Development of the Micro-magnetic Sensors Using Magneto-resistance Effect

WANG Guoan

Nagoya University

2011

Development of the Micro-magnetic Sensors Using Magneto-resistance Effect

(磁気抵抗効果を利用したマイクロ磁気センサーに関する研究)

A Dissertation

By

WANG Guoan

Submitted to Department of Quantum Engineering,
Graduate School of Engineering,
In partial fulfillment of the requirements for the degree of

Doctor of Engineering

NAGOYA UNIVERSITY

2011

Table of contents

Chapter 1 Introduction 1

1.1 Magnetic Field Sensors 1

1.1.1 Hall-effect Sensor 2

1.1.2 Fluxgate Sensor 3

1.1.3 Magneto-impedance Sensor 5

1.1.4 SQUID Sensor 6

1.1.5 Magneto-resistive Sensor 8

1.2 Magneto-resistive Effect 10

1.2.1 Anisotropic Magneto-resistive Effect 10

1.2.2 Giant Magneto-resistance Effect 11

1.2.3 Tunnel Magneto-resistance Effect 12

1.3 Spin-valve GMR 13

1.4 Magnetic Tunnel Junctions 14

1.5 Magnetic Anisotropy 16

1.5.1 Magneto-crystalline Anisotropy 16

1.5.2 Shape Anisotropy 17

1.5.3 Induced Anisotropy in Permalloy and CoFeB thin films 18

1.6 Magnetic Domains 18

1.6.1 Domain Wall Dynamics 19

1.7 Applications of Magnetic Sensors 22

1.7.1 Hard Disk Drive Read Heads 22

1.7.2 Biological Detection 24

1.7.3 Vehicle Detection 25

1.7.4 Eddy-current Testing 27

1.7.5 Rotary and Angle Sensing 28

1.8 Objectives of This Research 30

References 32

Chapter 2 Preparation and Analytical Tools 35

2.1 Preparation of the Sample 35

2.2 Preparation of Lithographic Photomasks 38

2.2.1 Electron Beam Lithography 38

2.2.2 Electron Beam Resists 41

2.2.3 Developing and Wet Etching 42

2.3 Micro-fabrication 45

2.3.1 Photolithography Techniques 45

2.3.2 Procedure of Photolithography 46

2.3.3 Ar^+ ion Etching 49

2.4 Analytical Tools 51

2.4.1 Alternating Gradient-field Magnetometer 51

2.4.2 Magneto-optical Kerr Effect Microscope 52

2.4.3 Transmission Electron Microscope 54

2.4.4 Magneto-resistance Measurement 55

References 57

Chapter 3 Domain Wall Displacing Type Field Sensor 58

3.1 Principle of Domain Wall Displacing Method 58

3.2 Fabrication of the DWD Type GMR Sensor 62

3.3 Electrical Circuits for DWD Type GMR Sensor 64

3.4 Properties of the GMR Sensor Device 66

3.5 Domain Structure and Wall Coercivity 68

3.6 Detection of Oscillatory Domain-wall Displacement 69

3.7 Field Detection by Oscillatory Domain-wall Displacement 72

3.8 Field Detection by Magnetization Rotation 76

3.9 Investigation of Shape and Materials for Free Layer 78

3.9.1 Domain Structure in Ferromagnetic Thin Films 78
3.9.2 Magnetic Property of Ferromagnetic Thin Films................................ 80
3.9.3 Dependence of the Minor Loop on GMR element width 81
3.9.4 Influence of Free-layer material on Sensor Output.............................. 84
3.10 Fabrication of DWD type TMR Sensor 88
3.11 Electrical Circuits for DWD Type TMR Sensor... 92
3.12 Field Detection Using DWD type TMR sensor... 94
3.13 Conclusions 101
References.. 103
Chapter 4 Magnetization Modulation Type Field Sensor.. 104
4.1 Principle of Magnetization Modulation Method...................................... 104
4.2 Sensor Device.. 106
4.3 Experimental configuration 108
4.4 Experimental Results and Discussion 111
4.5 Conclusions..116
Chapter 5 General Conclusions...117

Acknowledgements
List of Achievements

Chapter 1

Introduction

1.1 Magnetic Field Sensors

The magnetic sensors are solid state devices that convert magnetic or magnetically encoded information into electrical signals for processing by electronic circuits. Recently, the magnetic field sensors are used in many different types of application such as hard disk read heads [1-3], linear / rotary position sensing [4, 5], bio-magnetic sensing [6-8], etc. due to their non-contact wear free operation, robust design and immune to vibration, dust and water. With the development of information technology, there has always been a growing demand for more sensitive and lower power consumption magnetic field sensors.

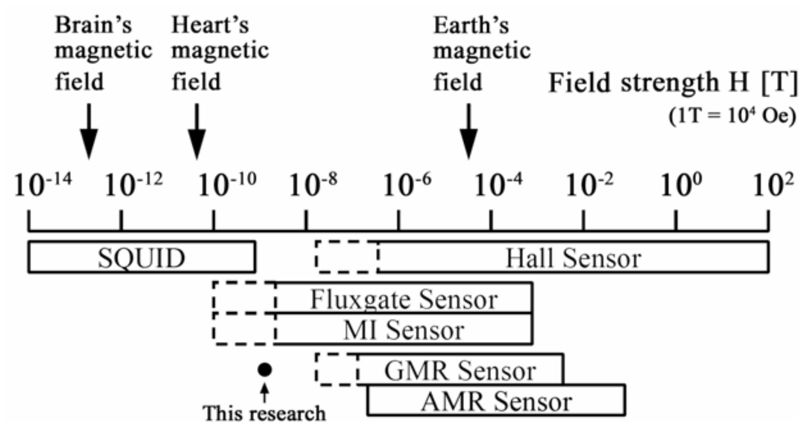

Fig. 1.1. Comparison of magnetic field sensors [9].

Some common magnetic sensors are listed in Fig. 1.1, which compares approximate sensitivity ranges. In Fig. 1.1, the arrows are used to indicate the field strength of the

Earth’s field, Heart's field and the field produced by human brain. Because of the large magnitude of the Earth’s field, sensors must either have a large dynamic range or use a coil to decrease the field at the position of the sensor.

1.1.1 Hall-effect Sensor

The Hall effect is one of the best known and earliest exploited for the solid-state sensor, which is discovered by Hall in 1879 with the basic physical principle underlying the Hall effect being Lorentz force [10]. The effect has been used in solid-state physics as a powerful tool in studying carrier transport phenomena. The development of semiconductor technology made possible the sensor applications of the Hall effect. In 1948, Pearson proposed a germanium Hall device as a magnetic sensor [11], and a few years after the discovery of high-mobility compound semiconductors, Hall sensors became commercially available. Hall effect sensors are devices which convert an external magnetic field to an electric voltage.

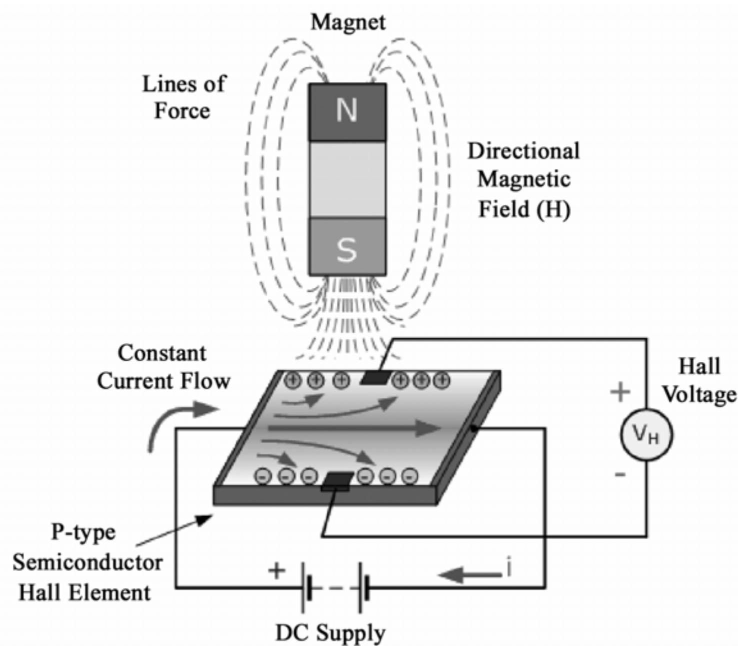

Fig. 1.2. Schematic of Hall effect magnetic field sensor [12].

Hall effect sensors consist basically of a thin piece of rectangular p-type semiconductor material such as gallium arsenide (GaAs), indium antimonide (InSb) or indium arsenide (InAs) passing a continuous current through itself, as shown in Fig. 1.2. When the device is placed within a magnetic field, the magnetic flux lines exert a force on charge carriers in the semiconductor material which deflects the charge carriers, electrons and holes, to either side of the semiconductor slab. This movement of charge carriers is a result of the Lorentz force they experience passing through the semiconductor material. As these electrons and holes move side wards, a potential difference is produced between the two sides of the semiconductor material. Then the movement of electrons through the semiconductor material is affected by the presence of an external magnetic field which is at right angles to it and this effect is greater in a flat rectangular shaped material.

1.1.2 Fluxgate Sensor

Fluxgate magnetic sensors are widely applied since it appeared in early 1930s. They are vector devices which are used to measure the components of magnetic fluxes density vector at one certain point, and they detect DC or low-frequency AC magnetic fields up to 10 Oe [13]. The theory exploited is based on the saturation of ferromagnetic materials [14]. They have the resolution of 10^{-6} - 10^{-4} Oe [15], even down to 10^{-7} Oe (10 pT), and the absolute precision of 10^{-5} Oe to 10^{-3} Oe [16].

Figure 1.3 shows the schematic of a single axis fluxgate magnetic sensor. The sensor consists of a ring core made of highly magnetically permeable alloy. Two coils are wound around these cores: the drive coil and the sense coil. Some sensors will also have a third feedback coil, if the sensor is to operate in a closed loop mode. Typically, there is

one ring core to measure the field in each of the 3 axes. An AC current pulse is injected into the drive coil to drive the material around its B-H loop and deeply saturating the core in alternate directions. The sense coil placed around the sensor picking up an induced voltage caused by changing flux within the coil as a result of an external field. This induced voltage appears as a signal at twice the drive frequency, which due to the nonlinearity of the *B-H* loops.

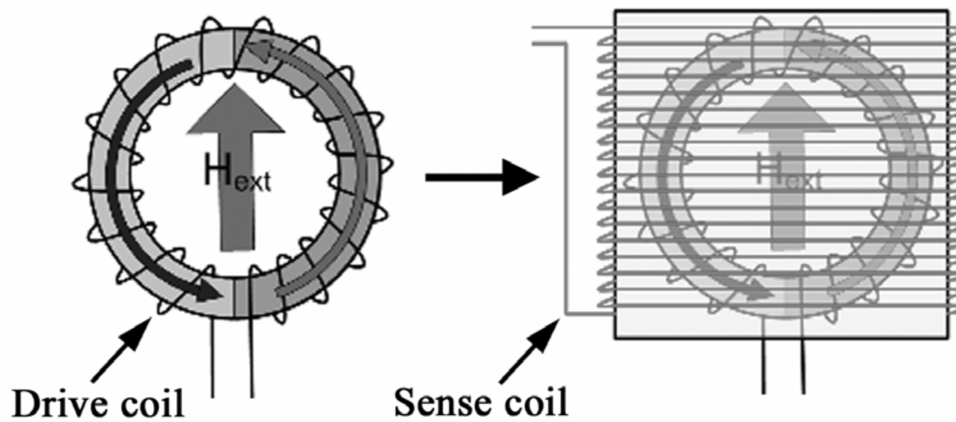

Fig. 1.3. Schematic of a single axis fluxgate magnetometer sensor.

The drive frequency (*f*) is typically tens of kHz and thus the induced frequency (2*f*) will be twice that. Sense and detection electrical circuits are required to extract magnitude and phase of the very small field proportional signal, to determine the field magnitude and direction. Signal amplification may be achieved either by use of an amplifier, tuning the sense coil as it is more sensitive at 2*f* or a combination of both. Fluxgate sensors will undergo a careful calibration usually in a low field or magnetic coil facility so that the sensors transfer function is accurately known.

1.1.3 Magneto-impedance Sensor

The giant magneto-impedance (GMI) effect was first observed in Co-based amorphous wires by Mohri et al. in 1992 [17]. It has since attracted significant interest due to its potential applications in highly sensitive magnetic field sensors. The GMI effect consists of a large variation of the impedance of a metallic magnetic conductor when a DC magnetic field is applied. Its origin is related to the classical electromagnetic skin effect. When a high frequency current flows along the conductor, typically elongated, it will concentrate into a small thickness from the surface. This penetration depth, according to the classical theory, is inversely proportional to the conductivity and to the permeability of the sample as well as to the frequency of the AC current. Consequently, large conductivity and permeability values lead to a reduced skin depth, penetration depth. The skin effect has been conventionally studied in metallic conductors with high electrical conductivity, and noble metals like Cu, Au or Ag exhibit noticeable skin effect [18]. The magnetic permeability of magnetic materials can be modified by the action of a DC magnetic field, which may change the penetration depth of the skin effect, and consequently, the impedance of these materials depends on the applied DC field.

Figure 1.4 (a) shows the schematic of MI sensor, an AC current is transmitted through the amorphous magnetic wire and the impedance of the wire is determined by measuring the output voltage of the pick-up coil. The output voltage changes with the DC magnetic field applied along the length direction of the amorphous wire. Figure 1.4 (b) shows the MI sensor element developed by Aichi Steel Corp. Company. The element consists of an amorphous wire (10 μm in diameter) and a micro pick-up coil.

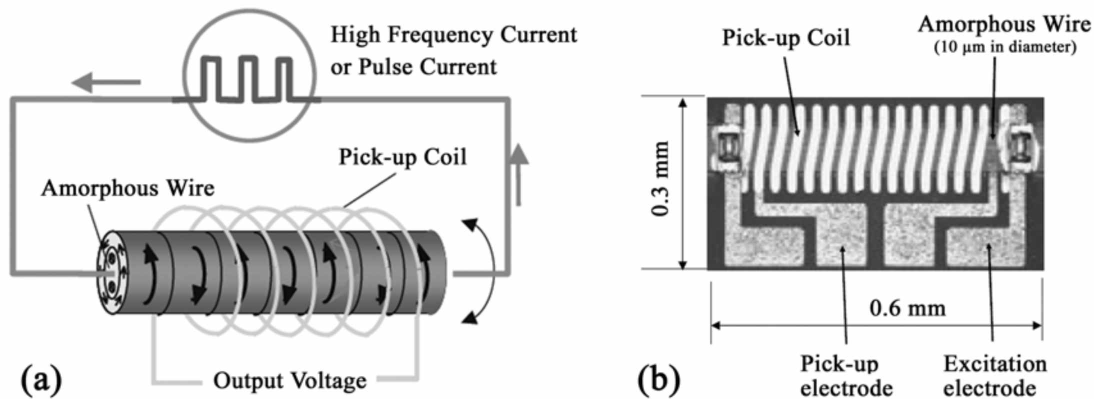

Fig. 1.4 (a) Schematic of magneto-impedance (MI) sensor, and (b) MI sensor element developed by Aichi Steel Corp. Company.

1.1.4 SQUID Sensor

The superconducting quantum interference device (SQUID) is the most sensitive instruments for measuring a magnetic field at low frequencies (< 1 Hz) [19, 20]. It is based on the remarkable interactions of electric currents and magnetic fields observed when certain materials are cooled below a superconducting transition temperature. At this temperature, the materials become superconductors and they lose all resistance to the flow of electricity. SQUIDs require cooling to liquid helium temperature (4 kelvin) at present. It can detect fields from several femtotesla up to 9 tesla, a range of more than 15 orders of magnitude. This is essential in medical applications since the neuromagnetic field of the human brain is only a few tenths of a femtotesla; Earth's magnetic field, by way of comparison, is ~30 mT, or 0.3 Oe.

A SQUID is simply a ring of superconducting material (see Fig. 1.5). The superconducting ring in a SQUID is typically a toroid (a few millimeters in diameter) made of a metal such as lead or niobium. While it is possible for a loop of superconducting material to have magnetic flux through the loop, the amount of flux will

keep constant. Any attempt to introduce more flux through the loop (running a current through the inductor) will create a current in the loop to cancel the introduction of flux. This changes the voltage across the SQUID.

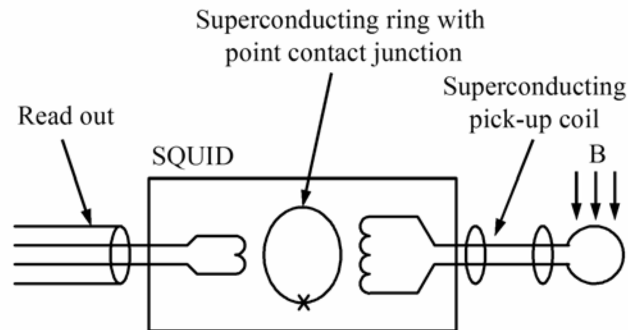

Fig. 1.5. Simple schematic of SQUID.

If a line of magnetic flux becomes threaded through the superconducting ring, a current is induced in the ring; in the absence of any further disturbances the current would continue flowing forever. The magnitude of the induced current is an exquisitely sensitive indicator of the flux density. It turns out that the flux through the ring is quantized [21, 22] and that the flux can only take on values that are integer multiples of a basic flux quanta. The sensitivity of SQUID is improved by coupling the ring to a larger superconducting loop or coil (without a weak link), which effectively serves as a magnetic “antenna” or DC search coil, gathering flux over an area of several square centimeters. Using superconducting properties, one can form a DC transformer between the sense loop and the SQUID readout. The SQUID ring essentially serves as a very precise ammeter for measuring the current in the pickup coil. Thus, the device has three superconducting components: the SQUID ring itself, the radio-frequency coil, and the large antenna loop. All three must be cooled to a superconducting state.

1.1.5 Magneto-resistive Sensor

The magneto-resistive sensor is based on the magneto-resistive (MR) effect [23], a change in resistance caused by an external magnetic field. Materials such as Permalloy (an alloy of nickel and iron) magnetizes along a direction parallel to the easy axis under zero external magnetic field. If an external field is applied perpendicular to the easy axis, the direction of magnetization will rotate toward the direction of the external field. The angle of magnetization depends on the amplitude of the external magnetic field. The resistance of the Permalloy element decreases as the direction of magnetization rotates away from the direction in which the current flows because the conduction electrons flowing in the direction of magnetization have a greater tendency to be scattered. The resistance changes roughly as the square of the cosine of the angle when the direction of magnetization is rotated from the direction of the current flow [24]. This effect is called anisotropic magneto-resistance effect.

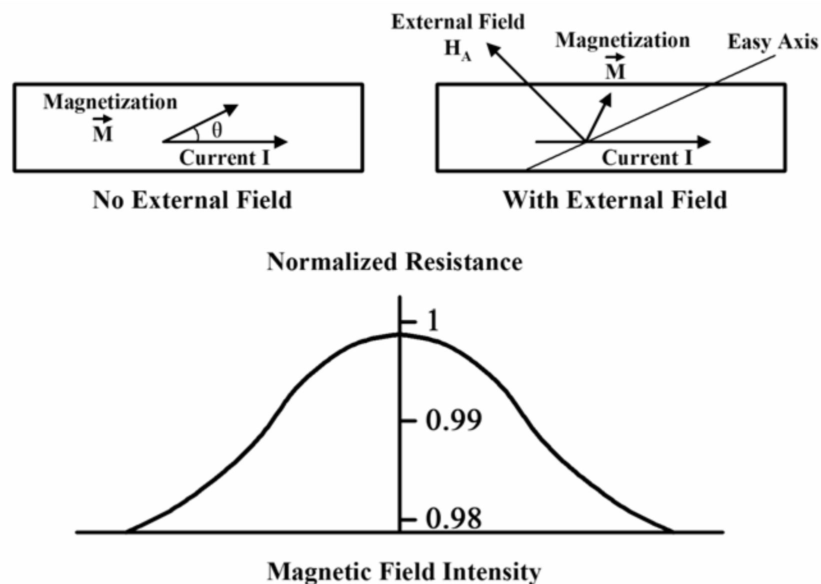

Fig. 1.6. Anisotropic magneto-resistive effect in a thin current strip.

Figure 1.6 illustrates the anisotropic magneto-resistive effect. Resistance of a ferromagnetic thin film varies with the direction of magnetization of the film. The resistance is highest when the magnetization is parallel to the current and lowest when it is perpendicular to the current. The magnetization rotates its direction depending on an applied external field, but it generally does not end up pointing in the same direction as the field because its direction is determined by several competing factors. One is induced magnetic anisotropy, where the easy axis is determined by the magnetic field applied during deposition of the film. Another is the shape anisotropy of the film, which in the case of a long, thin film, keeps the magnetization in the plane of the film and tends to make it point along the length direction of the film.

Permalloy is the most common material for magneto-resistive sensors because it has a relatively high magneto-resistive coefficient and because its characteristics are compatible with the fabrication techniques employed to make silicon integrated circuits such as a small coefficient of magneto-striction. The magneto-resistive sensors have a sensitivity range of 10^{-2} Oe to 50 Oe with open-loop readout electronics. With open-loop readout electronics, these sensors have an extremely wide dynamic range from DC to nearly 1 GHz. These sensors are small, low power consumption, and can be operated at wide temperature range.

1.2 Magneto-resistive Effect

The magneto-resistive (MR) effect is the change of the resistivity of a material due to a magnetic field; it has been discovered by Thomson in 1856 [23], which was later called ordinary magneto-resistance (OMR) effect. The improvement of the technology of thin ferromagnetic films (with a thickness of 10-50 nm) and the utilization of the anisotropic magneto-resistive (AMR) effect [25] led to an increasing technical interest in this effect. More recent researchers discovered materials showing giant magneto-resistance (GMR) effect [26] and tunnel magneto-resistance (TMR) effect [27], which are based on the weak coupling between separate thin ferromagnetic layers.

1.2.1 Anisotropic Magneto-resistive Effect

The anisotropic magneto-resistive (AMR) effect is the property of a material in which the electrical resistance depends on the angle between the direction of electric current and magnetization as briefly described in 1.1.5. The effect is attributed to a probability of s-d scattering of conduction electrons flowing along the direction of local spins. To compensate for the non-linear characteristics and inability to detect the polarity of a magnetic field, a somewhat more complex structure is used for sensors. It consists of stripes of aluminum or gold placed on a thin film of permalloy inclined at an angle of 45°. This structure forces the current not to flow along the easy axes of thin film, but at an angle of 45°. The dependence of resistance now has a permanent offset which is linear around the null point. The AMR effect is used in a wide array of sensors for measurement of Earth's magnetic field (electronic compass), for electric current measuring (by measuring the magnetic field created around the conductor), for traffic detection and for linear position and angle sensing.

1.2.2 Giant Magneto-resistance Effect

Giant magneto-resistance (GMR) is a quantum mechanical magneto-resistance effect as well as the AMR, but is observed in thin film structures composed of alternating ferromagnetic and nonmagnetic layers. The 2007 Nobel Prize in physics was awarded to Albert Fert and Peter Grunberg for the discovery of the GMR.

The effect is observed as a significant change in the electrical resistance depending on whether the magnetizations of adjacent ferromagnetic layers are in a parallel or an antiparallel alignment. The overall resistance is relatively low for parallel alignment and relatively high for antiparallel alignment. There are four types of GMR: multilayer GMR, spin valve GMR and granular GMR. In the multilayer GMR, two or more ferromagnetic layers are separated by a very thin (about 1 nm) non-ferromagnetic spacer (e.g. Fe/Cr/Fe). In spin valve GMR two ferromagnetic layers are separated by a thin non-ferromagnetic spacer (e.g. Cu). If the switching fields of the two ferromagnetic electrodes are different, it is possible to switch them independently. Therefore, parallel and anti-parallel alignment can be achieved, and normally the resistance is again higher in the anti-parallel case. For such purpose, one of the ferromagnetic layers is exchange coupled to the antiferromagnetic layer, which shifts the switching field due to the exchange bias effect. The antiferromagnetic (AF) coupling was first observed by Grünberg for Fe/Cr multilayers in 1986 [28]. Shortly afterwards, Parkin discovered that the coupling oscillates between the ferromagnetic and the antiferromagnetic configuration as a function of spacer thickness [29]. The granular GMR is an effect that occurs in solid precipitates of a magnetic material in a non-magnetic matrix. Granular GMR has been observed in matrices of copper containing cobalt granules. The reason for this is that copper and cobalt are immiscible, and so it is possible to create the solid precipitate by

rapidly cooling a molten mixture of copper and cobalt. Granule sizes vary depending on the cooling rate and amount of subsequent annealing.

1.2.3 Tunnel Magneto-resistance Effect

The tunnel magneto-resistance (TMR) effect is a magneto-resistive effect that occurs in magnetic tunnel junctions (MTJs), which consists of two ferromagnets separated by a thin insulator. If the insulating layer is thin enough (typically 1~3 nanometers), electrons can tunnel from one ferromagnet into the other.

The basic principle of the TMR is spin-dependent tunneling, which is ascribed to the spin-dependent density of states at the Fermi level E_F of ferromagnets, assuming that tunneling current is dependent on the density of states of the two electrodes and spin is conserved in tunneling. According to the models of Julliere [27] and Maekawa et al. [30], the tunneling magneto-resistance ratio *TMR* or $\Delta R/R$ is given by

$$\Delta R/R = (R_{AP} - R_P)/R_P = 2P_1P_2/(1-P_2) \qquad (1.1)$$

where R_{AP} and R_P are resistance of antiparallel and parallel ferromagnetic spin configurations, and $P_i(i=1,2) = [D_{i\uparrow}(E_F) - D_{i\downarrow}(E_F)]/[D_{i\uparrow}(E_F) + D_{i\downarrow}(E_F)]$ is the spin polarization of the FM electrodes. Large TMR ratio is essential for industrial application to increase the signal to noise ratio (SNR) and output voltage. Since Julliere's model is based on some ideal assumptions, the TMR value calculated by this model is usually the upper limit for the measured value. The TMR is highly dependent on temperature and applied bias voltage. The TMR generally decrease monotonically with increasing the applied bias voltage up to ~ 1V. Increase of the temperature generally diminishes the TMR, most likely due to the reduction of the magnetic moment at the electrode interfaces.

1.3 Spin-valve GMR

The spin-valve GMR structure consists of four layers: a “free” ferromagnetic layer, a spacing layer, a “pinned” ferromagnetic layer, and an antiferromagetic layer, as shown in Fig. 1.7. The antiferomagnetic layer on top “pins” the ferromagnetic layer underneath it, while the “free” ferromagnetic layer can be rotated by applying a magnetic field. Material such as MnPt, IrMn, PtMn, etc. are the commonly used as the antiferromagnetic materials. The unidirectional coupling between the antiferromagnet and ferromagnet was first observed in 1956 [31].

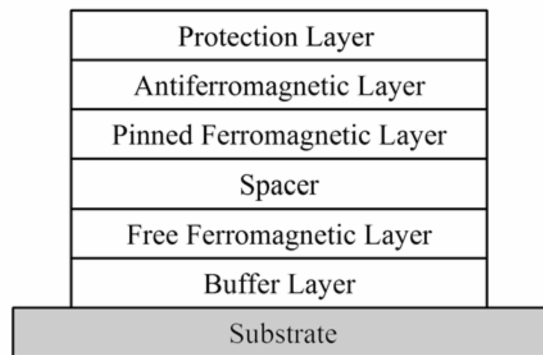

Fig. 1.7. Basic structure of a spin valve. The antiferromagnetic layer pins the adjacent ferromagnetic layer. The free ferromagnetic layer is able to rotate along an applied magnetic field.

The giant magnetoresistance is basically due to spin-dependent scattering of the conduction electrons at the ferromagnetic layers, which was first observed in 1956 [31]. For free layer with its magnetization direction parallel to the pin layer (as shown in Fig. 1.8 (a)), the conduction path with the electron spins parallel to the magnetization directions experiences low scattering, while the electrons of the other path are constantly scattered with a large probability, thus leading to a low electrical resistance. In the case of

antiparallel orientation of the magnetizations of adjacent ferromagnetic layers (as shown in Fig. 1.8 (b)), both conduction paths encounter high and low scattering probabilities, thus leading to a relatively high total resistance.

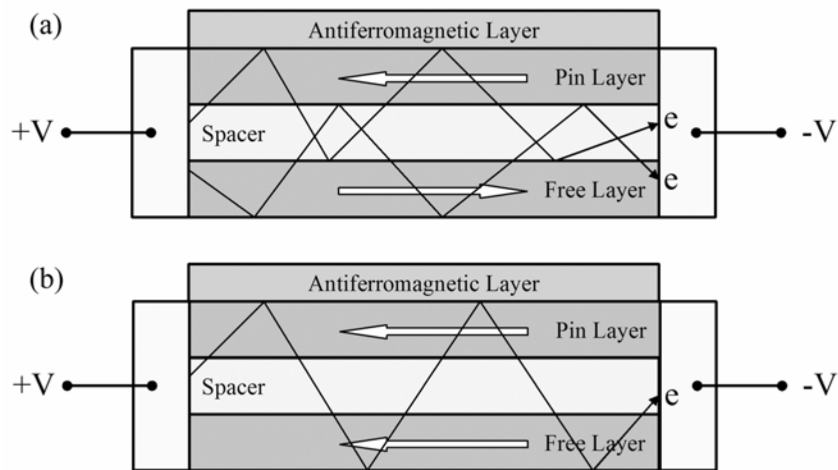

Fig. 1.8. Schematic of electron transport in a layered magnetic structure.

1.4 Magnetic Tunnel Junctions

The tunnel magneto-resistance (TMR) effect in ferromagnetic tunnel junctions consisting of ferromagnetic-insulator-ferromagnetic (FM-I-FM) structure was observed in 1975 [27]. The direction of the two magnetizations of the ferromagnetic films can be switched individually by an external magnetic field. If the magnetizations are in a parallel orientation it is more likely that electrons will tunnel through the insulating film than if they are in the oppositional (anti-parallel) orientation, as shown in Fig. 1.9. Consequently, such a junction can be switched between two states of electrical resistance, one with low and one with very high resistance.

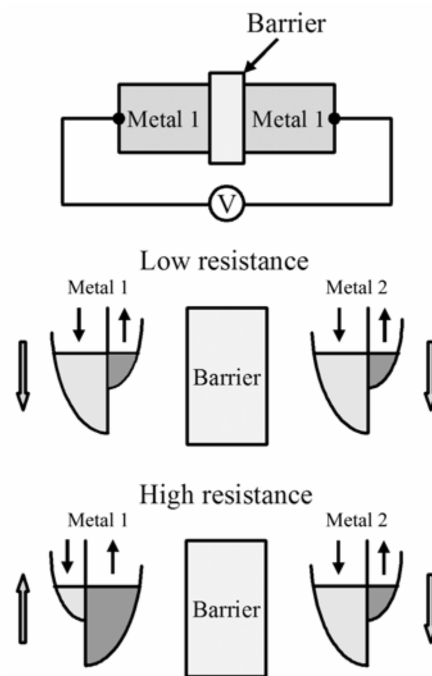

Fig. 1.9. A schematic model for spin dependent tunneling.

In MTJs, the conduction occurs by tunneling of electrons across the barrier. The insulating barrier must be very thin (1~3 nm thick) and is usually Al_2O_3 or MgO. The junctions can be shorted either in fabrication or by accidentally applying a large voltage across the junction that forms a pinhole or metallic bridge. The tunneling barrier (including its interfaces) is the most critical part in MTJs. For a proper operation of the tunnel junction, the following issues must be taken care of: the barrier must be homogeneous and without pinholes or impurities, which will cause large parasitic, unpolarized currents parallel to the polarized tunnel current and will decrease the TMR ratio. The film surfaces must be very smooth to minimize coupling between the layers [32]. Some roughness of the barrier interface can cause a magnetic coupling between the two ferromagnetic layers, which may result in the situation that the layers do not switch independently and an antiparallel state cannot be achieved anymore.

MTJ devices have higher resistance and magneto-resistance value than GMR. Because of the higher resistance, MTJ has lower power consumption than GMR. However, MTJ devices often have an inherent noise that is much larger than the Johnson noise limit. Klaassen et al. [33] gave a general discussion of the noise in MTJ and pointed out that different noise mechanisms. Because of their high magneto-resistance, high resistance, and planer geometry, MTJs have potential for being used as low cost, energy efficient, high sensitivity magnetic sensors. A single axis MTJ has been used to construct a two-axis magnetometer [34]. MTJs are also the key element in nonvolatile magnetic random access memory (MRAM).

1.5 Magnetic Anisotropy

Magnetic anisotropy is the dependence of the internal energy of a system on the direction of the spontaneous magnetization. An energy term of this kind is called magnetic anisotropy energy. In general most kinds of magnetic anisotropy are related to the crystal symmetry of a material and this is known as magneto-crystalline anisotropy. Anisotropy can also be related to the shape of magnetic materials, which is known as shape anisotropy. Magnetic anisotropy strongly affects the shape of hysteresis loops and controls the coercivity and remanence.

1.5.1 Magneto-crystalline Anisotropy

Magneto-crystalline anisotropy is an intrinsic property of a ferromagnetic material, independent of grain size and shape. It arises mostly from spin-orbit coupling. As a result, certain crystallographic directions are preferred directions, or easy axes, for the magnetization. The magneto-crystalline anisotropy can be most easily seen by measuring

magnetization curves along different crystal directions, which is the energy necessary to deflect the magnetic moment in a single crystal from the easy to the hard direction.

In cubic crystals, like magnetites, the magneto-crystalline anisotropy energy is given by a series expansion in terms of the angles between the direction of magnetization and the cube axes. It is sufficient to represent the anisotropy energy in an arbitrary direction by just the first two terms in the series expansion. These two terms, each has an empirical constant associated with them, are called the first and second order anisotropy constants, or K_1 and K_2, respectively.

1.5.2 Shape Anisotropy

The anisotropy is due to the shape of magnetic materials. A magnetized ferromagnetic film will produce magnetic charges or poles at the surface. This surface charge distribution is another source of a magnetic field, called the demagnetizing field. It is called the demagnetizing field because it acts in opposition to the magnetization that produces it. The shape anisotropy energy for a thin layer contains an angular dependent term. For thin films, the demagnetizing field will force the magnetization into the plane of the film. In a thin film considered as a magnetic continuum the dipolar anisotropy energy per unit volume is given by [35]

$$E = \frac{1}{2}\mu_0 M_s^2 \cos^2\theta \qquad (1.2)$$

where M_s is the saturation magnetization, assumed to be uniform throughout the layer. The magnetization subtends an angle (θ) to the plane normal. The dipolar anisotropy energy is thus minimized for an angle of 90° ie moments lying in the plane of the layer.

1.5.3 Induced Anisotropy in Permalloy and CoFeB thin films

Uniaxial anisotropy of soft magnetic film is required to ensure output signal stability and linearity in MR sensors. Many research groups have used permalloy ($Fe_{20}Ni_{80}$ alloy) thin film as a magnetic free layer in GMR and TMR spin-valve because it is easy to get soft magnetic property by a simple process [36-38]. Magnetic anisotropy can be induced in soft magnetic thin films by applying a magnetic field during preparation [39], and also by using post-deposition heat treatments. The origin of this anisotropy is the pare-ordering of atoms in the alloy film, which is called as induced anisotropy. Permalloy shows very low magneto-striction and low crystalline magnetic anisotropy; therefore it could be possible to realize high permeability. Uniaxial anisotropy H_k can also be induced in soft amorphous CoFeB thin films by applying a DC field during the sputtering process.

1.6 Magnetic Domains

A magnetic domain is a region within a magnetic material which has a uniform magnetization [40]. The individual magnetic moments of the atoms are aligned with one another and they point in the same direction. When heated above a temperature called the Curie temperature, a piece of ferromagnetic material undergoes a phase transition, and the uniform magnetization within a domain spontaneously disappears: each atom has its own direction of magnetic moment, independent from its neighboring atoms. Magnetic domain structure is responsible for the magnetic behavior of ferromagnetic materials like iron, nickel, cobalt and their alloys, ferrites etc. The regions separating magnetic domains are called domain walls, where the magnetization rotates coherently from the direction in one domain to that in the next domain.

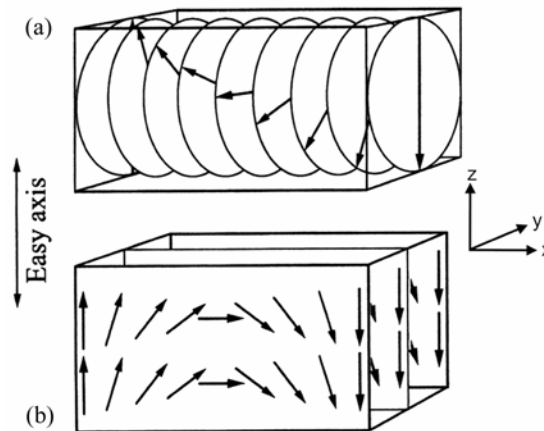

Fig. 1.10. Rotation of the magnetization vector in the (a) Bloch wall and in the (b) Neel wall [41].

There are two main types of spin structures inside the domain walls, Bloch and Néel types. Besides many other kinds of domain walls exist. One of them is called the cross-tie wall, which is an intermediate state between Bloch and Néel walls, and it is composed of a mixture of Bloch and Néel walls [42, 43]. In Fig. 1.10, the spin structures of Bloch and Néel walls are shown. The Bloch wall is usually preferable in bulk materials. Spins rotate in the plane parallel to the wall plane. The wall width of a 180° Bloch wall is most commonly defined by $\pi\sqrt{A/K}$, where A and K are the exchange constant and anisotropy energy, respectively [42]. Then the Néel wall becomes more favorable when the film thickness becomes smaller than the wall width. In a Néel wall, spins rotate in the film plane (Fig. 1.10 (b)). The Néel wall profile is well explained in [42, 44].

1.6.1 Domain Wall Dynamics

The dynamic behavior of magnetization is described by the Landau-Lifshitz-Gilbert equation [45, 46]:

$$\dot{M} = \frac{\gamma}{\mu_0} T + \frac{\alpha}{M}[M \times \dot{M}] \tag{1.3}$$

where γ = -1.8 × 10^7 $Oe^{-1}s^{-1}$ is the gyromagnetic ratio, α is the phenomenological damping constant, and T is the torque acting on the magnetization. The Gilbert equation summarizes the standard model for the evolution of the magnetization in rigid ferromagnetic bodies. When a domain wall is driven by a magnetic field, the position of the domain wall is generally governed by the following equation

$$m\frac{d^2 s}{dt^2} + \beta\frac{ds}{dt} + as = 2M_s H \tag{1.4}$$

where m is the mass of the domain wall, β is the frictional factor of the wall, and the term as express the restoring force. M_s and H are magnetization and applied field, respectively. If it is assumed the constant wall motion and negligible restoring force, the velocity of the wall is simplified as

$$v = \frac{ds}{dt} = \frac{2M_s H}{\beta} \tag{1.5}$$

The β is related to the energy dissipation of the magnetization, i.e., the second term of the LLG equation (1.4), and expressed as

$$\beta = \frac{2M_s \alpha}{\gamma \Delta} \tag{1.6}$$

where Δ is the domain wall width. In the Walker model, the wall velocity (1.6) becomes the maximum at the Walker field $H_{Walker} = 2\pi\alpha M_s$ [47], and the maximum wall velocity v_{max} is given by

$$v_{max} = 2\pi M_s \gamma \Delta \tag{1.7}$$

The velocity only increases with the driving field up to the critical Walker field [48]. Beyond the critical field no steady state is possible and the average velocity decreases with increasing the applied field.

Similar considerations also apply to the oscillatory domain wall motion regime, which corresponds to the case of negligibly small wall velocity under almost zero applied field. In such a case, the equation of the wall motion is approximated as

$$m\frac{d^2 s}{dt^2} = -as \tag{1.8}$$

The effective mass of the domain wall *m* was discussed by Döring, and is connected with the change in wall energy at small velocities. Following Döring, the mass is defined as

$$m = \frac{1}{2\pi\gamma^2\Delta} \tag{1.9}$$

The restoring force under the small applied field is related to the initial suceptivility χ_a, and when the external field is applied parallel to the easy axis of the uniaxial anisotropy, *a* is expressed as

$$a = \frac{4M_s^2}{\chi_a}S \tag{1.10}$$

where *S* is the domain wall area in unit volume. Thus the oscillation frequency of the domain wall is written as

$$\omega \approx \frac{5}{\sqrt{\chi_a}}\sqrt{S\delta}\gamma M_s \tag{1.11}$$

This expression means the oscillation frequency is limited by the total volume of the domains. If we assume the stripe domains with the width of 100 µm and the wall width of 10 nm, the $\sqrt{S\Delta}$ will become 10^{-2}, and thus the maximum frequency of the wall oscillation will be 1/100 of the resonance frequency of the magnetization expected from LLG equation.

1.7 Applications of Magnetic Sensors

Magnetic sensors have been used in analyzing and controlling thousands of functions for many decades. Computers have nearly unlimited memory through the use of magnetic sensors in hard disk drives (HDDs) and tape drives. Airplanes fly with higher safety standards because of the utilization of high reliability non-contact switches with magnetic sensors. Automobiles use magnetic sensors to navigate or determine position in several places such as the engine crank shaft and wheel braking. Factories promoted its productivity because of the stability and low cost of magnetic sensors [50–53].

1.7.1 Hard Disk Drive Read Heads

New GMR read heads for hard disk drive (HDD) have been developed by IBM and other companies. In the read heads, the spin valve material is etched into a narrow stripe, and the magnetization of the pin layer is oriented across the stripe [54]. Figure 1.11 shows the schematic of magnetic recording. It uses a GMR head for reading, and uses an inductive coil for writing.

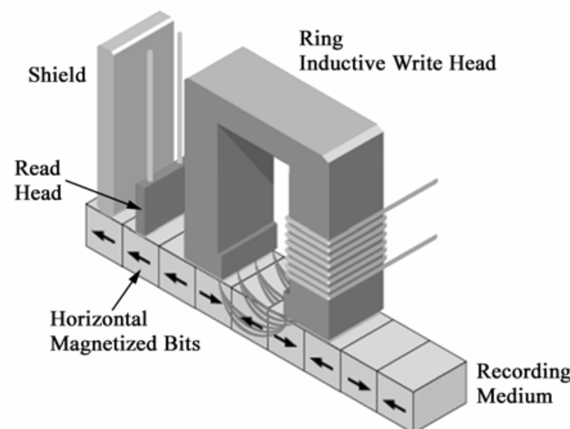

Fig. 1.11. Schematic of magnetic recording process.

Because of the higher sensitivity, GMR heads are superior to the conventional MR heads. The older MR heads typically exhibit a resistance change of about 2% when passing from one magnetic polarity to another, for GMR heads the MR change is about 5% to 8%. This means GMR heads can detect much weaker and smaller signals, which greatly increased the areal density. They are also much less subject to noise and interference because of their increased sensitivity, and they can be made smaller and lighter than the conventional MR heads. GMR heads are also typically fitted with "shields" that prevent them from being affected by stray magnetic fields, i.e., anything but the bit directly below the head.

With the increase of industry demands for higher density, the size of the read head becomes smaller and smaller, and demagnetizing effects in very narrow horizontal sensor stripes will become a major challenge. For example, in the center of a permalloy stripe (100 Å thick, 0.25 μm wide), the self demagnetizing field is about 200 Oe. At the edges of the stripe, the demagnetizing effects tend to “pin” the magnetization along the edge, thus magnetization near the edges of the stripe is very insensitive to magnetic fields. The magneto-static coupling of magnetization near the edge also reduces the sensitivity of GMR heads. These demagnetizing effects limit the sensitivity to the fields produced by the recording media, and become more difficult to implement as sizes keep shrinking [55]. One way to reduce the demagnetizing effects in the horizontal stripe is to make the magnetic films (and the nonmagnetic interlayer) thinner while retaining high GMR. This will increase the resistance of GMR and improve SNR. Another way is to reduce the magnetization of the ferromagnetic layers. This raises fundamental issues about the relationship between magnetization and GMR. Because the magnetic field produced by the recording media decreases very rapidly with vertical distance from the media surface,

it is important that the spin valve be sensitive to fields very near the outside surface of the head. The rapid decrease is due to the nature of the field from the media, and the magnetic shields. Shielding materials are thick and have high permeability, thus creating a low reluctance path to shunt off the signal flux.

1.7.2 Biological Detection

Selective and quantitative detection of all kinds of bio-molecules plays an important role in the biosciences. Recently, the idea of integrating all these common laboratory tasks into a single easy-to-use portable device has received growing attention both by researchers and biotechnology companies [56-58]. The fast development of devices based on GMR and TMR makes the magnetic biosensors become possible. Due to their direct electronic translation and their small and scalable size, which is also compatible with standard Complementary Metal-Oxide Semiconductor (CMOS) processing, MR devices experienced a great boost within the last decade. Compared to the established fluorescent detection method, magnetic biosensors have many advantages, including low molecular detection limits, flexibility and the direct availability of an electronic signal suitable for automated analysis.

The bio-molecule to be detected (target or analyte) is magnetically labeled (immobilized on a magnetic label) and passed over an array of specifically patterned complementary or non-complementary (probe) molecules, which are immobilized over on-chip magnetic field sensors. The magnetic sensors detect the presence of the magnetic labels via a change in sensor resistance at a fixed sense current. The unbound target bio-molecules are then washed away and residual sensor signals are obtained at sensor sites, where complementary magnetically labeled target and surface-bound probe

molecules have successfully interacted. As shown in Fig. 1.12, the interaction of a magnetic label, functionalized with bio-molecule A, with a magneto-resistive sensor-bound bio-molecule B. The magnetic fringe field resulting from the magnetic moment of the label within an on-chip applied magnetic field changes the resistance of the sensor, resulting in a voltage signal at a sensing current. If this signal remains after the appropriate washing of the sensor surface, this indicates the detection of molecular recognition between bio-molecules A and B [59].

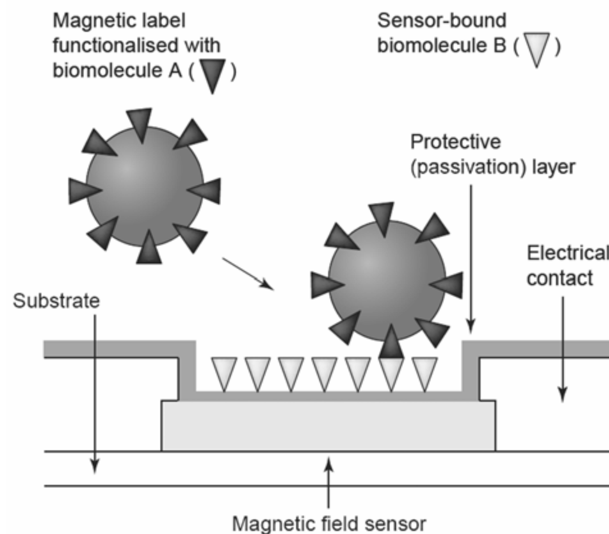

Fig. 1.12. Simplified cross-sectional scheme for magnetically labeled biomolecule detection in biosensor [59].

1.7.3 Vehicle Detection

The earth's field provides a uniform magnetic field over a wide area about several kilometers. A car will create a local disturbance in this field. The disturbance can be modeled as a composite of many dipole magnets. These dipoles have north-south orientations that cause distortions in the earth's magnetic field. Magnetic sensors can detect the change in the earth's field due to the vehicle disturbance.

There are several forms of applications for vehicle detection [60]. Depending on vehicle's ferrous content, the sensing distance from the vehicle can extend up to 15 meters away. This is useful in parking garages to give drivers the information that where the most available spaces to park. Another use is to detect the moving direction of the vehicle, which will be useful for safety reasons such as activating warning lights when traffic through tunnels, and operating crossing gates when train approaching. The axis along the moving direction can be used to determine the direction of the vehicle (see Fig. 1.13). When there is no car present, the sensor output is only the background earth's magnetic field as its initial value. When the car approaches, the earth's magnetic field lines of flux will be drawn toward the car. If the car is traveling left to right, and the sensing axis of the magnetic sensor points to the right, the sensor will initially detect a decreasing field since more flux lines bend toward the oncoming car. The first magnetic deviation from the sensor's initial value will swing in the negative direction.

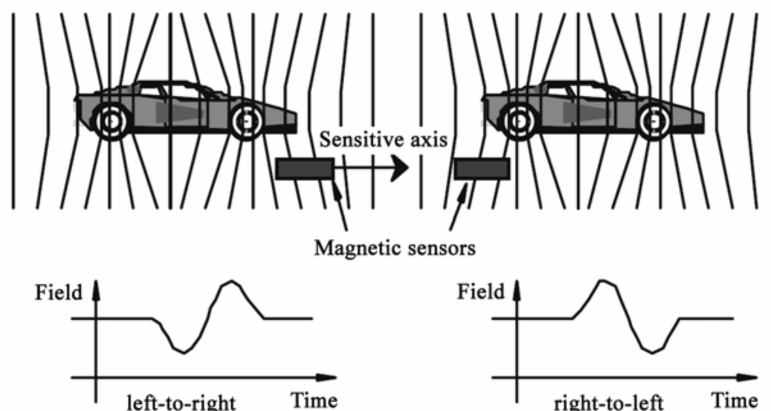

Fig. 1.13. Direction sensing for vehicles driving over magnetic sensor [60].

When the car is directly inline with the sensor, the sensor output curve returns to the initial value. The flux lines will bend toward the car in the positive sensor axis when the

car leaves to the right. This will cause the sensor output to increase above the initial value. When the car is out of sensing range, the sensor output will again return to the initial value. The left-hand curve in Fig. 1.13 shows the sensor response to a vehicle moving left-to-right. When the car is traveling in the opposite direction, the flux lines are attracted toward the car, i.e., in the positive sensor direction, causing an initial increase in the sensor output. The right-hand curve in Fig. 1.13 shows the sensor response to a vehicle moving right-to-left.

1.7.4 Eddy-current Testing

Eddy-current testing (ECT) is commonly used for detecting defects such as fatigue cracks, inclusions, voids, etc., in conductive materials to evaluate the expected life of mechanical components. Eddy currents are induced in a specimen by applying an alternating magnetic field. A cylindrical coil can be used to produce an excitation magnetic field which induces circular currents constrained to a region near to the surface of the specimen under test. In the presence of defects, which act as a high resistance barrier, the eddy-current flow is perturbed. As a result of this defect, a "leakage" magnetic field is produced. Such field perturbations are usually detected as an impedance change in the exciting coil [61]. To enhance the sensitivity and spatial resolution of the measurement, more advanced techniques based on the separation with the excitation and detection elements have been developed. Inductive sensors of reduced dimensions [62, 63] have been proposed for detection. Among these sensors, the MR sensors offer a good tradeoff in terms of performance versus cost.

Currently, inductive probes based on small pickup coils are used for surface crack detection with high resolution. However the reduction of the coil diameter leads to the

decrease in sensitivity of these probes. This is because the induced voltage depends proportionally to the magnetic flux intercepted by the pickup coil, which in turn is proportional to its cross-sectional area [64]. To solve this problem, a GMR-based probe (as shown in Fig. 1.14) has been developed for detecting small surface-breaking cracks with high accuracy [65]. The GMR-based eddy-current probe consists of a relatively large cylindrical coil with the GMR sensor located on the coil axis. The GMR sensor consists of four thin-film resistors in a Wheatstone bridge configuration with two of them being magnetically shielded and acting as dummy resistors. The sensing axis of the GMR probe is coplanar with the surface of the specimen. The excitation field on the coil axis, being perpendicular to the sensing axis of the GMR films, has no effect on the sensor. In a defect-free specimen, because of the circular symmetry of the induced eddy currents, these will produce no effect on the sensor output. In the presence of a defect, output signal from the sensor is produced by the perturbation of the eddy-current flow path.

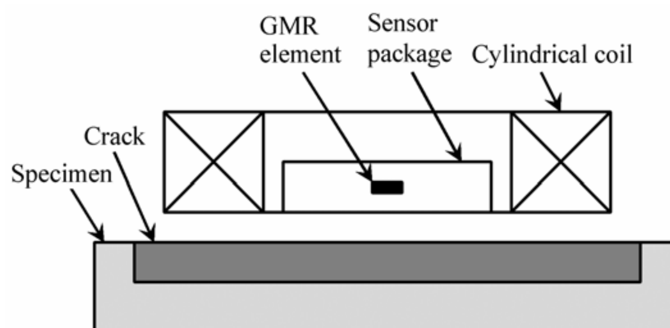

Fig. 1.14. Schematic diagram of the GMR-based probe.

1.7.5 Rotary and Angle Sensing

Magnetic rotary and angle sensors are fundamental devices in many mechanical and electronic systems. For compact equipment, small and low-cost sensors capable of high

resolution detection are required. The GMR sensors are very suitable for analog angle sensing because of their intrinsic angle dependence. Since the angle dependence of the GMR effect has a period of 360° it is possible to cover the full revolution of 360° with two GMR sensors that are mutually rotated over 90°. Such a contactless angle sensor can be used in automotive applications to sense the rotation-speed, which is used in the anti-lock braking systems (ABS). The principle is illustrated in Fig. 1.15. The sensor is positioned between a (soft) magnetic gear wheel and a permanent magnet (as shown in Fig. 1.15 (a)), with its sensitivity direction in the tangential direction. If a tooth of the wheel is exactly opposite the sensor (as shown in Fig. 1.15 (b)), the field lines from the magnet cross the sensor perpendicularly (in which direction it is not sensitive) and the sensor gives null output. If a tooth is approaching from above, as shown in Fig. 1.15 (c), the field lines are deviated upwards, resulting in a component along the sensitive direction of the sensor. Analogously, for a tooth below the sensor the output signal is negative. In this way a rotating wheel gives an output signal of positive and negative pulses approximating a sinusoidal signal. The number of peaks per time interval is a measure for the rotation speed.

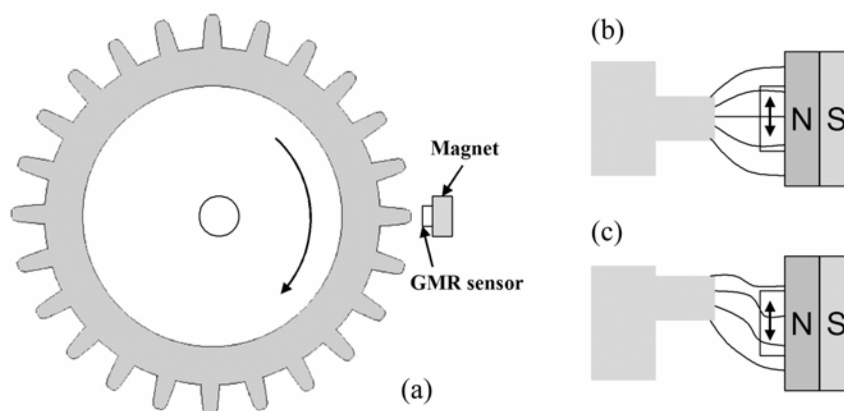

Fig. 1.15. Schematic view of rotary sensing.

1.8 Objectives of This Research

The tunnel magneto-resistive (TMR) and giant magneto-resistive (GMR) magnetic field sensors have been widely used in many applications such as hard disk read heads, linear/rotary position sensing, and bio-magnetic sensing. Compared to various other field sensors, the TMR and GMR sensors have high-frequency response (over 1 MHz) and can be easily integrated onto one chip. However, typical TMR and GMR sensors show lower field resolution compared to fluxgate and magneto-impedance sensors. For most of the conventional TMR and GMR field sensors with spin-valve structure, the free-layer magnetization of the sensor device is saturated by a bias field produced with a pair of thin-film magnets, and the external field perpendicular to the bias field is detected (see Fig. 1.16). In this case, the magneto-resistance (MR) change of the sensor is caused by the magnetization rotation of the free layer.

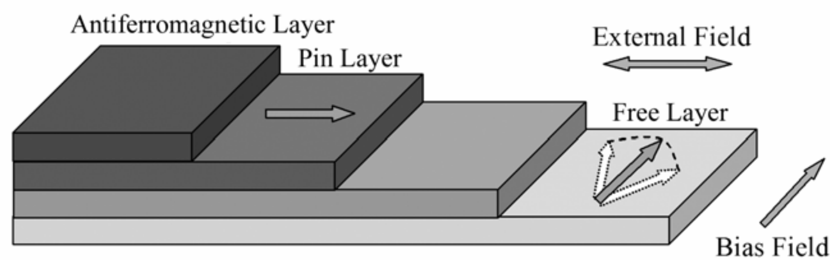

Fig. 1.16. Schematic diagram of the conventional spin-valve field sensor, the free-layer magnetization is saturated perpendicular to the pinned direction by a bias field and rotated by the applied external field.

In this thesis, we propose a new method utilizing the oscillatory domain wall displacement in the ferromagnetic free layer to detect the external field. Since the domain wall displacement is more sensitive to the external field than the magnetization rotation, higher sensitivity compared to the conventional field sensors is expected. However, in

order to utilize the displacement of domain wall to detect the external field, we have to face two problems: 1) the wall coercivity in the ferromagnetic materials, 2) the discontinuous domain-wall motion known as Barkhausen effect. To avoid the influence of these two factors, an AC field was applied to stimulate the oscillatory domain wall motion in the ferromagnetic free layer and the external field was detected by measuring the shifting of the oscillatory domain wall. The oscillatory domain wall displacement reduces the influence of wall coercivity and Barkhausen effect, and enables the sensor to detect the magnetic field which is much smaller than the wall coercivity.

As many sensors, the domain wall displacing (DWD) type field sensor is also suffered from the DC drift of sensor output caused by the change of environmental temperature, and is only suitable for AC field detection. To solve this problem, we propose another type of field sensor which senses the external field by detecting the change of frequency component in the modulated sensor output. For this type of sensor, the direction of free-layer magnetization direction is modulated by an alternating field and the external field is detected by measuring the change of frequency component in the modulated signal using a lock-in amplifier. The modulation type sensor normally works in a closed-loop mode and the DC output of lock-in amplifier acts as a negative feedback in the system. Since the feedback current in the system is independent of the resistance and MR ratio of the sensor, this method significantly reduces the drift caused by the thermal fluctuation. Thus the modulation type sensor can be used for high precision DC field detection without the additional temperature compensation.

References

[1] R. Rottmayer and J. G. Zhu, IEEE Trans. Magn. 31, 2597 (1995).

[2] T. Miyazaki and N. Tezuka, J. Magn. Magn. Mater. 139, L231 (1995).

[3] S. N. Mao, Y. H. Chen, F. Liu, X. F. Chen, B. Xu, P. L. Lu, M. Patwari, H. W. Xi, C. Chang, B. Miller, D. Menard, B. Pant, J. Loven, K. Duxstad, S. P. Li, Z. Y. Zhang, A. Johnston, R. Lamberton, M. Gubbins, T. McLaughlin, J. Gadbois, J. R. Ding, B. Cross, S. Xue, and P. Ryan, IEEE Trans. Magn. 42, 97 (2006).

[4] H. A. M. Van den Berg , W. Clemens, G. Gieres, G. Rupp, M. Vieth, J. Wecker, and S. Zoll, J. Magn. Magn. Mater. 165, 524 (1997).

[5] K. M. H. Lenssen, D.J. Adelerhof, H.J. Gassen, A.E.T. Kuiper, G.H.J. Somers, and J.B.A.D. van Zon, Sens. Actuators A 85, 1 (2000).

[6] H. A. Ferreira, D. L. Graham, P. P. Freitas, and J. M. S. Cabral, J. Appl. Phys. 93, 7281 (2003).

[7] G. Li, V. Joshi, R. L. White, S. X. Wang, J. T. Kemp, C. Webb, R. W. Davis, and S. Sun, J. Appl. Phys. 93, 7557 (2003).

[8] S. C. Mukhopadhyay, K. Chomsuwan, C. P. Gooneratne and S. Yamada, IEEE Sens. J. 7, 401 (2007).

[9] H. Wakiwaka, Transactions of the Institute of Electrical Engineers of Japan A 126, 265 (2006).

[10] E . H. Hall, Am. J. Math., 2, 287 (1879).

[11] G. L. Pearson, Rev. Sci. Instrum., 19, 263 (1948).

[12] http://www.electronics-tutorials.ws/electromagnetism/hall-effect.html.

[13] P. Ripka, Sens. Actuators A 106, 8, (2003).

[14] F. Primdahl, J. Phys. E: Sci. Instrum. 12, 241 (1979).

[15] P. Ripka, S. Kawahio, S. O. Choi, A. Tipek and M. Ishida, Sens. Actuators A 91, 65 (2001).

[16] P. Ripka, JMMM 215216, 735 (2000).

[17] K. Mohri, T. Kohhzawa, K. Kawashima, H. Yoshida and L.V. Panina, IEEE Trans. Magn. 28, 3150 (1992).

[18] M. Knobel, M. Vazquez and L. Kraus, Handbook of magnetic materiasl 15, 497 (2003).

[19] V. Pizzella, S. D. Penna, C. D. Gratta and G. L. Romani, Supercond. Sci. Technol. 14, R79 (2001).

[20] R. Cantor, Supercond. Cryoelectron. 13, 16 (2001).

[21] B. S. Deaver and W. M. Fairbank, Phys. Rev. Lett. 7, 43 (1961).

[22] R. Doll and M. Nabauer, Phys Rev. Lett. 7, 51 (1961).

[23] W. Thomson, Proc. R. Soc. London A 8, 546 (1857).

[24] E. L. James, Proc. IEEE 78, 6 (1990).
[25] I. Genish, Y. Kats, and L. Klein, J. Appl. Phys. 95, 6681 (2004).
[26] M. N. Baibich, J. M. Broto, A. Fert, F. Nguyen Van Dau and F. Petroff, Phys. Rev. Lett. 61, 2472 (1988).
[27] M. Julliere, Phys. Lett. 54A, 225 (1975).
[28] P. Grünberg, R. Schreiber, Y. Pang, M. B. Brodsky and H. Sowers, Phys. Rev. Lett. 57, 2442 (1986).
[29] S. S. P. Parkin, N. More and K. P. Roche, Phys. Rev. Lett. 64, 2304 (1990).
[30] S. Maekawa and U. Gafvert, IEEE Trans. Mag. 18, 707 (1982).
[31] W. H. Meiklejohn and C. P. Bean, Phys. Rev. 102, 1413 (1956).
[32] J. L. Leal and M. H. Kryder, IEEE Trans. Magn. 32, 4642 (1996).
[33] K. B. Klaassen, J. C. L. v. Peppen, and X. Xing, J. Appl. Phys. 93, 8573 (2003).
[34] J. B. Kammerer, L. Hebrard, M. Hehn, F. Braun, P. Alnot and A. Schuhl, IEEE Sens. J. 4, 313 (2004).
[35] M. T. Johnson, P. J. H. Bloemen, F. J. A. den Broeder and J. J. de Vries, Rep. Prog. Phys. 59, 1409 (1996).
[36] A. S. Kao and P. Kasiraj, IEEE Trans. Magn. 27, 4452 (1991).
[37] H. Funaki, S. Okanoto, O. Kitakami and Y. Shimada, Jpn. J. Appl. Phys. 33, L1304 (1994).
[38] M. Kitada, K. Yamamoto, J. Magn. Magn. Mater. 147, 213 (1995).
[39] A. Miktus, J. Wenda, K. Kulakowski, J. Magn. Magn. Mater. 160, 341 (1996).
[40] B. D. Cullity and C. D. Graham, Introduction to Magnetic Materials, 2nd edition. New York: Wiley-IEEE. 116 (2008).
[41] Magnetization reversal dynamics in magnetically coupled trilayer systems, Fukumoto Keiki, der Freien Universitat Berlin, Germany, Ph.D Dissertation, 2005.
[42] A. Hubert and R. Schafer, Magnetic Domains (Springer, Berlin, 1998).
[43] T. Trunk, M. Redjdal, A. Kakay, M. F. Ruane and F. B. Humphrey, J. Appl. Phys. 89, 7606 (2001).
[44] A. Holz and A. Hubert, Z. angew. Phys. 26, 145 (1969).
[45] L. Landau and E. Lifshitz, Phys. Z. SU 8, 153 (1935).
[46] T. L. Gilbert and J. M. Kelly, Proc. Conf. Magnetism and Magnetic Materials, A.I.E.E., New York 1955 (p. 253).
[47] L.R. Walker, unpublished. Reported in J. F. Dillon Jr., Domains and Domain Walls, in Magnetism, Eds. G. R. Rado and H. Suhl, Academic Press, New York (1963).
[48] Schryer, N. L., and Walker, L. R., J. Appl. Phys. 45 (12), 5406-21 (1974).
[49] N. L. Schryer, L. R. Walker, J. Appl. Phys. 45, 5406 (1974).
[50] J. E. Lenz, Proc. IEEE 78, 973 (1990).

[51] A. E. Mahdi, L. Panina, and D. Mapps, Sens. Actuators A 105, 271 (2003).

[52] J. M. Daughton, A. V. Pohm, R. T. Fayfield and C. H. Smith, J. Phys. D: Appl. Phys. 32, R169 (1999).

[53] J. Lenz and A. S. Edelstein, IEEE Sens. J. 6, 3 (2006).

[54] C. Tsang, R. Fontana, T. Lin, D. Heim, V. Speriosu, B. Gurney and M. Williams, IEEE Trans. Magn. 30, 3801 (1994).

[55] J.M. Daughton, J. Magn. Magn. Mater. 192, 334 (1999).

[56] L.J. Kricka, Clin. Chim. Acta 307, 219 (2001).

[57] D. Figeys and D. Pinto, Anal. Chem. 72, 330A (2000).

[58] J. Wang, Nucleic Acids Res. 28, 3011 (2000).

[59] D. L. Graham, H. A. Ferreira and P. P. Freitas, Trends Biotechnol. 22, 9 (2004).

[60] M. J. Caruso and L. S. Withanawasam, Sensors Expo Proceedings 477 (1999).

[61] S. K. Burke, J. Non-Destruct. Eval. 7, 35 (1988).

[62] J. Pavo and K. Miya, IEEE Trans. Magn. 32, 1597 (1996).

[63] M. Uesaka, T. Nakanishi, K. Miya, H. Komatsu, K. Aoki, and K. Kasai, IEEE Trans. Magn. 31, 870 (1995).

[64] E. S. Boltz and T. C. Tiernan, Rev. Prog. Quant. Non-Destruct. Eval. 17, 1033 (1998).

[65] T. Dogaru and S. T. Smith, IEEE Trans. Magn. 37, 5 (2001).

Chapter 2

Preparation and Analytical Tools

The sensor devices are built from different stacks consisting of magnetic layers and nonmagnetic layers, the thickness of each layer is in the range of roughly 1-20 nm. The film stacks are deposited onto thermally oxidized silicon wafers in UHV chambers by RF magnetron sputtering. Subsequently, they are micro-fabricated into a number of separate sensor elements by photolithography and Ar^+ ion etching techniques. The resist patterns are transferred to the layer stacks either by deposition of additional films or by Ar^+ ion etching. After completion, individual sensor elements are measured by magneto-electronic transport measurements, and the magnetic property of the film stacks are characterized by alternating gradient field magnetometer (AGM). Following is a short description of the employed preparation and analytical tools.

2.1 Preparation of the Sample

The GMR and TMR thin-film stacks were deposited on 525-μm-thick thermally oxidized <100> silicon wafers with a 500-nm-thick SiO_2 layer. The deposition was carried out in magnetron sputtering systems. Argon gas of purity (99.9999%) was used as the sputtering gas and the working pressure was set to be constant of 0.4 Pa. Before inserting the Si substrates into the sputtering chamber, they were rinsed in an ultrasonic bath using isopropyl alcohol (IPA) for 5 minutes. Prior to the sputtering, the chamber

was evacuated to a low base pressure using a turbo molecular pump. The Ar^+ ion cleaning process cleaned the substrate on atomic level to smooth out any uneven surface irregularities and to knock out surface contaminations present on the substrate. Another advantage of the Ar^+ ion cleaning of the substrate is to enhance the adhesive force between sputtered atom and the substrate surface. Pre-sputtering was also performed for cleaning the target surface before the sputtering deposition.

Figure 2.1 shows the schematic diagram of the 8-source magnetron RF sputtering system used for the film deposition. The permanent magnets located behind the target can enhance the sputtering rate effectively. This system consists of a main chamber and a load-lock chamber, where a transfer arm is used to transfer the samples between these two chambers. The base pressures of the main chamber and the load-lock chamber are lower than 2.0×10^{-7} Pa and 1.0×10^{-5} Pa, respectively. The Al_2O_3 tunnel barriers for TMR films were formed by depositing a layer of metallic Al and oxidizing it using oxygen plasma produced on an Al_2O_3 target (4 Pa, 200 W, 80 Sec.). A 5-source sputtering system was used to deposit the metallic electrodes and the insulating layers during the sensor device fabrication. A so-called reverse-sputtering was performed before the deposition (2 Pa, 100 W, 60 Sec.) to clean the substrate surface. The background pressure of the 5-source sputtering chamber is lower than 2.0×10^{-5} Pa.

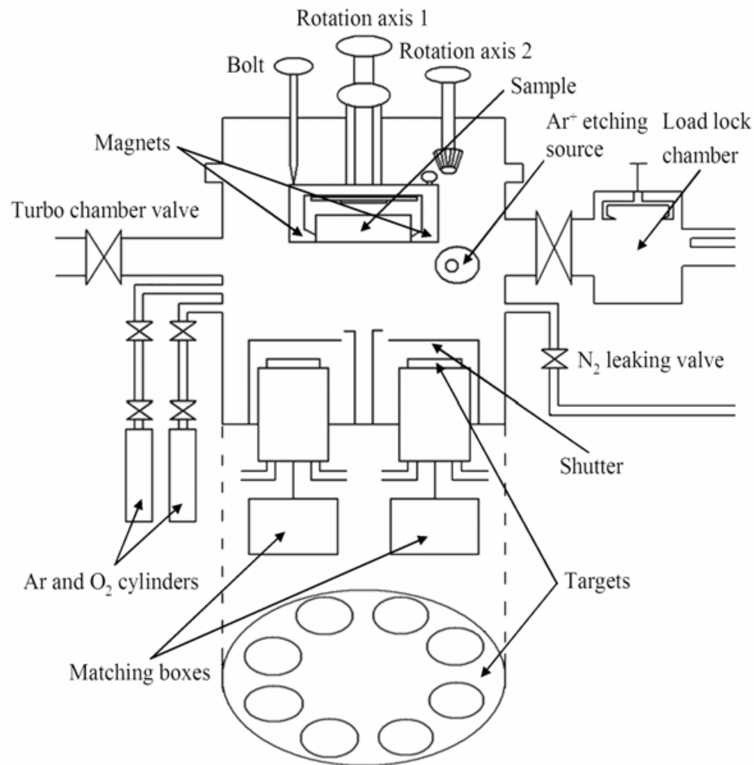

Fig. 2.1. Schematic diagram of the 8-source magnetron sputtering system.

The layer structure of the TMR and GMR multilayer films are illustrated in Fig. 2.2. The TMR and GMR stacks have a bottom pinned and a top pinned structure, respectively. The sputtering conditions for each layer are listed in Table 2.1 and Table 2.2.

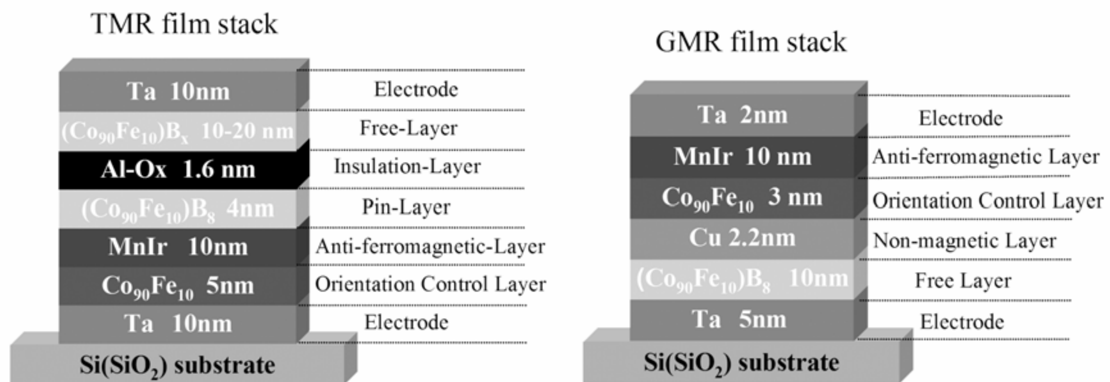

Fig. 2.2. Layer structure of the TMR and GMR multilayer films.

Table 2.1 Sputtering condition for 8-source sputtering system (2 inch targets).

Target	Power [W]	Sputtering rate [Å/sec]	Ar pressure [Pa]
Ta	80	0.36	0.4
CoFe	120	0.41	0.4
CoFeB	120	0.35	0.4
MnIr	90	0.76	0.4
Al	120	0.31	0.4
Cu	60	0.41	0.4

Table 2.2 Sputtering condition for 5-source sputtering system (3 inch targets).

Target	Power [W]	Sputtering rate [Å/sec]	Ar pressure [Pa]
Al	150	0.83	0.4
Pt	90	0.41	0.4
Al_2O_3	200	0.42	0.4

2.2 Preparation of Lithographic Photomasks

Lithographic photomasks are typically transparent covered with a pattern defined chrome metal film. In this research, 2-inch transparent SiO_2 wafers (0.5 mm thick) were used as the substrates, on which a metallic chrome film of 70 nm was deposited.

2.2.1 Electron Beam Lithography

The electron beam lithography (EBL) technique was used to expose the patterns on the photomasks. Compared to other lithographic methods, the EBL offers higher patterning resolution, as listed in Table 2.3 [1].

Table 2.3 Practical and ultimate resolution limits for lithographic methods.

Lithography Type	**Practical**	**Ultimate Limit**	**Lithography**
Ultraviolet Light	150 nm	50 nm	Ultraviolet
Extreme Ultraviolet	90 nm	30 nm	Extreme
Ion Beam	30-50 nm	10-20 nm	Ion Beam
X-Ray	70 nm	10 nm	X-Ray
Imprinting	20-40 nm	8-10 nm	Imprinting
Electron Beam	40-50nm	7-20 nm	Electron Beam

The EBL system is similar to a scanning electron microscope (SEM), where an electron beam is focused to a spot onto the substrate and scanned over the desired field of view. The major differences between an SEM and an EBL system is that in an SEM, the emphasis is on capturing signals emitted from the sample, due to the incident electron beam, for imaging and analysis, while an EBL system is focused on controllably applying the desired dose of electrons in a localized pattern on the substrate [2]. Therefore, the EBL system includes a highly accurate positional control stage using laser interferometry to measure the position of the stage and sample, a Faraday cup with a pA current detector, high speed blanking system for blocking the electron beam during the stage movement, sophisticated software and routines for automatically correcting for focus, stigmatism, and a computer interface to feed data from a CAD file into the instrument.

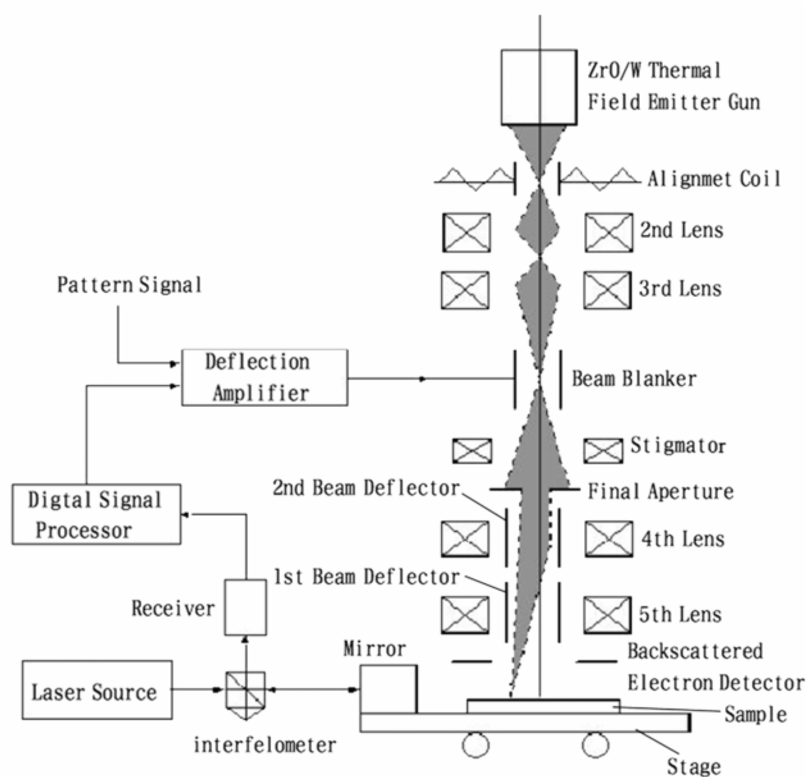

Fig. 2.3. Schematic diagram of the JEOL JBX-6000FS EBL system.

In this research, the JEOL JBX-6000FS EBL system was utilized. It consists of substrate holders with an interferometrically controlled X-Y stage, high quality vacuum units, a vibration isolated electron optical column, a wafer handling system that automatically feeds wafers to the system and unloads them after processing; and a computer system that controls the equipment. The system is illustrated in Fig. 2.3. The JBX-6000FS generates a high current density electron beam using a thermal field emission gun with a ZrO/W emitter. The system is capable of high-speed pattern exposure on high-resolution (low sensitivity) resists. The JBX-6000FS uses in-lens electrostatic deflector free from hysteresis, assuring high stability. It incorporates two different objective lenses for fine and ultra fine pattern exposures with a beam diameter range of 5 nm to 200 nm.

2.2.2 Electron Beam Resists

The resists used for microlithography must have a high resolution, high sensitivity, and good dry-etch resistance as basic properties. Usually, the e-beam resists are high molecular-weight polymers dissolved in a liquid solvent. The polymer changes its structure when exposed to radiation, including electron beam radiation. Electron beam resists can be either positive or negative [3].

For the positive resist, the exposed area is removed in the developing process, and for the negative resist, the exposed area is insoluble. In this work, both positive and negative resists were used. Polymethyl methacrylate (PMMA) [4] was one of the positive resists developed for EBL and remains the most commonly used resist that has a very high resolution. The major problems of the PMMA are the relatively poor sensitivity and poor dry etch resistance. Here, a non-chemically amplified positive resist ZEP520A (a copolymer of chloromethacrylate and methylstyrene) and a chemically amplified negative tone resist NEB22 were used as the EB resists.

A spin coater was used to deposit a smooth film of resist on the substrate. Before the resist coating, substrates are rinsed in an ultrasonic bath using acetone and IPA for 5 minutes, respectively. The resist material is dissolved into a suitable solvent and deposited onto a substrate rotating at an angular frequency of several hundred to several thousand revolutions per minute while the solvent evaporates. The centrifugal force throws the majority of solution off the substrate and spreads the remaining solution across the substrate, leading to a smooth film. After the resist coating, the film is baked to evaporate the solvent residues in the film using a hot plate or baking oven. The film is then ready for the e-beam exposure and subsequent development. The doses of exposing for ZEP520A and NEB22 are 120 $\mu C/cm^2$ and 40 $\mu C/cm^2$, respectively.

2.2.3 Developing and Wet Etching

The developing process was performed after the electron beam exposing. Table 2.4 lists the chemicals and developing processes for the ZEP520A positive resist and the NEB22 negative resist.

Table 2.4 Chemicals and developing processes for ZEP520A and NEB22.

EB Resist	Resist type	Chemicals and process
ZEP520A	Positive	1. Xylene 40 sec. 2. IPA 30 sec. 3. N_2 blowing.
NEB22	Negative	1. SOPD-R 50 sec. 2. Pure water rinse 90 sec. 3. Hot plate hard baking, 130 °C, 240 sec.

The regions of the underlying chrome film, which are no longer protected by the photoresist after development, were etched in an acid liquid (13.7 wt. % diammonium nitrate and 3.5 wt. % hydrogen peroxide, pure water balance). After the wet etching, it is necessary to strip the resist. The ZEP520A, positive resist, was dissolved by ZDMAC Remover, and the NEB22, negative resist, was removed using a mixed liquid (70 vol. % dimethyl sulfoxide and 30 vol. % aminoethanol). The striping process was carried out using an ultrasonic bath for 20 minutes at 60 °C. The optical microscope images of the photomasks are shown in Fig. 2.4 and Fig. 2.5, where the chrome on dark areas are etched. The fabricated photomasks are finally fixed on the 4 inch square glass plates using resin glue.

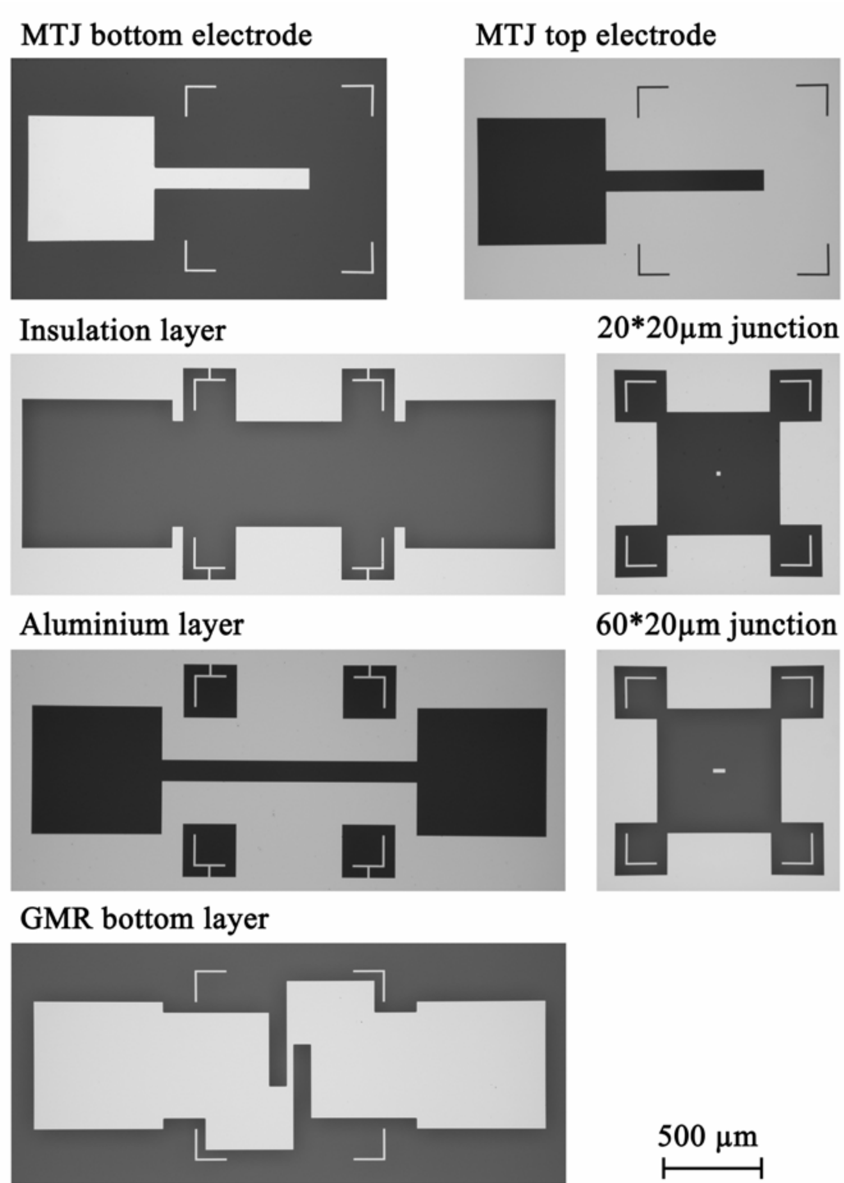

Fig. 2.4. Optical microscope images of the photomasks for TMR and GMR type sensor devices.

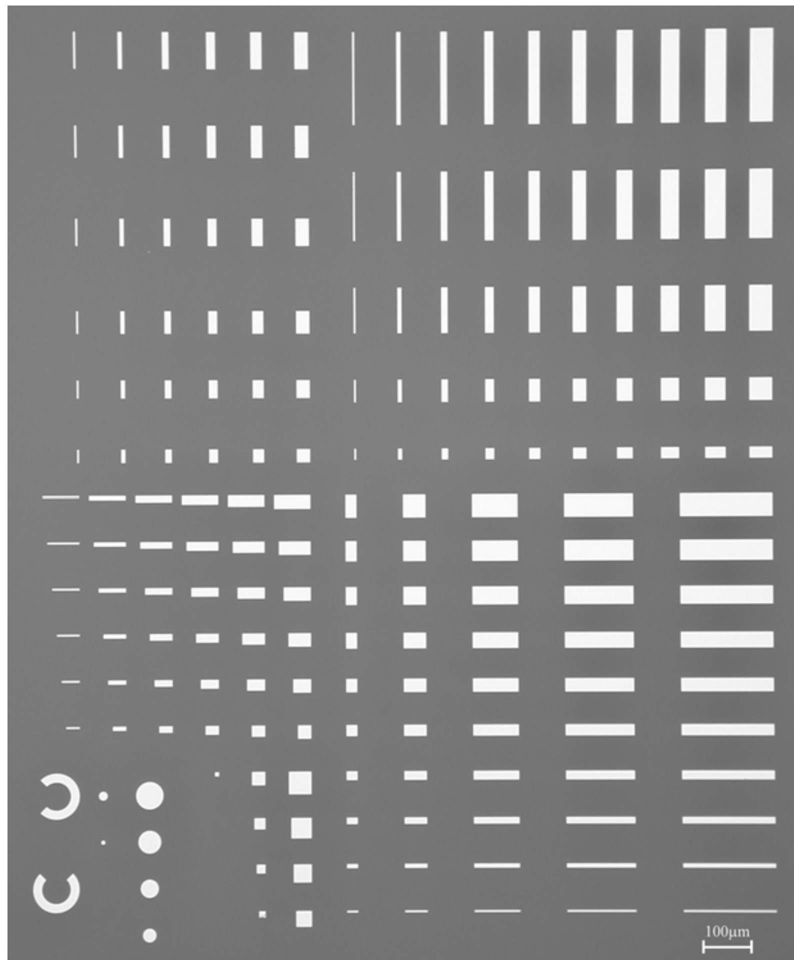

Fig. 2.5. Optical microscope images of the photomask prepared for the observation of domain wall structures in various patterns.

2.3 Micro-fabrication

The sensor devices were micro-fabricated by performing a serial of photolithography, Ar^+ ion etching and sputtering processes. Materials were deposited or etched from the exposed area to form the sensor structures.

2.3.1 Photolithography Techniques

Photolithography a technique used to transfer the patterns designed on the photomask onto a photosensitive resist that covers the sample. The resist patterns are transferred to the layer stacks either by deposition of additional materials followed by the lift-off of the resist (positive lithography) or by Ar^+ ion etching (negative lithography). Therefore, there are two alternative techniques that are generally used to obtain patterned samples: etching and lift-off techniques, as shown in Fig. 2.6.

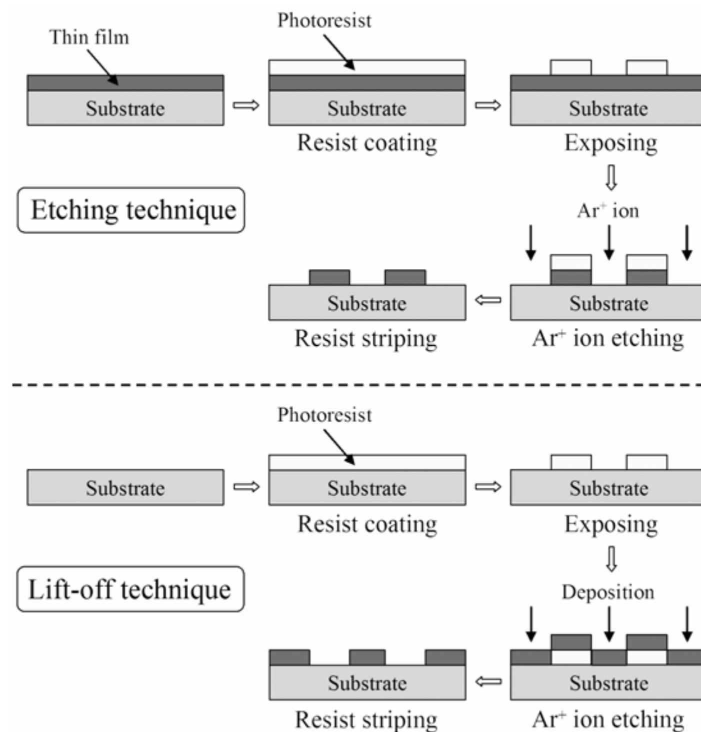

Fig. 2.6. Schematic diagram of etching and lift-off techniques.

For etching process, a photoresist is coated onto the film surface and the patterns of photomask are transferred on the photo-resist. Then, the entire sample surface is exposed to Ar^+ ions or etchant resulting in non-etched regions, which are covered with resist, and etched regions, which are not covered. After the etching process, the resist is dissolved by a solvent in an ultrasonic bath. In case of the lift-off technique, after the patterns of photomask are transferred on the resist, the thin film is deposited on the entire of the sample. Then, the deposited materials onto the resist are removed by a solvent in an ultrasonic bath, obtaining the patterned sample. For the fabrication of sensor devices, both etching and liftoff techniques were employed, while for the patterned single-layer film only the etching process was used.

2.3.2 Procedure of Photolithography

The photolithography process must be performed in a yellow light, since the photoresist is most sensitive to blue light. For this reason, it is necessary to use the yellow lights room when handling the photoresist or samples before they are developed and rinsed. Furthermore it is important that the sample is not exposed to dust. Since the normal laboratory is not a clean room, we carried out those process steps that are sensitive to particle contamination in a clean room. On top of the clean room, there are some Hepa (High Efficiency Particulate Air) filters, which will filter out most of the particles in the air. Inside the clean room, it is possible to create a class 1000 atmosphere (class 1000 means that there are less than 1000 particles of 0.5 μm per cubic feet). The photolithography process steps are listed as follows:

Step 1: Substrate cleaning and dehydration

Before resist coating, the Si substrates were rinsed in an ultrasonic bath using

isopropyl alcohol (IPA) for 5 minutes to remove the moisture and contaminants, both of which cause a multitude of resist processing problems. After that, the substrates were blown with dry N_2 to eliminate any moisture adsorbed by sample surfaces, since hydrated substrates result in adhesion failures.

Step 2: Resist coating

Resist coating is performed by spin-coating, which produces a uniform, adherent, and defect-free resist film of required thickness over the sample. Spin-coating consists of dispensing the resist solution over the sample surface and rapidly spinning the wafer until it becomes dry. Resist spinning thickness T depends on spin speed ω (rpm), solution concentration C (the polymer concentration in grams per 100 ml solution), and molecular weight (measured by intrinsic viscosity η). There is half- empirical formula to express their relationship [5]:

$$T = \frac{KC^{\beta}\eta^{\gamma}}{\omega^{\alpha}} \quad (2.1)$$

where, K is a calibration constant. Once the various exponential factors (α, β and γ) have been determined the equation can be used to predict the thickness of the film that can be spun for various molecular weights and solution concentrations of a given polymer and solvent system. Equation (2.2) was found to be true for positive S1813 resist which was used in this work [6].

$$T = K'\omega^{-0.5} \quad (2.2)$$

The units of T and ω are nm and krpm, respectively. The proportional constant K' in this work is around 3000 [nm/(krpm)$^{1/2}$].

Step 3: Soft baking

The coated photoresist was pre-baked at 110 ºC for 10 min in the convection oven to

drive away the solvent from the spun-on resist, which will improve the adhesion of the resist to the wafer, and anneal the shear stresses introduced during the spin-coating. Soft baking is a critical step in photolithography, and will affect the resist profile.

Step 4: Exposure

After the sample has been coated with photoresist and subjected to soft baking, S1813 resist on the sample was exposed to the mixed light of g-line (436 nm), h-line (405 nm) and i-line (365 nm) offered by high pressure Hg lamp using mask aligner (MIKASA M-10).

Step 5: Post exposure baking

The exposed resist was post-baked at 90 ºC for 20 min to reduce the standing waves in regular positive resist and to rearrange the overexposed and underexposed photoresist molecules, which smoothes the sidewall of patterns and improve resolution. Insufficient post-exposure baking will not completely eliminate the standing wave pattern, while over-baking will cause polymerization and affects the photoresist development.

Step 6: Development and striping

After the post exposure baking process, the sample was developed in SHIPLEY MF CD-26 DEVELOPER to remove the exposed regions. The sample was soaked for 15 sec and agitated softly for 45 sec in the developer, and followed by puddling in pure water for 1 minute. Regardless of development method, it should always be followed by thorough rinsing and drying to ensure that the development action will not continue after the developer has been removed from the sample surface. The unexposed area can be removed using the hot MICROPOSIT REMOVER 1165 liquid (60 °C) in an ultrasonic bath for 20 minutes.

2.3.3 Ar^+ ion Etching

In general, there are two classes of etching processes: wet etching where the material is dissolved when immersed in a chemical solution, and dry etching where the material is sputtered or dissolved using reactive ions or a vapor phase etchant. Ar^+ ion etching is a dry etching technique, which uses plasma generated to remove material only from the regions that are no longer protected by photoresist after development.

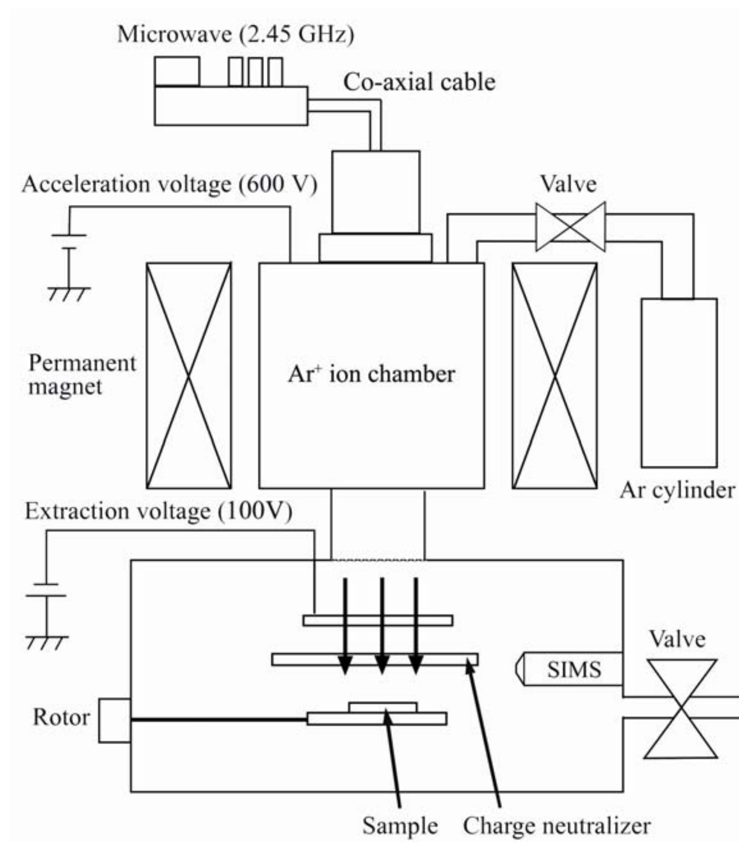

Fig. 2.7. Schematic diagram of ECR system.

In this research, an electron cyclotron resonance (ECR) physical etching system was used. Figure 2.7 shows the schematic diagram of ECR system. Microwaves (2.45 GHz) are injected through a co-axial cable into the plasma source and a resonant magnetic field

(about 875 G) is applied with a permanent magnet. The plasma source produces the ion/radical flux streams into the process vacuum chamber where the sample is located. Because of the low operating pressure for ECR plasmas (typically < 1 mTorr, about 0.1 mTorr in this work), the anisotropy of the etched features is greater than other ion etching techniques. In order to determine the etching depth, the secondary ion etched from the sample surface was detected with a quadrupole type secondary ion mass spectrometry (SIMS; EPD 400) technique [7], which is widely used in material science and surface science to analyze the composition of solid surfaces and thin films. The quadrupole SIMS separates the masses by resonant electric fields, which allow only the selected masses to pass through.

The sensor devices were micro-fabricated by performing a serial of sputtering, photolithography, Ar^+ ion etching and sputtering processes. Figure 2.8 shows the optical microscope images of the (a) GMR type sensor device and (b) TMR type sensor device.

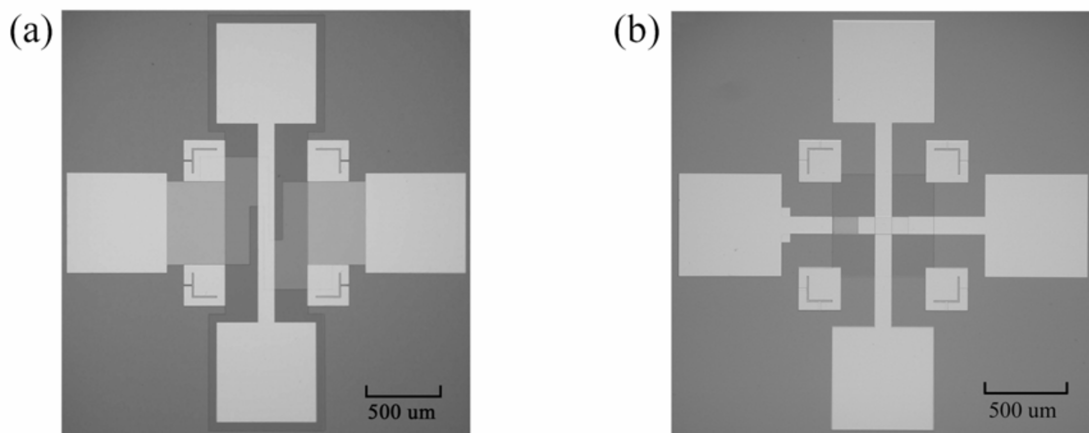

Fig. 2.8. Optical microscope images of the (a) GMR type sensor device and (b) TMR type sensor device.

2.4 Analytical Tools

2.4.1 Alternating Gradient-field Magnetometer

Alternating gradient-field magnetometer (AGM), which has a sensitivity exceeding (10^{-8} emu), was used to measure the magnetic moments of the magnetic thin films. The principle of the AGM is that the alternating field gradient exerts an alternating force on the sample, proportional to the magnitude of the field gradient and the magnetic moment of the sample. The acting force on the sample is measured by a piezoelectric element to determine the magnetic moment of the sample. The sample mounted on the tip of a cantilevered rod that incorporates a piezoelectric element is magnetized by a DC field and simultaneously subjected to a small alternating field gradient. The top end of the sample rod is attached to the piezoelectric element, as shown in Fig.2.9.

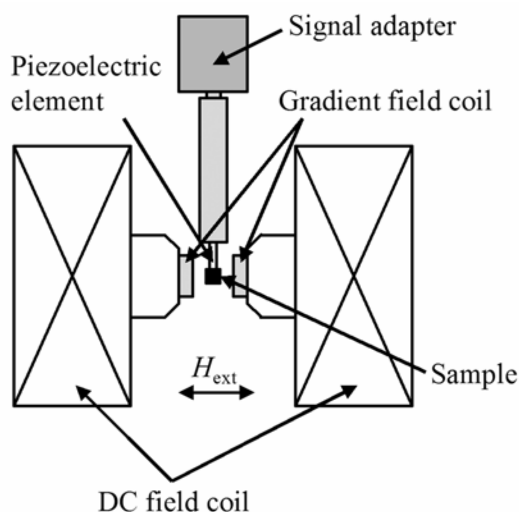

Fig. 2.9. Schematic diagram of alternating gradient-field magnetometer.

The force of the field gradient on the magnetized sample produces a bending moment on the piezoelectric element, which generates a voltage proportional to the force

on the sample. The output from the piezoelectric element is synchronously detected at the frequency of the gradient field. The amplitude of this voltage is proportional to the magnetic moment of the sample, which can be varied by changing the applied DC magnetic field $H_{ext.}$ To enhance the signal to noise ratio (SNR), the gradient field is tuned at the mechanical resonant frequency of the cantilever. The gradient field varies in orders smaller than the coercive fields of the investigated sample and is applied by the small coil placed in the greater field coils providing the magnetic bias field. The maximum field of the AGM used in this research is 22 kOe and the measurement frequency is from 100 Hz to 1000 Hz.

2.4.2 Magneto-optical Kerr Effect Microscope

The magneto-optical Kerr effect (MOKE) microscope is one of the most versatile techniques to image magnetic domains and magnetization processes, which is based on the magneto-optical Kerr effect. On a microscopic level, the Kerr effect is a consequence of the interaction between the electro-magnetic wave comprising the light and the electrons in the medium.

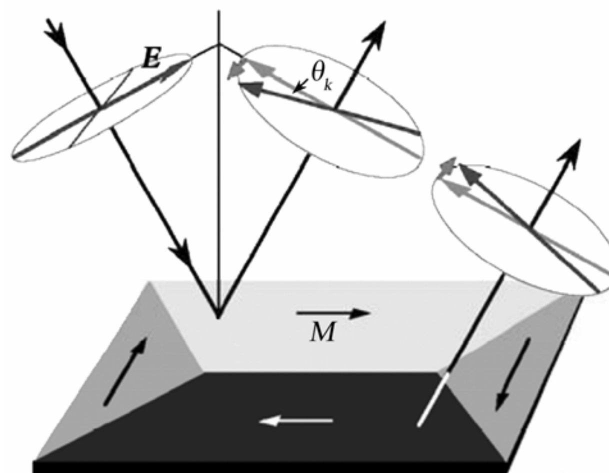

Fig. 2.10. Illustration of the longitudinal Kerr effect [8].

The interaction of a plane-polarized electromagnetic light wave with a magnetic material can be illustrated in an image based on the effect of the Lorentz force on the electrons set in motion by the electrical vector E of the wave. This influence is represented in Fig. 2.10 for the longitudinal Kerr effect. In the same manner, linearly polarized light incident on the surface becomes elliptically polarized, and the rotation angle θ_k is directly proportional to the component of magnetization that is parallel to the reflection surface and parallel to the plane of incidence.

A magneto-optical Kerr microscope is essentially a polarization microscope; the main components are represented schematically in Fig. 2.11. As the magneto-optical contrast is rather weak, a high-pressure mercury lamp was used to produce the high intensive light and significant enhancement is possible by video microscopy and digital image processing. A possible background image subtraction process is best carried out in real time at video frequency, making it possible to view magnetization processes in real-time.

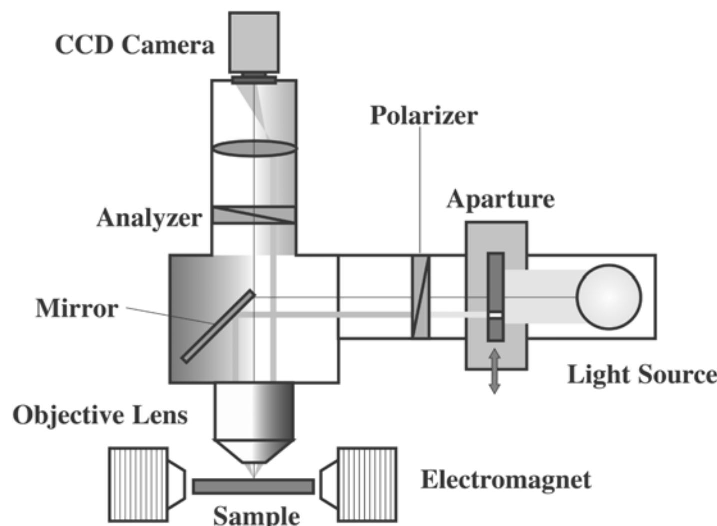

Fig. 2.11. Schematic representation of the main components of a Kerr microscope. The aperture iris is displaced from the optical axis to generate oblique incidence of light.

2.4.3 Transmission Electron Microscope

The transmission electron microscope (TEM) operates on the same basic principles as the optical microscope but uses electrons instead of light. A beam of electrons is transmitted through an ultra thin specimen, interacting with the specimen as it passes through, some of the electrons are scattered and absorbed. The image is formed from the electrons transmitted through the specimen. The magnified image is focused onto an imaging device, such as a fluorescent screen, on a layer of photographic film, or to be detected by a sensor such as a CCD camera.

In this research, the TEM was used to observe the sectional structure of the TMR multilayer film, as shown in Fig. 2.12. The dark areas of the image correspond to areas on the specimen where fewer electrons were able to pass through (either absorbed or scattered upon impact); the lighter areas are where more electrons did pass through, although the varying amounts of electrons in these areas enable the user to see structures and gradients.

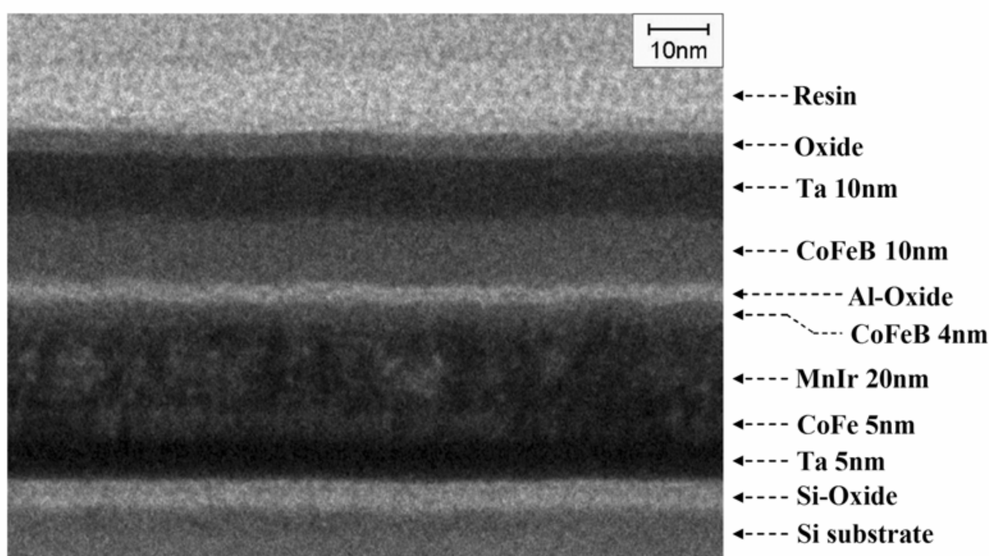

Fig. 2.12. Sectional structure of the TMR multilayer film observed with TEM.

2.4.4 Magneto-resistance Measurement

Generally, the transport properties of GMR multilayer films and MTJ are measured using 4-point probe method, which is an accurate measurement for sample resistance by eliminating the contact resistance and spreading resistance. In the real sensor devices, since the GMR and TMR elements have only two electrodes for each, the MR ratios were measure using a two-point probe method, where the probes for current flowing and voltage measurement were connected in pairs as shown in Fig. 2.13.

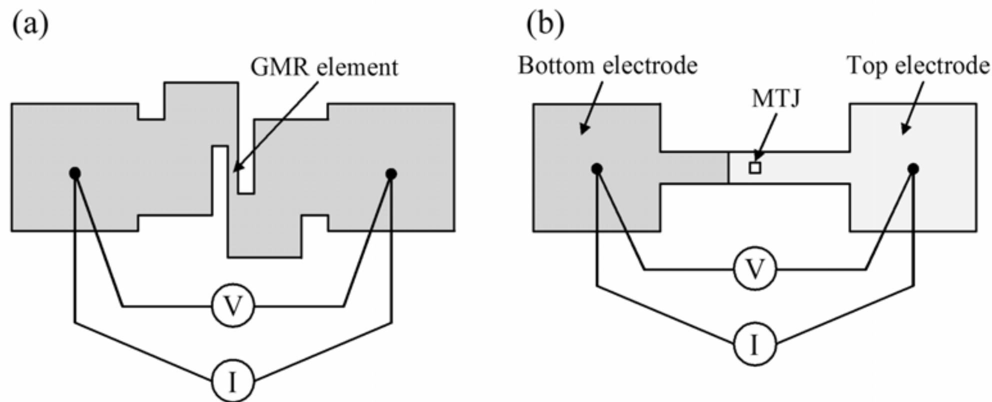

Fig. 2.13. Schematic diagram of the 2-point probe method used for measuring the transport properties of (a) GMR element and (b) MTJ.

TMR effect and tunneling *I-V* characteristic are only happened when a current tunnel through an Al_2O_3 barrier layer, therefore, the current direction must be designed to be perpendicular to the TMR film plane, which is called as current perpendicular to the plane (CPP) measurement. For *I-V* measurements of the junctions, a computer controlled current was applied and the voltage across the barrier was measured. The current was supplied by YOKOGAWA 7651 programmable current source. The voltage was measured using a Keithley 2182 nanovoltmeter. The *I-V* curve was normally taken by

sweeping the current from a negative value to a positive value. Typically *I-V* diagrams were taken in the bias voltage range of -500 to 500 mV. The magnetic field in this system was controlled by a DC power current source. The applied field was measured using a Hall sensor and recorded by a computer. During the magneto-resistance measurement, the sensor element was mounted between two magnetic coils and the MTJ or GMR element was biased with a constant current. The voltage was monitored by sweeping the magnetic field from positive to negative. The bias dependence of the magneto-resistance was obtained by measuring the resistance R (V/I) at various bias voltages for the situation of parallel and anti-parallel alignment of the magnetization direction of the two ferromagnetic layers.

References

[1] G.M. Wallraff and W.D. Hinsberg, Chem. Rev. 99, 1801 (1999).

[2] Unraveling photonic bands: characterization of self-collimation effects in two dimensional photonic crystals, Tsuyoshi Yamashita, Georgia Institute of Technology, Ph.D Dissertation, 2005.

[3] A. A. Tseng, K. Chen, C. D. Chen, and K. J. Ma, IEEE Trans. Electron. Packag. Manuf. 26, 141 (2003).

[4] K. Albrecht, R. Blass, N, Brand, J. Schafer and S. Wolf, Kunststoffe Plast Europe (Germany) 89, 76 (1999).

[5] Teaching materials of Dr. H. Noh, Mechanical Engineering and Mechanics, Drexel University, http://www.mem.drexel.edu/noh.

[6] Fabrication of superconducting nanowire single photon detectors, Joel K. Yang, Massachusetts Institute of Technology, Master Dissertation, 2005.

[7] A. Benninghoven, Surface Science 35, 427 (1973).

[8] A. Hubert and R. Schafer, Magnetic Domains. The Analysis of Magnetic Microstructures. Springer Verlag, Berlin (1998).

Chapter 3

Domain Wall Displacing Type Field Sensor

The domain wall displacing (DWD) type field sensor utilizes the oscillatory domain wall displacement in the ferromagnetic free layer to detect the external field. Since the domain wall displacement is more sensitive to the external field than the magnetization rotation, higher sensitivity compared to the conventional field sensors is expected. To avoid the influence of the wall coercivity in the ferromagnetic materials and the discontinuous domain-wall motion known as Barkhausen effect, an AC field was applied to stimulate the oscillatory domain wall motion in the ferromagnetic free layer and the external field was detected by measuring the shifting of the oscillatory domain wall. The oscillatory domain wall displacement reduces the influence of these two factors, and enables the sensor to detect the magnetic field which is much smaller than the wall coercivity.

3.1 Principle of Domain Wall Displacing Method

The principle of the DWD type field sensor is the utilization of oscillatory domain wall displacement to detect the external field. The domain walls in the ferromagnetic free layer are oscillated by an AC field produced by transmitting an AC current through the Al conducting wire, as shown in Fig. 3.1. The generated AC field H_{ac} can be calculated using

$$H_{ac} = \frac{I}{w\pi} \tan^{-1} \frac{w}{160d} \quad \text{[Oe]} \tag{3.1}$$

where I [A] is the applied current, w [m] is the width of the Al conducting wire, d [m] is the distance between the conducting wire and the free layer. As the distance between the conducting wire and the MTJ or GMR element, d ($\approx$200 nm) << w (100 μm), the field applied on the ferromagnetic free layer can be written as

$$H_{ac} = \frac{I}{160w} \quad \text{[Oe]} \tag{3.2}$$

The oscillatory domain wall motion significantly reduces the influences of the wall coercivity in the ferromagnetic materials and the discontinuous domain-wall motion known as Barkhausen effect. The external field is detected by measuring the shifting of the oscillatory domain wall. If the oscillatory domain wall displacement reduces the influence of wall coercivity and Barkhausen effect, the DWD type sensor can detect the magnetic field much smaller than the wall coercivity. Moreover, the domain wall displacement is more sensitive to the external field than the magnetization rotation, thus higher sensitivity compared to the conventional field sensors can be achieved.

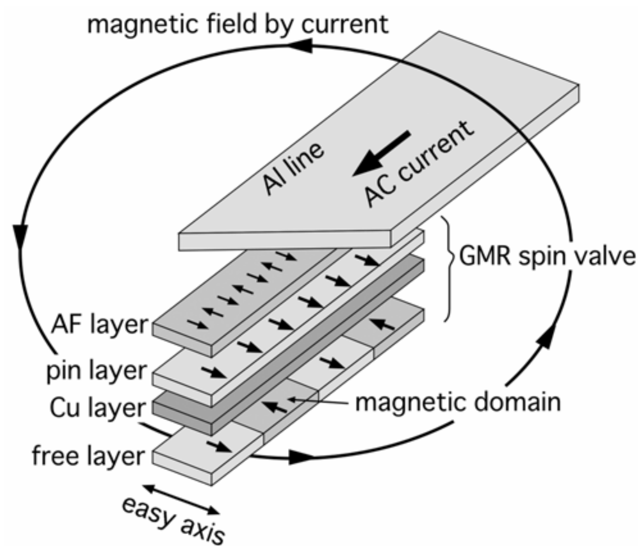

Fig. 3.1. Diagram of oscillatory domain wall method.

Figure 3.2 shows the cartoon of the domain wall displacement in the ferromagnetic free layer for ideal conditions. Driven by an AC field H_{ac}, the domain walls can be oscillated, and the central positions of the oscillatory walls are modified by applying an external field (H_{ex}). Since the domain walls are oscillation-stimulated by the H_{ac}, the central positions of the oscillatory walls can be shifted even if the external field is much smaller then the wall coercivity, and the shifting distance is expected to be proportional to the applied external field. In the actual sensor devices, a bias field is applied to cancel the interlayer coupling exists between the free layer and the pin layer, which may result in the saturation of the ferromagnetic free layer.

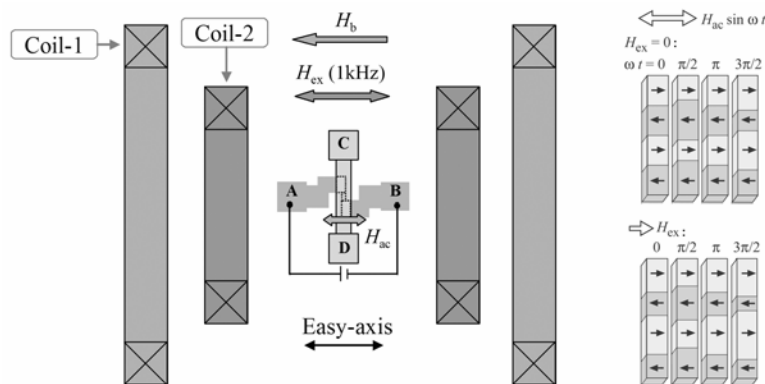

Fig. 3.2. Cartoon of the domain wall displacement in the CoFeB free-layer under zero external field (H_{ex}) and a rightward applied H_{ex}.

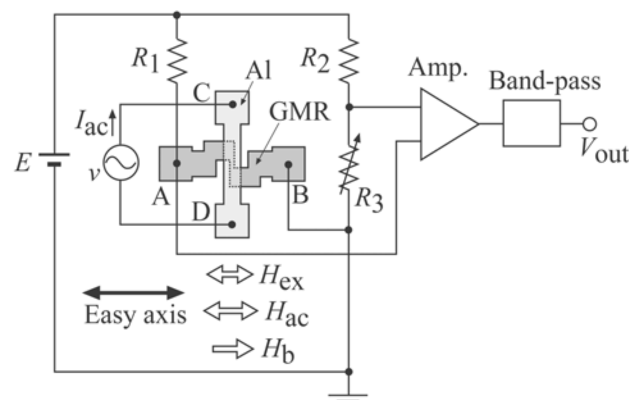

Fig. 3.3. Experimental configuration and electrical circuits for DWD type GMR sensor.

Figure 3.3 shows the experimental arrangement, two independent Helmholtz coils were used to produce a 1 kHz external field (H_{ex}) and a bias field (H_b); both fields were parallel to the easy axis of the GMR element. The H_{ex} acted as a signal field to be detected, and the H_b was used to cancel the coupling between the pin layer and the free layer which causes the saturation of the domain structure in the free layer. DC bias voltage of 1 V was applied to the GMR element (A, B), and an 140 kHz AC current was transmitted through the aluminum conducting wire (C, D) to produce a 140 kHz alternating field H_{ac}. Since the domain walls are oscillation-stimulated by the H_{ac}, the central positions of the oscillatory walls is expected to be shifted even if the external field is much smaller than the wall coercivity, and the shifting distance is proportional to the applied external field. Figure 3.4 shows the predicted signals in the sensor circuit. The bridge signal, contains both 1 kHz and 140 kHz components (as shown in Fig. 3.4 (c)), was amplified using an instrumentation amplifier and the 1 kHz signal was selectively separated by a band-pass/low-pass filter (as shown in Fig. 3.4 (d)).

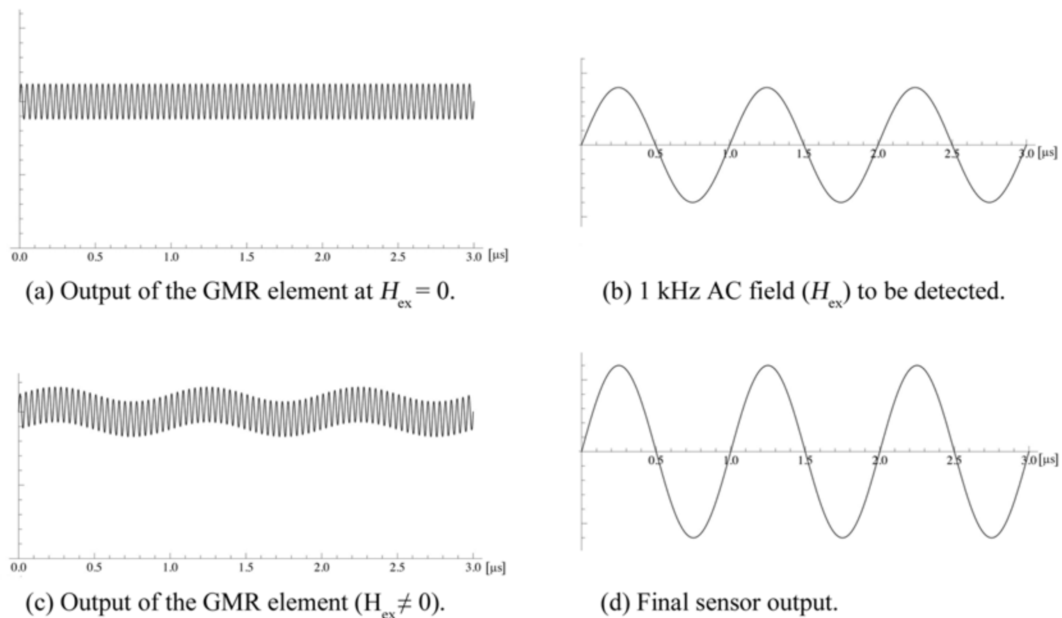

(a) Output of the GMR element at $H_{ex} = 0$.

(b) 1 kHz AC field (H_{ex}) to be detected.

(c) Output of the GMR element ($H_{ex} \neq 0$).

(d) Final sensor output.

Fig. 3.4. Predicted signals in the sensor circuit.

3.2 Fabrication of the DWD Type GMR Sensor

The DWD type GMR sensor devices were fabricated on thermally oxidized silicon wafers, and the GMR multi-layer film: Si wafer / Ta 5 nm / $(Co_{90}Fe_{10})_{92}B_8$ 10 nm/ Cu 2.2 nm / $Co_{90}Fe_{10}$ 3 nm / MnIr 10 nm / Ta 2 nm, was prepared by RF magnetron sputtering at room temperature. A 200-Oe magnetic field was applied during the sputtering to induce the exchange bias field of the pin layer and the magnetic anisotropy of the ferromagnetic free layer. The 200×30-μm spin-valve GMR element with an insulation layer (Al_2O_3, 200 nm thick) and a 250-nm-thick aluminum conducting wire (100 μm in width and 1200 μm in length) were micro-fabricated (as shown in Fig. 3.5).

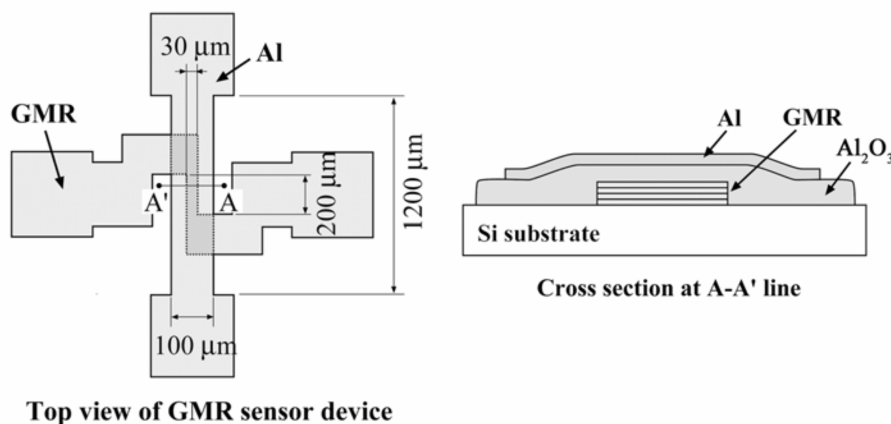

Fig. 3.5. Schematic top view and cross section of the DWD type GMR sensor.

The detailed fabrication process steps are listed as follows:

Step 1: Fabrication of GMR element

The pattern of GMR element was transformed to the multi-layer film by photolithography. The unprotected film regions were etched away by ECR Ar^+ ion etching. After the etching process, a layer of Al_2O_3 was deposited on the etched regions to flatten the surface (as shown in Fig. 3.6). The resist was stripped with a hot remover (photoresist solvent MICROPOSIT REMOVER 1165) at a temperature of 60 °C.

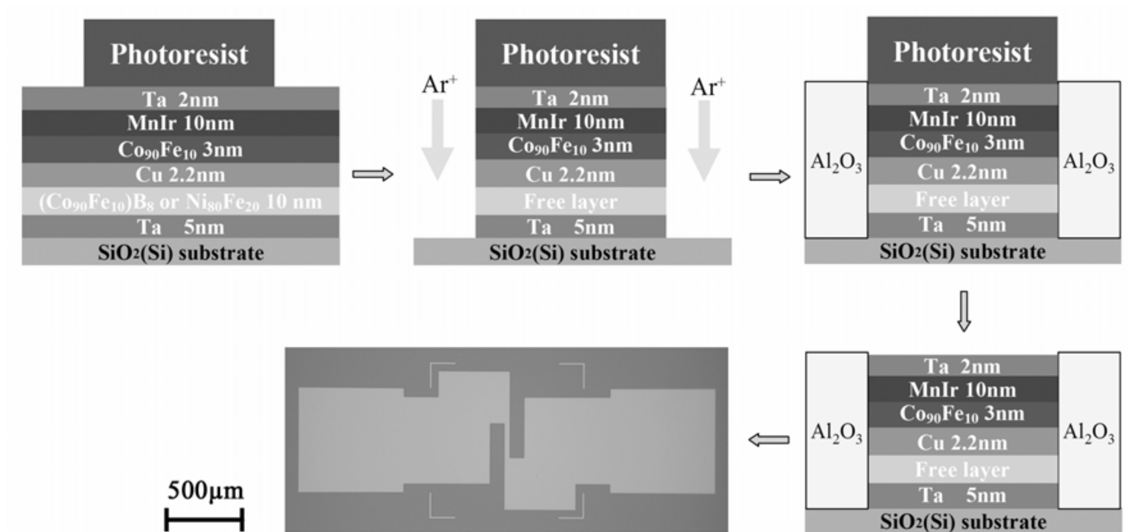

Fig. 3.6. Processes of GMR element fabrication and the optical microscope image of the GMR element.

Step 2: Deposition of insulation layer and Al conducting wire

After the fabrication of the GMR element, an Al_2O_3 insulation layer of 200 nm thick and a 250-nm-thick aluminum conducting wire (100 μm in width and 1200 μm in length) were micro-fabricated onto the GMR element by lift-off process, as shown in Fig. 3.7. The size of the insulation layer was designed slightly larger than the Al conducting wire to prevent the electric short of Al and GMR element due to the adjustment error in photolithography process.

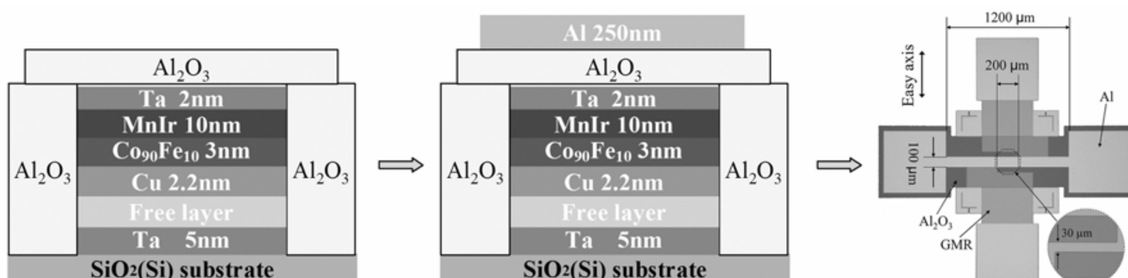

Fig. 3.7. Processes of insulation layer & Al conducting wire deposition and the optical microscope image of finished DWD type GMR sensor device (inset shows the micro-fabricated spin-valve GMR element before the deposition of Al conducting wire).

3.3 Electrical Circuits for DWD Type GMR Sensor

The GMR element of DWD type sensor was connected to a Wheatstone bridge and the applied bias voltages V_b on the GMR element was 1V, as illustrated in Fig. 3.8, the output of the bridge circuit with the GMR sensor was amplified by a low-noise instrumentation amplifier (IA; INA217). Since the amplified signal contained a 140-kHz component (contributed from the wall oscillatory displacement) and a 1-kHz signal component (contributed from the mean position shift of the oscillatory domain walls), the 1-kHz output signal was selectively separated using a 4th-order active low-pass filter (LPF; MAX274). The root-mean-square (RMS) value of the low-pass filter output was measured by a Lock-in Amplifier and defined as V_{out}, and the total gain for the 1 kHz signal component was 50 dB.

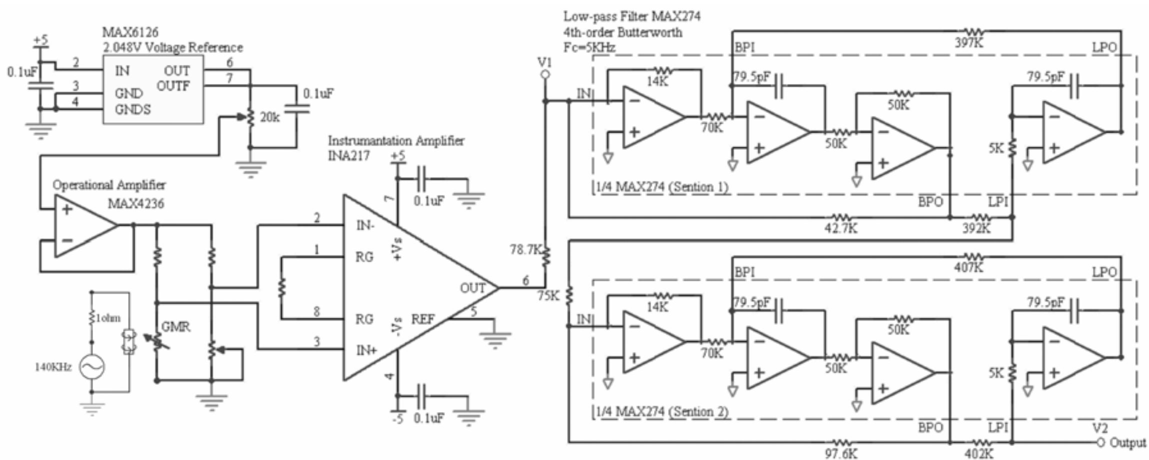

Fig. 3.8. Signal acquisition circuits for DWD type GMR sensor.

The instrumentation amplifier (INA217) is internally composed of 3 op-amps, as shown in Fig 3.9. The bridge outputs are connected to V_{IN}^{+} and V_{IN}^{-}, and the gain can be set with an external resistor connected to RG_1 and RG_2. The IA has a very low noise

about 1.3 nV/Hz$^{0.5}$ at 1 kHz and the bandwidth is about 200 kHz at Gain = 60 dB. As the gain of IA decreases with increasing the input frequency (as shown in Fig. 3.10), in order to utilize the large gain range, the 140 kHz was selected as the frequency of H_{ac}.

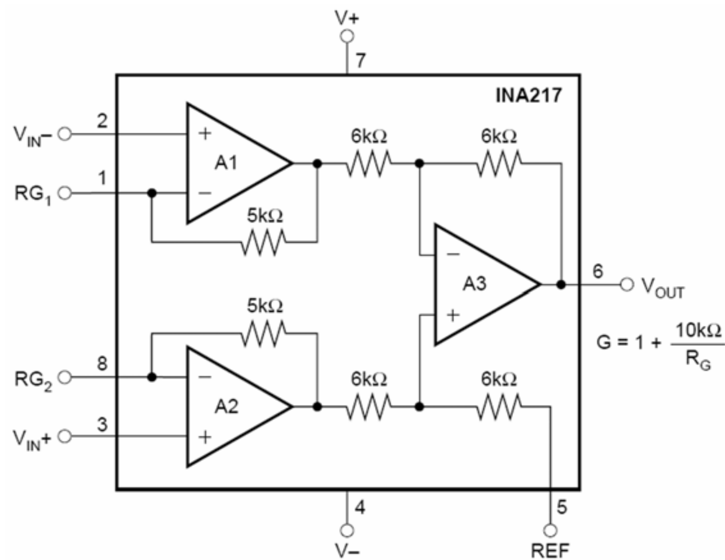

Fig. 3.9. Simplified schematic of INA217 instrumentation amplifier [1].

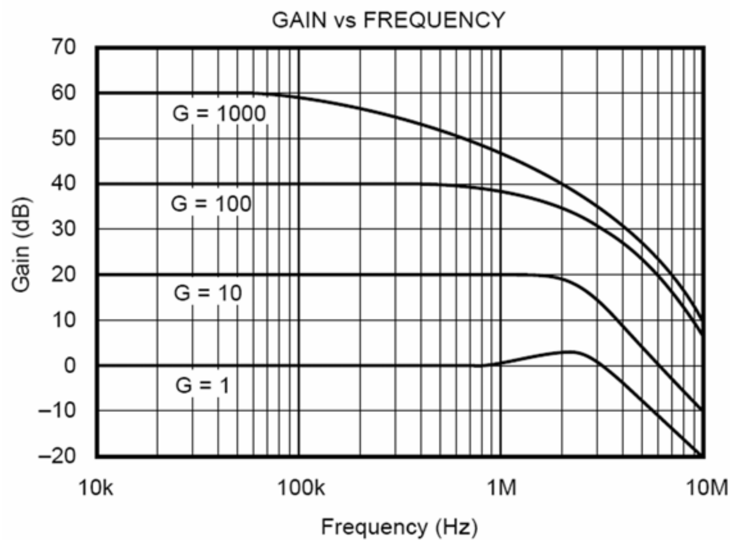

Fig. 3.10. Dependence of the gain on signal frequency [1].

In this research, an integrated filter MAX274 was used to separate the sensor output from the modulated signal. The MAX274 is a continuous-time active filter IC comprises four independent 2nd-order sections. Each section can be implemented as an all-pole band-pass or low-pass filter by four external resistors. Here, two filter sections were connected in series to build a 4-th order low-pass or band-pass filter. In the initial experiments, a band-pass filter was used, and it was later replaced with a low-pass filter with a cut-off frequency (f_c) of 5 kHz. The frequency response for this low-pass filter is illustrated in Fig. 3.11, where a function generator was used to produce a sine test signal (1-500 kHz, 1V RMS), and the root mean square (RMS) value of the output voltage was measured with an oscilloscope.

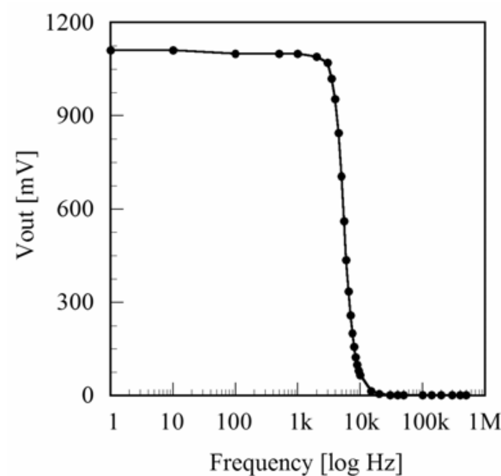

Fig. 3.11. Frequency response of the 4th-order low-pass filter (f_c = 5 kHz).

3.4 Properties of the GMR Sensor Device

The properties of the film stacks and sensor devices were characterized using an AGM and a 2-point probe method. Figure 3.12 shows the *M-H* loop and the minor loop for the GMR film stake measured with an AGM. The coercivity of the 10-nm CoFeB free layer is about 3 Oe (estimated from the minor loop shown in Fig. 3.12 (b)).

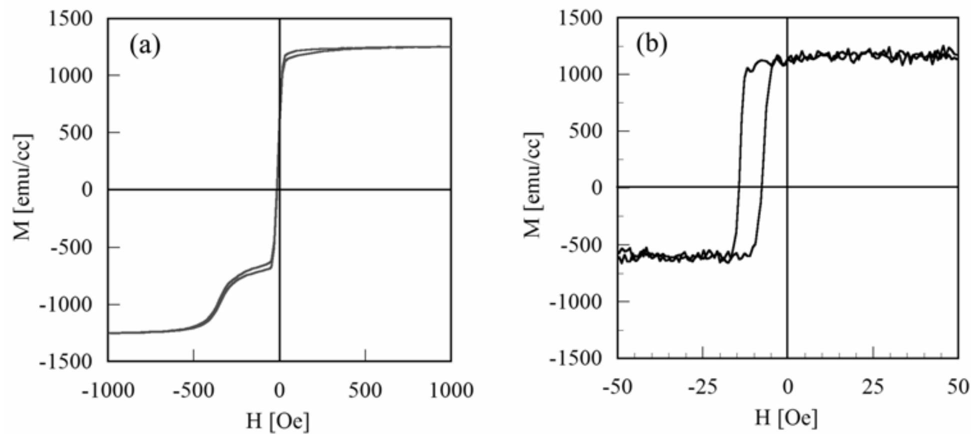

Fig. 3.12. (a) *M-H* loop and (b) minor loop for the GMR film measured with an AGM.

Figure 3.13 shows the MR and minor curves of the micro-fabricated GMR element in easy-axis direction, which were measured by sweeping the applied field from negative to positive and monitoring the voltage of the GMR element. The resistance of the GMR element is about 200 Ω and the element has a MR ratio about 5 %. During the measurement, the bias voltages applied to the GMR element was 1 V.

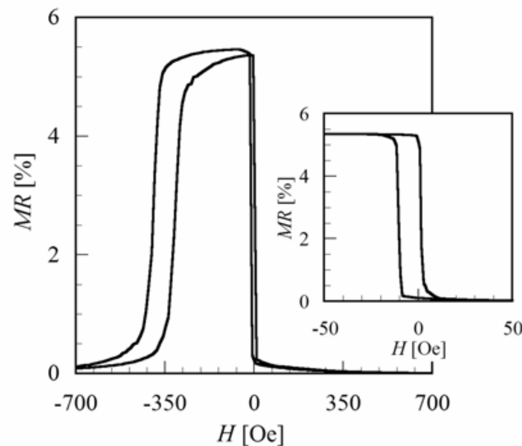

Fig. 3.13. *MR* curves for the GMR element, inset shows the minor loop.

The hard-axis MR curve and the hard-axis M-H loop (as shown in Fig. 3.14) were measured using the same method, where the magnetic field was applied along the hard-axis direction. The uniaxial anisotropy field of the free layer is about 30 Oe.

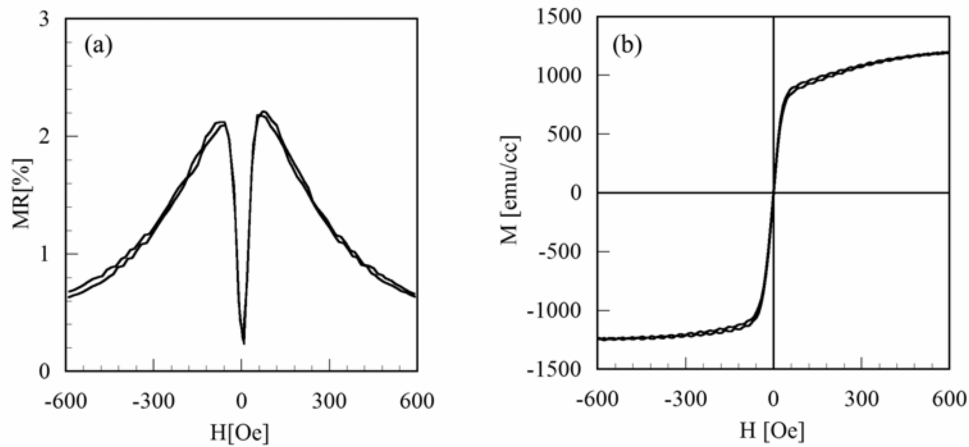

Fig. 3.14. (a) Hard-axis *MR* curve and (b) hard-axis *M-H* loop for the GMR element.

3.5 Domain Structure and Wall Coercivity

Domain structures in the micro-fabricated soft magnetic patterns have been investigated using a magneto-optical Kerr effect microscope. A SiN (40 nm) dielectric layer was deposited onto the micro-fabricated patterns to enhance the magneto-optic Kerr effect [2]. The domain walls in the micro-fabricated patterns can be moved by applying an external field along the easy-axis. Figure .3.15 shows the domain wall structures in the 20-nm-thick (a) $(Co_{90}Fe_{10})B_8$ and (b) $Ni_{80}Fe_{20}$ single-layer patterns (200×30μm) observed with magneto-optical Kerr effect microscope under different applied fields. With increasing the applied field, the domains having the magnetization parallel to the external field were enlarged and finally saturated. The minimum fields to induce the domain-wall displacement for the CoFeB and NiFe samples are almost consistent with the coercivities measured with an AGM.

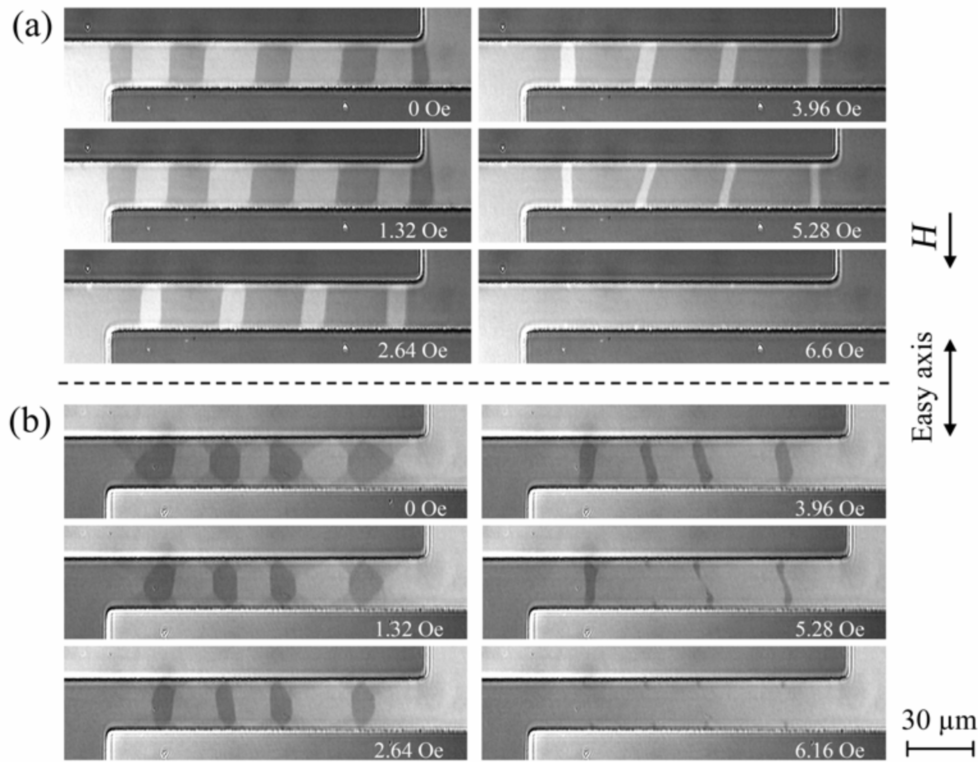

Fig. 3.15. Domain wall structures in the 20-nm-thick (a) $(Co_{90}Fe_{10})B_8$ and (b) $Ni_{80}Fe_{20}$ single-layer patterns (200×30μm) observed with magneto-optical Kerr effect microscope under different applied fields.

3.6 Detection of Oscillatory Domain-wall Displacement

In order to detect the oscillatory domain-wall displacement in the ferromagnetic free layer, the IA output signal was directly observed with a synchroscope. Considering the bandwidth limitation of the IA, a lower-frequency 5 kHz AC current was transmitted through the top aluminum conducting wire to generate an AC field on the GMR element, which drives the domains in the free layer, and a bias field (H_b) of about 4.8 Oe was applied along the easy axis simultaneously. Figure 3.16 shows two waveforms of the IA output under H_{ac} = 2.12 Oe and H_{ac} = 2.5 Oe. In waveform A, the displacement of the domain walls is erratic; this indicates that the alternating field of 2.12 Oe is not sufficient to successively drive the domain walls. By increasing the H_{ac} to 2.5 Oe, (see waveform

B), the domain walls oscillate more regularly. This result also suggests that the wall coercivity of the CoFeB free layer is around 2 Oe, which is consistent with the coercivity measured with the AGM.

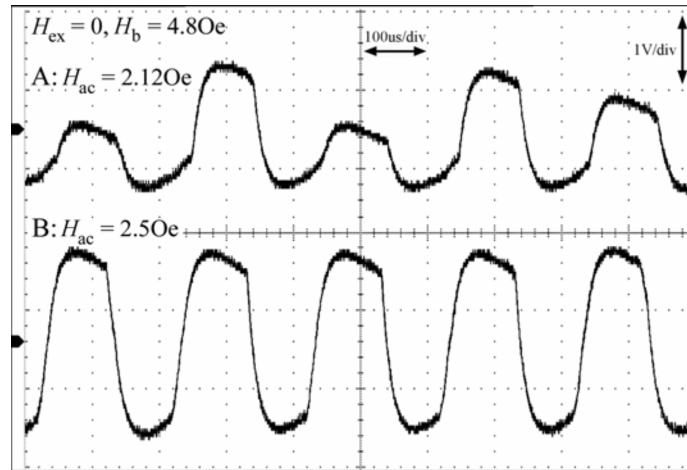

Fig. 3.16. Waveforms of the instrumentation amplifier output under H_{ac} = 2.12 Oe (waveform A) and H_{ac} = 2.5 Oe (waveform B). The frequency of the alternating field (H_{ac}) was 5 kHz. The bias field (H_b) was 4.8 Oe; no external field (H_{ex}) was applied.

The discontinuous domain-wall motion in the ferromagnetic free layer (known as Barkhausen effect) was also observed using a synchroscope. In this experiment, a 5.12 Oe DC bias field H_b was applied along the easy axis of the GMR element to cancel the coupling between the pin layer and the free layer. A 100 Hz square-wave AC field (with a rising and falling time of 2 ms) and a 50 kHz sine AC field were applied along the easy axis of the GMR element to drive the domain walls in the free layer. Figure 3.17 shows the waveforms of the applied square-wave 100 Hz AC field and the IA output. This waveform shows that the walls move abruptly when the applied field exceeds a certain threshold value, which is due to the coercivity of free layer. In addition, on both rising and falling edges of the IA output many dentate jumps can be observed, which indirectly

reflects the discontinuous domain wall motion in the CoFeB free layer. Because the wall velocity is fast enough to follow the frequency of H_{ac} (up to several hundred kHz), when increasing the frequency of applied field to 50 kHz and using the sine wave-form (as shown in Fig. 3.18), the IA output is still square wave. If assuming there are 8 domain walls exist in the 200-μm-long CoFeB free layer and the rising and falling time of the IA output are about 2 μs, and the displacing distance for each domain wall is 10 μm, the calculated domain-wall displacing speed is about 5 m/s, which is smaller than the estimated maximum domain wall speed (about 50 m/s) calculated with equation (1.5).

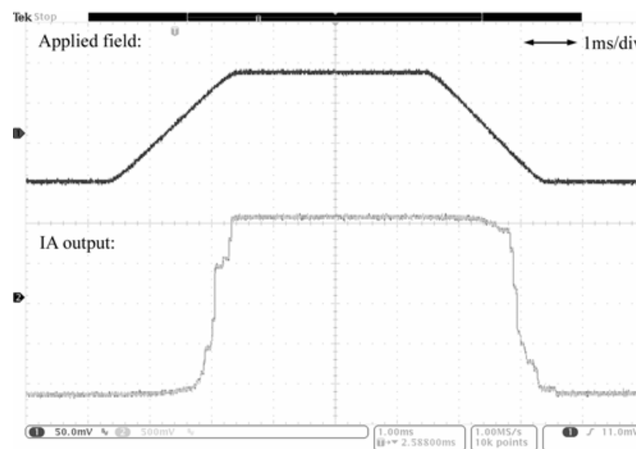

Fig. 3.17. Waveforms of the applied 100 Hz AC field and the IA output.

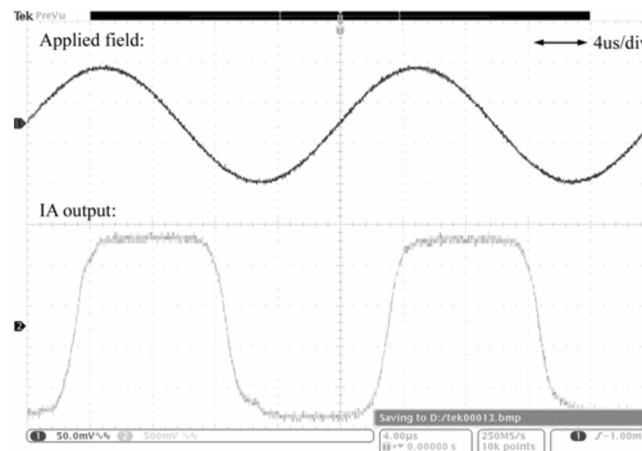

Fig. 3.18. Waveforms of the 50 kHz applied field (sine wave) and the IA output.

3.7 Field Detection by Oscillatory Domain-wall Displacement

According to the operational principle of the DWD type sensor, if the domain walls in the CoFeB free layer are saturated, the sensor should have no response to the external field. Fig. 3.19 shows the dependence of 1 kHz output voltage V_{out} on the bias field H_b. As the H_b increases from -20 Oe to +20 Oe, the V_{out} appears in the range of 3.5 to 9 Oe and takes a maximum at H_b = 6.4 Oe. This result implies that the domain walls are introduced into the CoFeB free layer within this bias field range. The reason of the necessity for a bias field H_b is due to the orange peel coupling between the free and pin layers. The bias field H_b of 6.4 Oe almost corresponds with the loop shift of the MR minor loop shown in Fig. 3.13

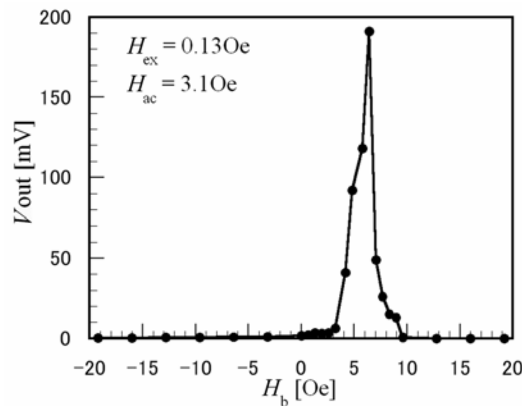

Fig. 3.19 Dependence of the 1-kHz signal output voltage (V_{out}) on the bias field H_b.

Figure 3.20 shows the field dependence of 1 kHz V_{out} under different H_{ac} fields. Curves A and B were measured at H_{ac} = 3.1Oe (I_{ac} = 50 mA, RMS) and H_{ac} = 0.93 Oe (I_{ac} = 15 mA, RMS), respectively. For both measurements, a 6.4-Oe bias field (H_b) was applied. For curve B, there is no output until H_{ex} = 2 Oe, and V_{out} starts to increase when H_{ex} > 2 Oe. This non-linear behavior implies that the H_{ac} is insufficient to drive the domain walls in the free layer since the wall coercivity of the CoFeB free layer is around

2.5 Oe, estimated from a minor loop of the CoFeB layer measured with the AGM. On the other hand, in curve A and the inset of Fig. 3.20, a linear relationship between H_{ex} and V_{out} is observed, which indicates that the domain walls oscillate successively under the H_{ac} of 3.1 Oe, and that the output V_{out} is proportional to the external field even though the external field is much smaller than the coercivity of the CoFeB free layer. According to curve A, the field sensitivity is about 2.65mV/V/Oe. Moreover, we have analyzed the frequency spectra (FFT) of the band-pass filter output, and the minimum external field H_{ex} that can be distinguished from the background noise is about 0.21 mOe.

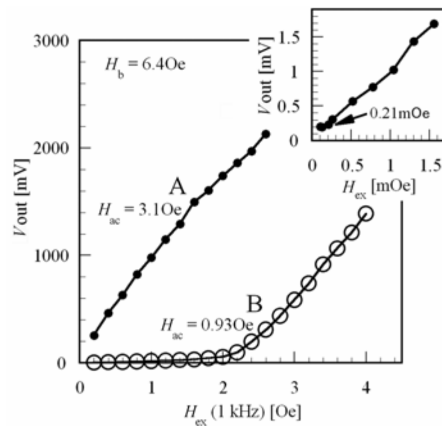

Fig. 3.20 Relationship between the 1-kHz external field (H_{ex}) and the output voltage under different 140-kHz AC fields (H_{ac}). Inset shows V_{out} vs. small H_{ex}.

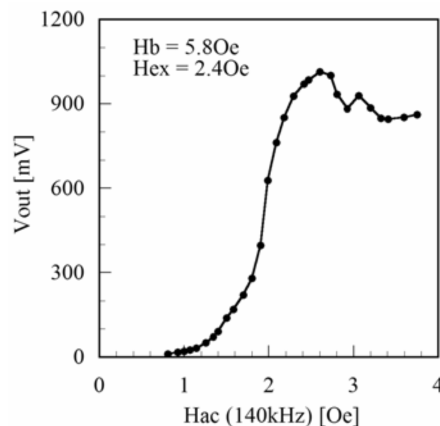

Fig. 3.21. Dependence of the 1 kHz V_{out} on 140 kHz H_{ac}.

Figure 3.21 shows the dependence of the 1 kHz V_{out} on 140 kHz H_{ac} under a 2.4 Oe external field. The V_{out} appears at H_{ac} = 0.8 Oe becomes stable when H_{ac} > 3 Oe, which indicates that the domain walls in the free layer can be oscillated by applying a 3 Oe or larger H_{ac}. The V_{out} vs. H_{ex} under different frequencies are illustrated in Fig. 3.22, the V_{out} keeps constant when the frequency of H_{ex} varies from 10 Hz to 3 kHz. This is because the wall velocity under a signal frequency less than 3 kHz is much lower than the maximum velocity given by equation (1.5).

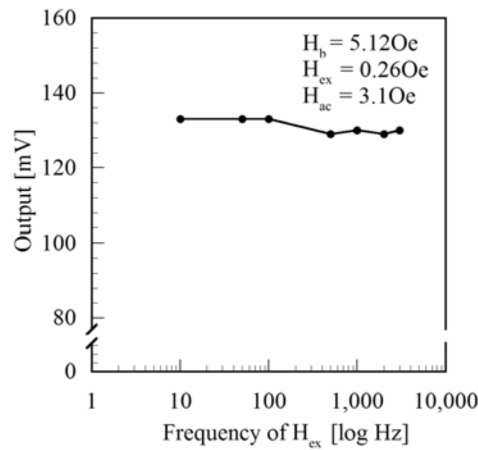

Fig. 3.22. Dependence of the 1 kHz V_{out} on the frequency of H_{ac}.

The waveforms of the applied 1 kHz H_{ex} and the V_{out} under different H_{ex} intensities are illustrated in Fig. 3.23. The sine wave output becomes distorted when external field decreased to about 4.6 mOe. Figure 3.24 shows the frequency spectra (FFT) of the 1 kHz V_{out} under different H_{ex} intensities, the background noise is about 0.2 mOe in terms of magnetic field. Since the domain structure can be induced into the free layer by applying a 4.8 Oe H_b, the sensor becomes more sensitive to the external field and the noise level is about 2 times larger than it for H_b = 0 case (as shown in Fig. 3.25).

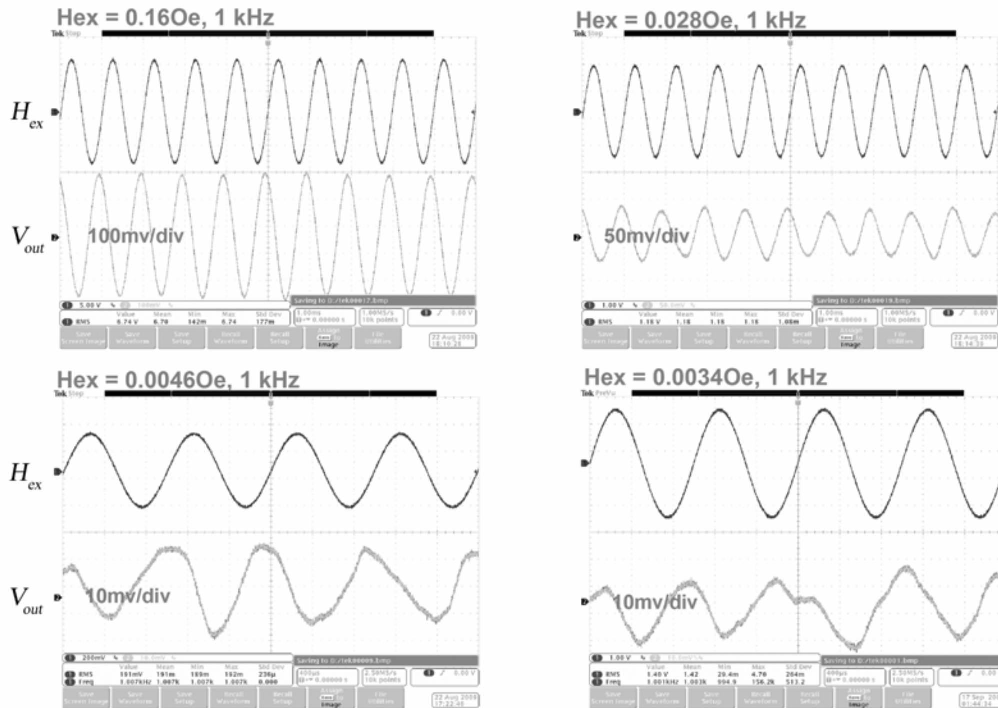

Fig. 3.23. Waveforms of the applied 1 kHz H_{ex} and the V_{out} under different H_{ex} intensities.

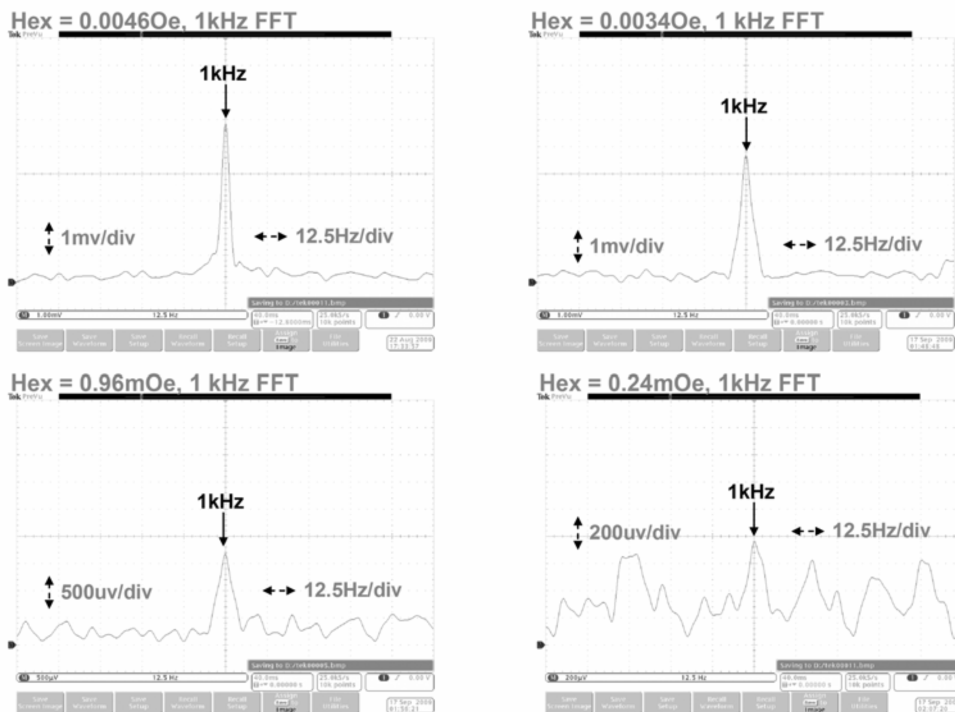

Fig. 3.24. Frequency spectrs (FFT) of the 1 kHz V_{out} under different H_{ex} intensities.

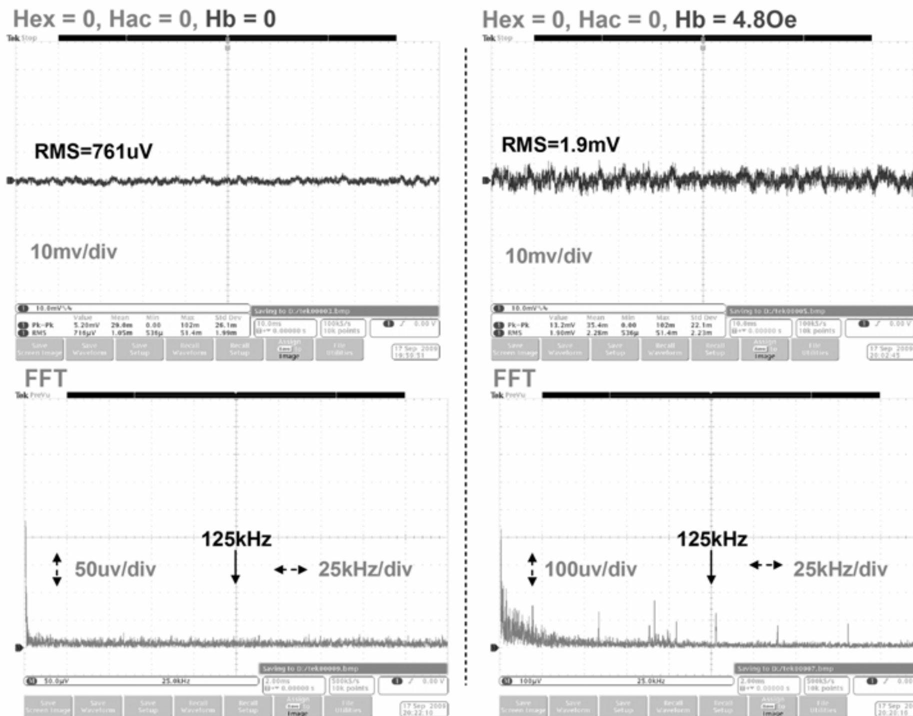

Fig. 3.25. Waveforms and frequency spectrs (FFT) of the background noise under $H_b = 0$ and $H_b = 4.8$ Oe.

Moreover, the domain wall displacement distance by applied field is about 15μm/Oe (estimated from Fig. 3.15 (a)). The detectable field (about 0.21 mOe) corresponds to about 3 nm domain wall displacement. The fluctuation of wall position due to the thermal agitation and/or environmental magnetic field noise (few nanometers) may be an origin of the background noise when walls were introduced into the free layer.

3.8 Field Detection by Magnetization Rotation

The same DWD type GMR sensor element (with a 10 nm CoFeB free layer) was operated in magnetization rotation sensing mode to compare the field resolution and sensitivity with the DWD mode. In this experiment, two Helmholtz coils were arranged perpendicular to each other (as shown in Fig. 3.26), coil-1 was used to apply a DC bias

field H_b perpendicular to the easy axis, which saturates the free-layer magnetization orthogonal to the easy axis. The 1 kHz external field H_{ex} was applied using coil-2 along the easy axis to rotate the free-magnetization form the hard axis. The applied bias voltage on the GMR element was about 380 mV. The output signal of the IA (Gain = 59.7 dB) was detected with a synchroscope. Before starting the measurement, the IA output (V_{out}) was adjusted near zero by balancing the Wheatstone bridge.

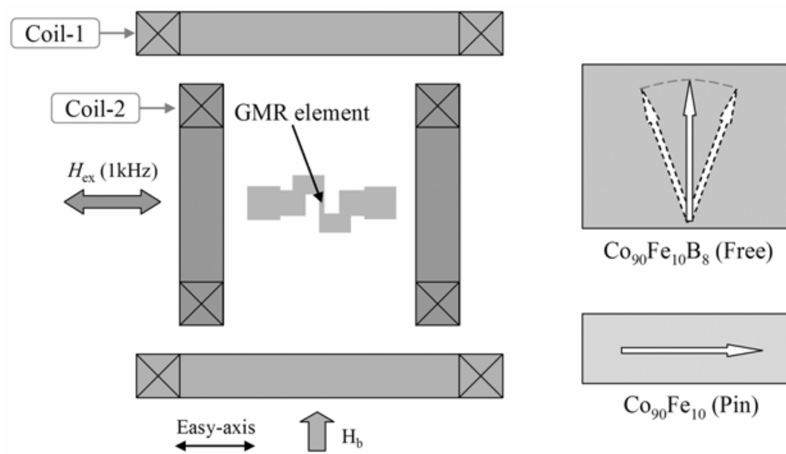

Fig. 3.26. Experimental configuration for magnetization rotation mode.

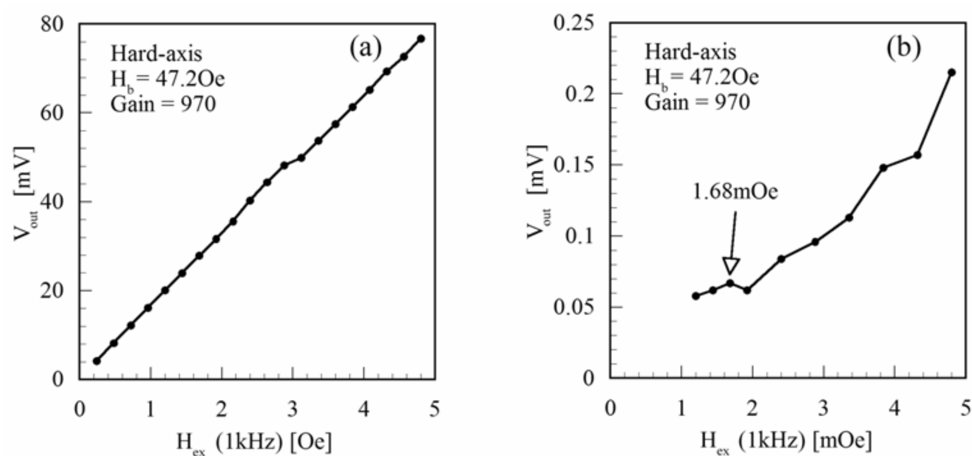

Fig. 3.27. Dependence of the output voltage V_{out} on the applied external field H_{ex} when the GMR sensor was operated under the magnetization rotation mode.

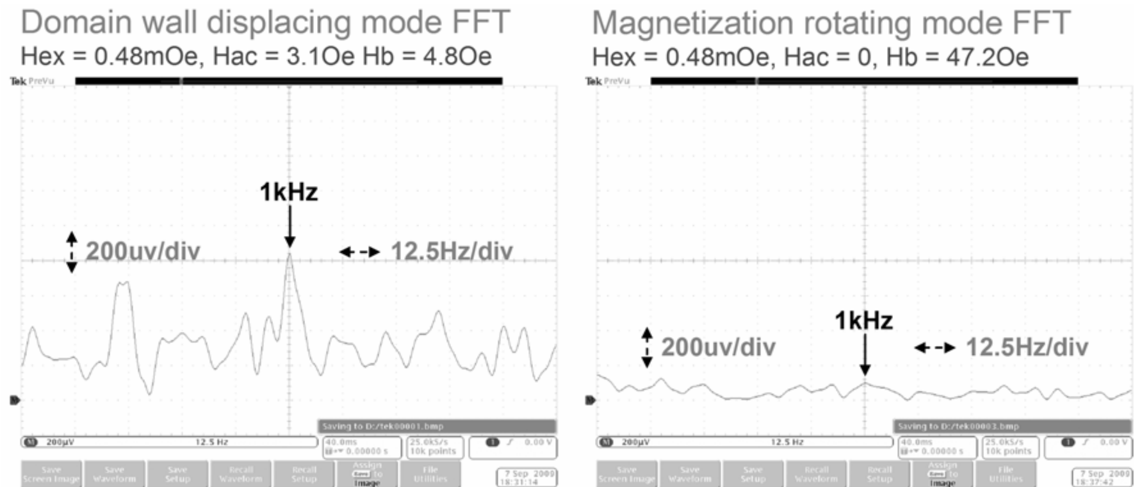

Fig. 3.28. Comparison of the background noises for domain wall displacing mode and magnetization rotation mode.

Figure 3.27 shows the output voltage V_{out} vs. applied external field, where a 47.2 Oe bias field H_b was applied. The calculated field sensitivity from the slope is about 43 μV/(V·Oe), which is much smaller than that for the DWD mode (2.65 mV/(V·Oe)). However, the DWD mode has higher noise level (as shown in Fig. 3.28), which may be caused by the irregular domain wall motion in the ferromagnetic free layer.

3.9 Investigation of Shape and Materials for Free Layer

3.9.1 Domain Structure in Ferromagnetic Thin Films

In this section, domain structures in various micro-fabricated soft magnetic patterns have been investigated using a magneto-optical Kerr effect microscope. As described in section 3.5, a SiN (40 nm) dielectric layer was deposited onto the micro-fabricated patterns to enhance the magneto-optic Kerr effect. The purpose of observing the domain structures in various magnetic patterns is to find out a proper free layer for the DWD type sensor.

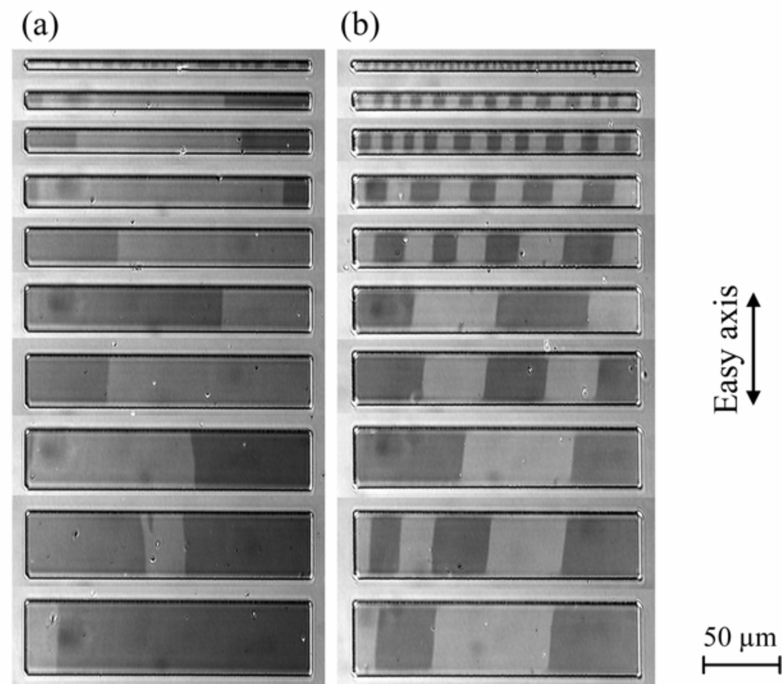

Fig. 3.29. Domain wall structure of (a) $(Co_{90}Fe_{10})B_8$ 10nm (b) $(Co_{90}Fe_{10})B_8$ 20nm single layer patterns.

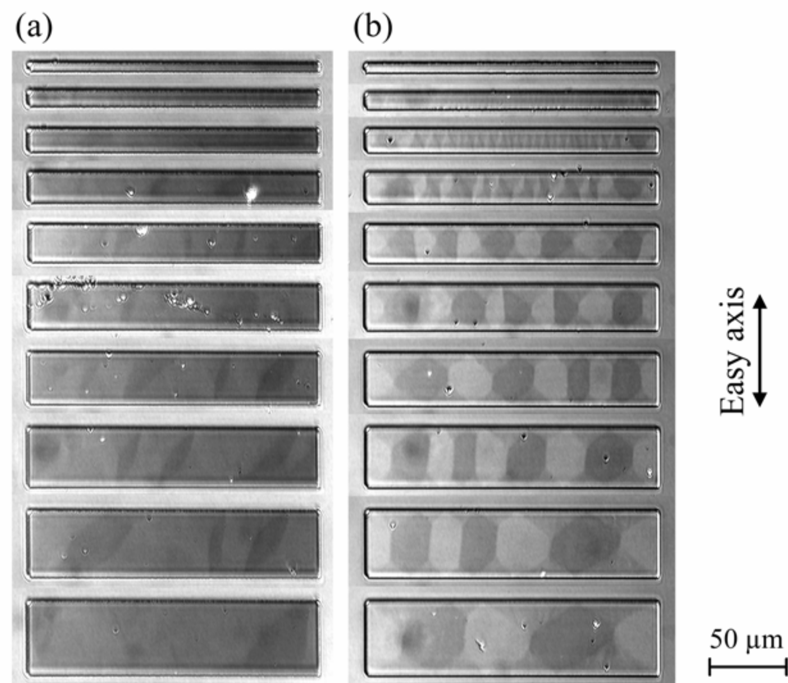

Fig. 3.30. Domain wall structure in (a) $Ni_{80}Fe_{20}$ 10nm (b) $Ni_{80}Fe_{20}$ 20nm single layer patterns.

Domain structures in CoFeB single layer and NiFe single layer patterns are illustrated in Fig. 3.29 and Fig 3.30, the number of domains increases with decreasing of the width of patterns and more domains are formed in the thicker samples, which is due to the increase of magneto static energy and more domains are tend to be formed to keep the minimum energy. In this research, two typical free-layer materials were selected to fabricate the GMR sensor devices: 10 nm $(Co_{90}Fe_{10})_{92}B_8$, which has only two rectangle domains inside, and 10 nm Ni80Fe20, which has a closure domain structure.

The magnetic domain structure tends to minimize the sum of domain wall energy and magnetostatic energy. In CoFeB films, the width of rectangular domains became narrower as increasing the thickness of CoFeB films or as decreasing the width of the patterns in order to reduce the demagnetizing field generated by the magnetic poles in the edges. In NiFe films, closure domains were formed due to the further reduction of the magnetostatic energy. The reason is considered to be the small magnetic anisotropy and the low domain wall energy density of the NiFe films.

3.9.2 Magnetic Property of Ferromagnetic Thin Films

The magnetic property of ferromagnetic thin films was characterized using an alternating gradient-field magnetometer (AGM) introduced in section 2.4, where the field gradient was set at 0.15 Oe/mm. Figure 3.31 shows the easy-axis and hard-axis *M-H* loops for the ferromagnetic single layers and coupled layers, which were used as the samples for domain structure observation. In the case of CoFeB, the clear uniaxial magnetic anisotropy about 50 Oe and 25 Oe were induced in the 10-nm-thick and 20-nm-thick film, and the coercivities were 4 Oe and 2 Oe, respectively. In the case of NiFe, the clear uniaxial magnetic anisotropy was not observed in the 10-nm-thick films,

but the anisotropy field and the coercivity in the 20-nm-thick NiFe films were 3.5 Oe and 1 Oe, respectively. Both parameters were lower than that for CoFeB films. When considering the application of magnetic field sensor, in general, the NiFe has an advantage because of its lower coercivity.

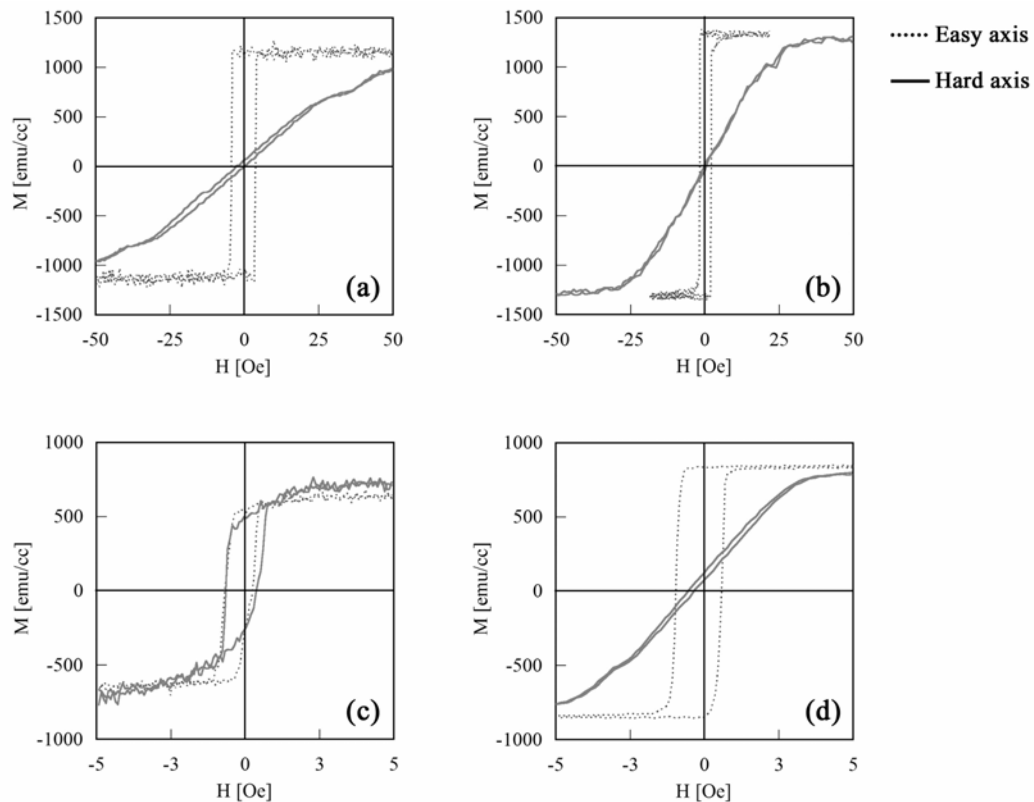

Fig. 3.31. Easy-axis and hard-axis *M-H* loops for the ferromagnetic single layers and coupled layers: (a) $(Co_{90}Fe_{10})B_8$ 10nm, (b) $(Co_{90}Fe_{10})B_8$ 20nm, (c) $Ni_{80}Fe_{20}$ 10nm and (d) $Ni_{80}Fe_{20}$ 20nm.

3.9.3 Dependence of the Minor Loop on GMR element width

The domain structure in ferromagnetic patterns is not only depended on the material but also be affected by the pattern width, where the number of domain increases with decreasing of the pattern width. To investigate the influence of element width on MR loop, GMR elements with width from 15-45μm were micro-fabricated using EB

lithography and Ar^+ ion etching techniques. The elements were measured with a 2-point probe method by applying a bias voltage of 1V.

The GMR films used in this experiment have the following layer structures: (a) Si wafer / Ta 5 nm / $(Co_{90}Fe_{10})_{92}B_8$ 10 nm / Cu 2.2 nm / $Co_{90}Fe_{10}$ 3 nm / MnIr 10 nm / Ta 2 nm, (b) Si wafer / Ta 5 nm / $(Co_{90}Fe_{10})_{92}B_8$ 20 nm / Cu 2.2 nm / $Co_{90}Fe_{10}$ 3 nm / MnIr 10 nm / Ta 2 nm. Figure 3.32 shows the minor loops for the GMR elements with width from 15-45 μm and the comparison of slopes under different element width. The sample has a free layer of 10-nm-thick $(Co_{90}Fe_{10})_{92}B_8$. The slope of minor loop for the wider GMR element is steeper than that for the narrower element. For the sample, which has a free layer of 20-nm-thick $(Co_{90}Fe_{10})_{92}B_8$ and lower coercivity, the situation is similar (as shown in lower right of Fig. 3.33). This result indicates that the domain wall displacement in the wider GMR elements is easer than it in the narrow elements, and the coercivity can be reduced by increasing the thickness of the free layer. In the GMR multilayer, the MR ratio is mainly contributed from the electrons traveling across the FM / Cu / FM interface. But for the GMR elements with 20 nm free layers, more electrons travel through the free layer instead of traveling across the Cu interface, the MR ratio is smaller than those elements with 10 nm free layer.

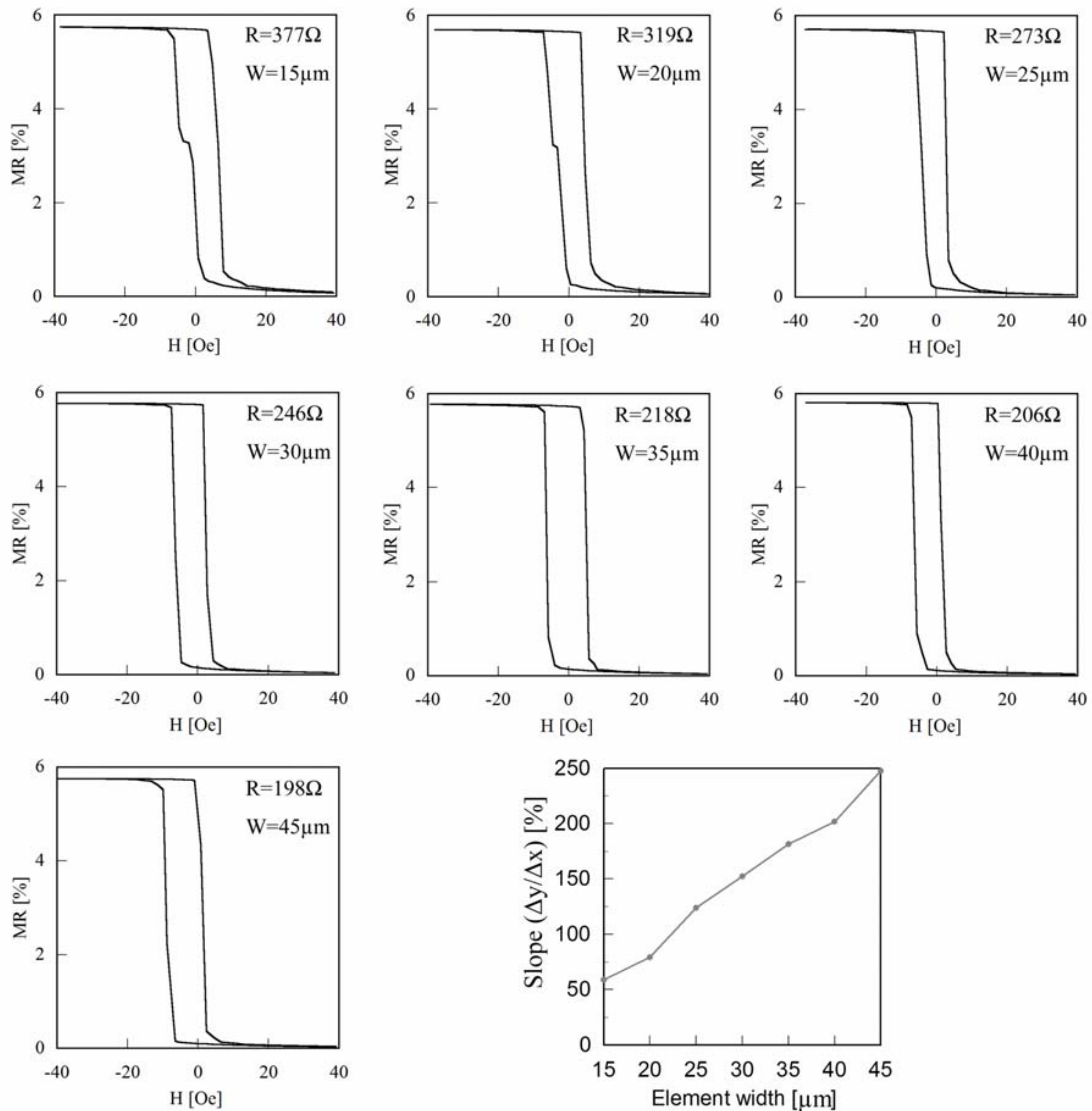

Fig. 3.32. Minor loops for the GMR elements with different widths. The GMR elements have the following layer structure: Si wafer / Ta 5 nm / $(Co_{90}Fe_{10})_{92}B_8$ 10 nm / Cu 2.2 nm / $Co_{90}Fe_{10}$ 3 nm / MnIr 10 nm / Ta 2 nm, the lower right figure shows the slope dependence on element width.

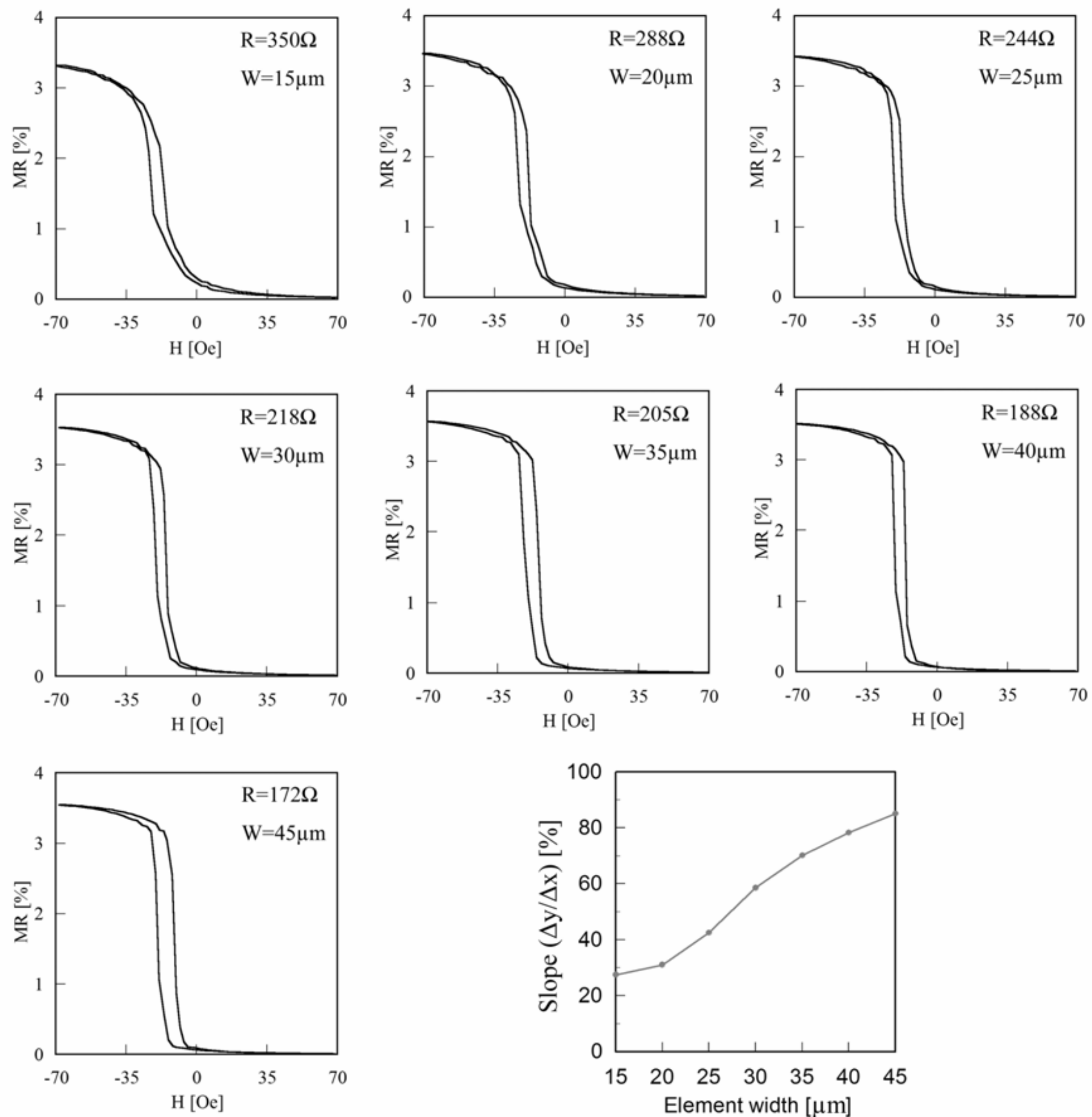

Fig. 3.33. Minor loops for the GMR elements with different widths. The GMR elements have the following layer structure: Si wafer / Ta 5 nm / $(Co_{90}Fe_{10})_{92}B_8$ 20 nm / Cu 2.2 nm / $Co_{90}Fe_{10}$ 3 nm / MnIr 10 nm / Ta 2 nm, the lower right figure shows the slope dependence on element width.

3.9.4 Influence of Free-layer material on Sensor Output

For the DWD type sensor, the soft magnetic material of the free layer plays an import role, and the sensor output is mainly determined by the domain-wall displacement in the free layer. In this section, dependence of sensor properties on free-layer material was investigated using the spin-valve GMR element with layer structure: Si wafer / Ta 5

nm / $(Co_{90}Fe_{10})_{92}B_8$ 10 nm or $Ni_{80}Fe_{20}$ 10nm / Cu 2.2 nm / $Co_{90}Fe_{10}$ 3 nm / MnIr 10 nm / Ta 2 nm. Figure 3.34 shows the MR loops of the micro-fabricated 200×30-μm GMR elements with a 10 nm NiFe free layer (solid line) or a 10 nm CoFeB free layer (dashed line). The MR ratios of these two GMR elements were 4.2% and 5.5%, respectively. By comparing minor loops shown in the inset of Fig. 3.34, the 10 nm NiFe free layer has a larger saturation field than that for the CoFeB, which may be attributed to the magnetization rotation of the closure domains in the NiFe free layer, and for the 10 nm CoFeB free layer, the magnetization change is mainly caused by the domain-wall displacement. Since the domain-wall displacement is more sensitive to the external field than the magnetization rotation, the GMR element with a CoFeB free layer has a steeper MR loop.

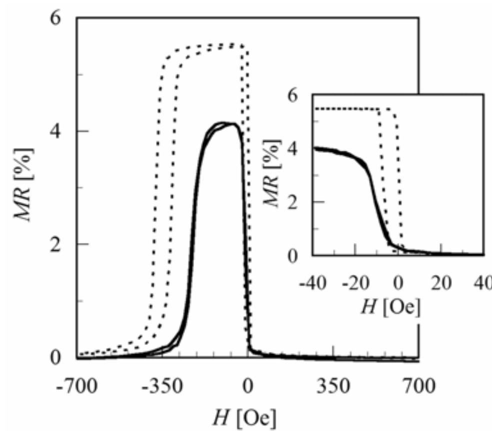

Fig. 3.34. MR loops of the micro-fabricated 200×30 μm GMR elements with a 10 nm NiFe permalloy free layer (solid line) or a 10 nm CoFeB free layer (dashed line).

Figure 3.35 shows the dependence of 1 kHz V_{out} on the bias field H_b for the DWD type sensor with a 10 nm NiFe free layer (open symbols) or a 10 nm CoFeB free layer (closed symbols). By sweeping the H_b from 20 Oe to negative, the sensor with a CoFeB free layer exhibits large V_{out} in the H_b range of 0 to -9 Oe and a maximum V_{out} at H_b = -6

Oe, and for the sensor, which has a 10 nm NiFe free layer, the V_{out} takes a maximum at H_b = -9.8 Oe. This result indicates that the domain structure can be introduced into the soft magnetic free layer within a certain bias field range and the oscillatory domain-wall displacement may reach the maximum when the interlayer coupling field between the pin layer and free layer are completely canceled by the H_b.

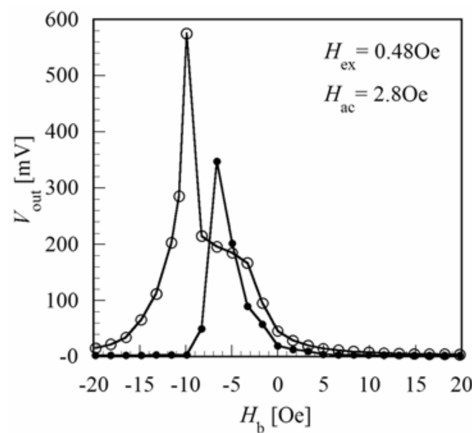

Fig. 3.35. Dependence of the 1 kHz V_{out} on the bias field H_b for the DWD type sensors with a 10 nm NiFe free layer (open symbols) or a 10 nm CoFeB free layer (closed symbols). The H_b swept from 20 Oe to -20 Oe.

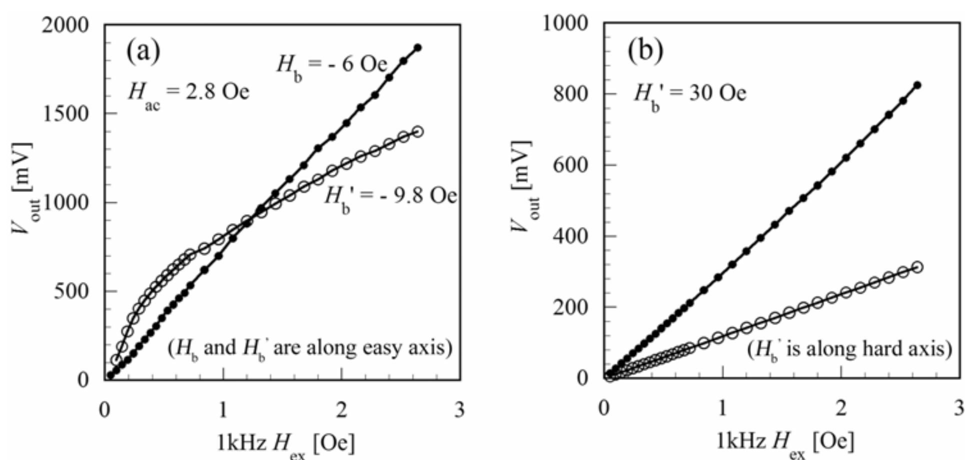

Fig. 3.36. Dependence of the sensor output (V_{out}) on 1 kHz external field (H_{ex}) for the sensor which has a 10 nm NiFe free layer (open symbols) or a 10 nm CoFeB free layer (closed symbols). The sensor devices were operated under (a) domain-wall displacement mode and (b) magnetization rotation mode.

Figure 3.36 shows the dependence of the sensor output V_{out} on 1 kHz external field H_{ex} for the sensor which has a 10 nm NiFe free layer (open symbols) or a 10 nm CoFeB free layer (closed symbols). The sensor devices were operated under (a) domain-wall displacement mode and (b) magnetization rotation mode. Under the DWD mode, the sensor with a 10 nm NiFe free layer shows a higher field sensitivity (about 4.2 mV/(V·Oe)) than that with a 10 nm CoFeB free layer, but the sensor output becomes saturated when the external field $H_{ex} > 0.4$ Oe.

As shown in Fig. 3.30 (b), the NiFe pattern has many domains inside, and the output in the DWD mode will be enhanced by the numbers of the domains in the free layer. Moreover, the wall coercivity of NiFe is much smaller than that of CoFeB, i.e., the domain walls in the NiFe are quite sensitive to the external field. However, the NiFe has many domains inside and the small wall coercivity may cause the saturation of the wall displacement easily. For the sensor, which has a 10 nm $(Co_{90}Fe_{10})_{92}B_8$ free layer, since there are rectangular domains exist in the free layer, the dynamic range of the domain wall displacement is larger than it is in the 10 nm NiFe free layer, and the sensor output is linear even H_{ex} increases to 2.6 Oe. For the magnetization rotation mode, as shown in Fig. 3.36 (b), the NiFe has small anisotropy field compared to CoFeB, so that the rotation angle of the magnetization in NiFe by applying a H_{ex} along the easy axis will be smaller than that in CoFeB, which results in the smaller V_{out} in the NiFe device. By comparing the sensor outputs under the DWD mode (Fig. 3.36 (a)) and conventional magnetization rotation mode (Fig. 3.36 (b)), the DWD mode shows at least 2 times higher field sensitivity.

3.10 Fabrication of DWD type TMR Sensor

Both the DWD type GMR and TMR sensors shared the same photolithography process, which has been discussed in section 2.3. The detailed processes for the photolithography pattern transfer used here are listed as follows:

1) Silicon wafers were cleaned in an ultrasonic bath using isopropyl alcohol (IPA) for 5 min. Then the wafers were dried in the convectional oven at 170 °C for 2 minutes.
2) The positive resist of SHIPLEY (S1813) was spin-coated with 1000 rpm for 10 seconds and with 5000 rpm for 35 seconds.
3) The photo-resist was pre-baked at 110°C for 10 minutes in the convectional oven.
4) Resist layer was exposed to the mixed light of g-line (436 nm), h-line (405 nm) and i-line (365 nm) offered by high pressure Hg lamp using mask alignment (MIKASA M-10). The light power was 250W and the typical exposure time was 7 seconds.
5) Post exposure bake was performed at 90 °C for 20min.
6) The exposed sample was developed in SHIPLEY MF CD-26 DEVELOPER. The sample was soaked for 15 sec and agitated for 45 sec. in the developer, followed by puddling in pure water for 1 minute.

The DWD type TMR sensor has the similar structure as the DWD type GMR sensor, it consists of a magnetic tunnel junction (MTJ) and an aluminum conducting wire placed on it with an insulation layer between them. The sensor device was fabricated on a thermally oxidized silicon wafer with 500 nm SiO_2 and a total thickness of 525 μm, and the multi-layer film with a stack of (Si wafer / Ta 10 nm / $Co_{90}Fe_{10}$ 5 nm / MnIr 10 nm / $(Co_{90}Fe_{10})_{92}B_8$ 4 nm / Al 1.6 nm + oxidation / $(Co_{90}Fe_{10})_{92}B_8$ 10 nm / Ta 10 nm) was prepared by RF magnetron sputtering at room temperature. The Al_2O_3 tunnel barrier was formed by depositing a layer of metallic Al and oxidizing it using oxygen plasma

produced on an Al_2O_3 target (4 Pa, 200 W, 80 Sec.). The exchange bias field of the pin layer and the magnetic anisotropy of the ferromagnetic free layer were induced by applying a 200 Oe magnetic field during the sputtering. The sensor device was micro-fabricated by performing a serial of photolithography, Ar^+ ion etching and sputtering processes. The structure of DWD TMR sensor was shown as Fig. 3.37. A micro-fabricated 60×20-μm magnetic tunnel junction (MTJ) with a film structure was prepared on the Si substrate. A 200-nm-thick insulation layer (Al_2O_3) and a 250-nm-thick Al conducting wire were micro-fabricated onto the MTJ.

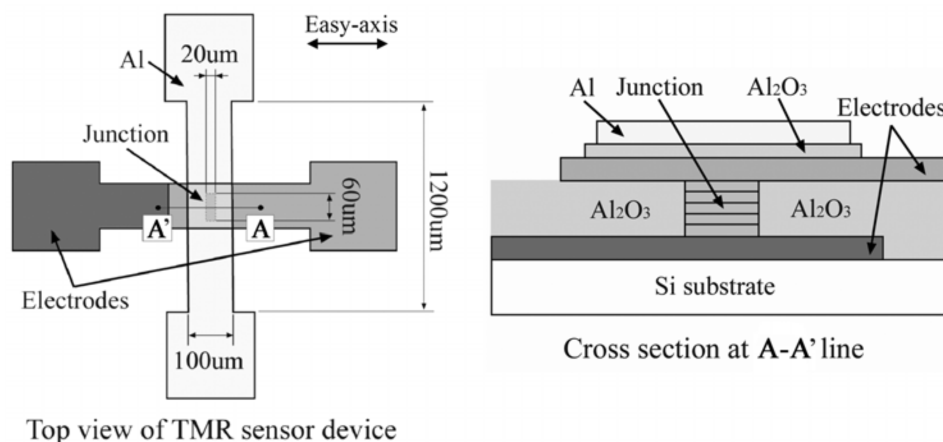

Fig. 3.37. Schematic top view and cross section of the DWD type TMR sensor.

The detailed fabrication process steps are listed as follows:

Step 1: Bottom electrode definition

The photoresist was patterned to cover the bottom electrode lead and contact areas. The film regions uncovered by the photoresist pattern were etched away by ECR Ar^+ ion beam milling and a layer of Al_2O_3 was deposited on the etched regions to flatten the surface (as shown in Fig. 3.38). The resist was strip with a hot remover (MICROPOSIT REMOVER 1165, 60 °C).

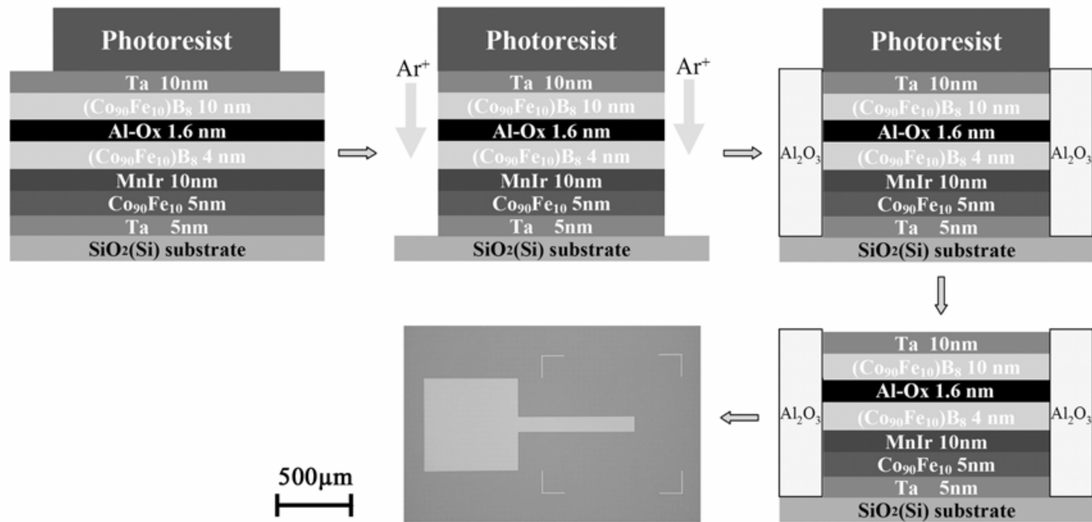

Fig. 3.38. Processes for bottom electrode definition and the optical microscope image of bottom electrode.

Step 2: Junction area definition

The second step is the most crucial and sensitive step in the sensor device fabrication processes. The photoresist was patterned to cover a small junction region on the bottom lead and the 600×600-μm area around the junction was etched by ECR. Since the bottom electrode serves as a contact layer between the contact pad and the junction, the etching must be stopped before the bottom electrode material is completely etched. Typically, the etching was stopped just after the tunnel barrier was removed, which can be detected from the SIMS. After the etching of junction area, an Al_2O_3 insulating layer was deposited to avoid the shortcut between top and bottom electrodes and also forces the current to pass through the barrier perpendicular to the film plane. Normally, 50-nm-thick Al_2O_3 layer was deposited using 5-target sputtering system. After the deposition of Al_2O_3 layer, the photoresist was removed, which opens a via in the insulating layer as a contact hole between the top electrode and junction (as shown in Fig. 3.39).

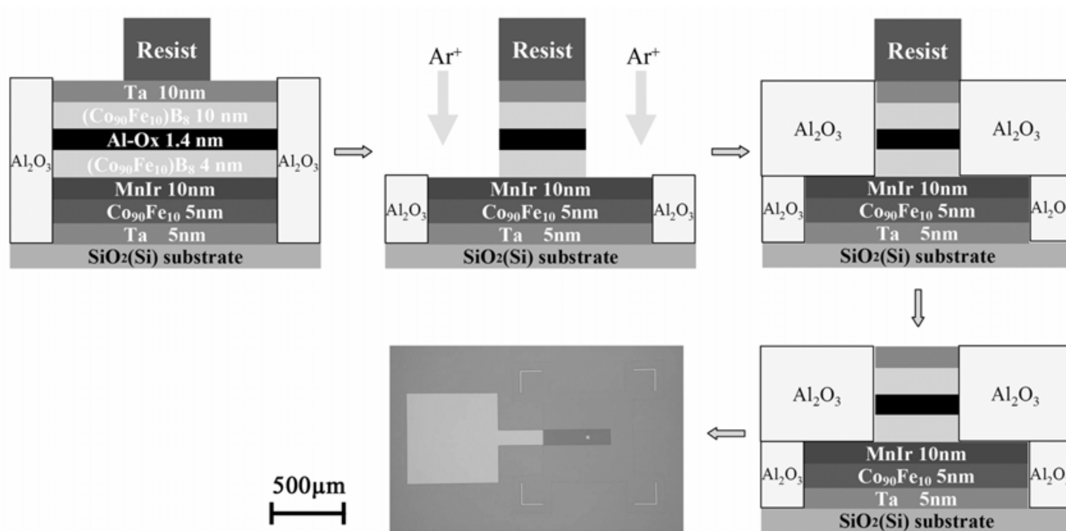

Fig. 3.39. Processes for junction area definition and the optical microscope image after removing the photoresist, the size of MTJ in this figure is 20×20-μm.

Step 3: Deposition of top electrode and Al conducting wire

The photoresist is patterned to cover the sample, except for the top lead and the large contact pad areas. A platinum layer of 60 nm thick was deposited using 5-target sputtering system. The Pt deposited on the resist area was removed with hot photoresist solvent in the ultrasonic bath and the sample was rinsed by IPA for 5 min in ultrasonic bath. In the previous experiment we tried to use aluminum as the material of top electrode, however the metallic Al electrode reacted with the developer and was dissolved during the photolithography process (as shown in Fig. 3.40), and then Pt was used as the material of top electrode instead of Al. After the deposition of top electrode, an insulation layer (Al_2O_3, 200 nm thick) and a 250-nm-thick aluminum conducting wire (100 μm in width and 1200 μm in length) were micro-fabricated onto the MTJ using the same processes. Figure 3.41 illustrates the process steps and the optical microscope images after the processes.

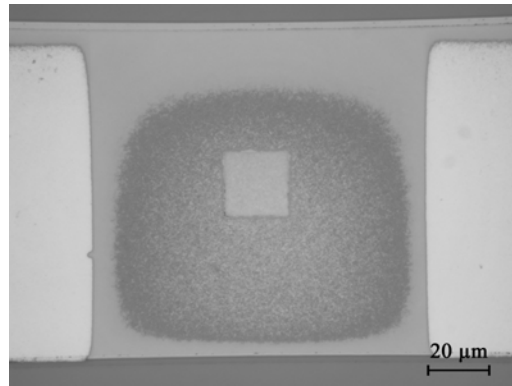

Fig. 3.40. Optical microscope image of the dissolved top electrode, the center is a 20×20-μm magnetic tunnel junction.

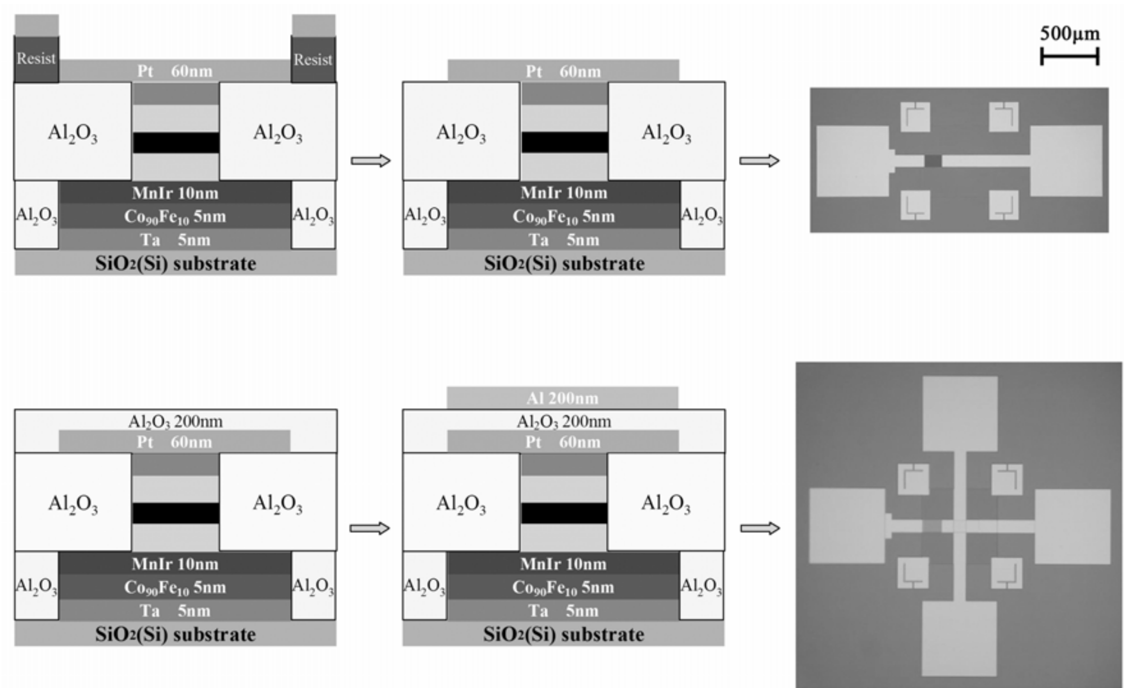

Fig. 3.41. Processes for deposition of top electrode & Al conducting wire and the optical microscope images after the processes.

3.11 Electrical Circuits for DWD Type TMR Sensor

Electrostatic discharge (ESD) is a single-event, rapid transfer of electrostatic charge between two objects, usually resulting when two objects at different potentials come into direct contact with each other. ESD is one of the major causes of device failures in the

semiconductor industry. Since the thickness of insulation barrier for the MTJ is quite thin, the larger electric field is applied to the insulating barrier at a fixed bias voltage. Applied bias voltage of only 1V corresponds to an electric field on the order of $E=1\times10^9$ V/m, which is roughly the dielectric breakdown voltage of insulating oxides. For industrial applications, the operation voltage of MTJ is about a few hundred millivolts and this value is comparable to the breakdown field. Therefore, the dielectric breakdown of MTJ is one of the important considerations for MTJ applications [3].

In this experiment, a pair of diodes was connect in parallel with the MTJ to protect the MTJ from been damaged by the ESD or the voltage spike when voltage source is turned on. Typical silicon diodes exhibit a turn-on voltage of approximately 0.7 volts. Germanium diodes begin to turn-on at about 0.35 volts. Schottky diodes turn on as low as 0.2 volts. Here, three types of diode pair were tested, and figure 3.42 shows the *I-V* loops of the diode-pairs. When the applied voltage is lower than the turn on voltage of the diode, the current transmitted through the diode is negligible small, and if the applied voltage exceeds the turn-on voltage the current increases rapidly.

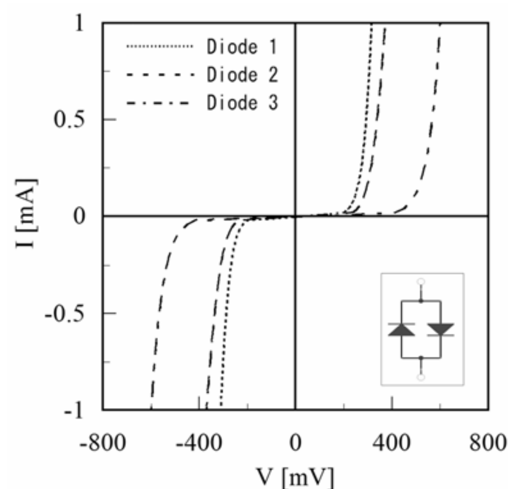

Fig. 3.42. *I-V* loops of the diode-pairs, Diode 1: Schottky diode, Diode 2: Germanium diode, Diode 3: silicon diode.

The signal acquisition circuits for the DWD type TMR sensor are similar to that for the DWD type GMR sensor. The TMR sensor device was connected to a Wheatstone bridge, and a pair of Schottky diodes (with turn on voltage about 0.2 V) was connected in parallel with the MTJ to protect it from the ESD. The applied bias voltage (V_b) on the MTJ was 50mV. Since the bridge output signal contains a 140 kHz component (contributed from the wall oscillatory displacement due to the H_{ac}) and a 1 kHz signal component (contributed from the central position shifting of the oscillatory domain wall due to the H_{ex}), the bridge output was firstly amplified by a low-noise instrumentation amplifier (INA217), which has a bandwidth about 200 kHz at Gain = 60 dB, and then sent to a 4th-order active low-pass filter (MAX274) to selectively separate the 1 kHz signal, as shown in Fig. 3.43.

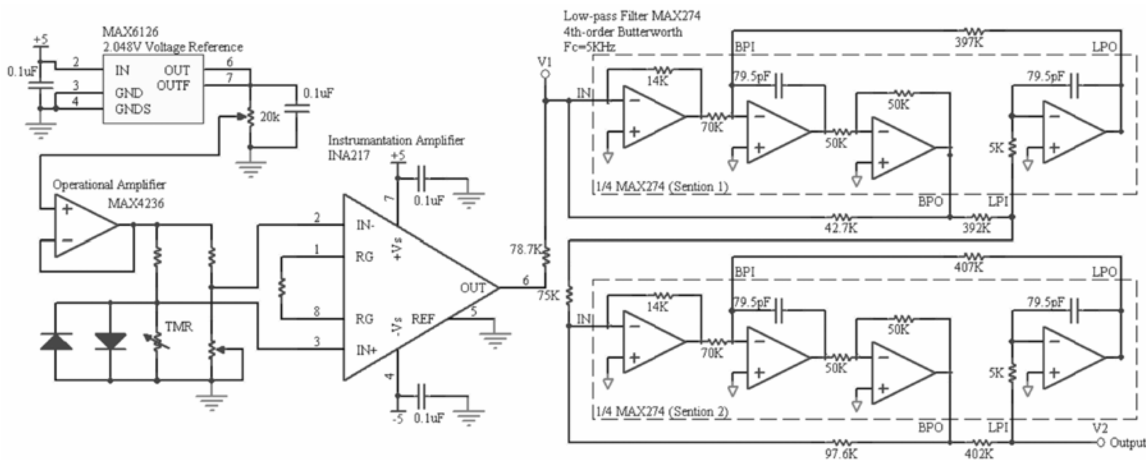

Fig. 3.43. Signal acquisition circuits for the DWD type sensor.

3.12 Field Detection Using DWD type TMR sensor

In this experiment, a 140 kHz AC current (130 mA) was transmitted through the Al conducting wire (C, D) of the DWD TMR sensor to generate an alternating field H_{ac} (about 8.1 Oe) on the free layer. Two independent Helmholtz coils (Coil-1 and Coil-2)

were used to apply a bias field (H_b) and a 1 kHz external field (H_{ex}), respectively; both fields were parallel to the easy axis of sensor device, as shown in Fig. 3.44. The H_{ex} acts as a signal field to be detected, and the H_b was used to cancel the coupling between the pin layer and the free layer which causes the saturation of the domain structure in the free layer at H_b = 0. The applied DC bias voltage on the MTJ (A, B) was 50 mV.

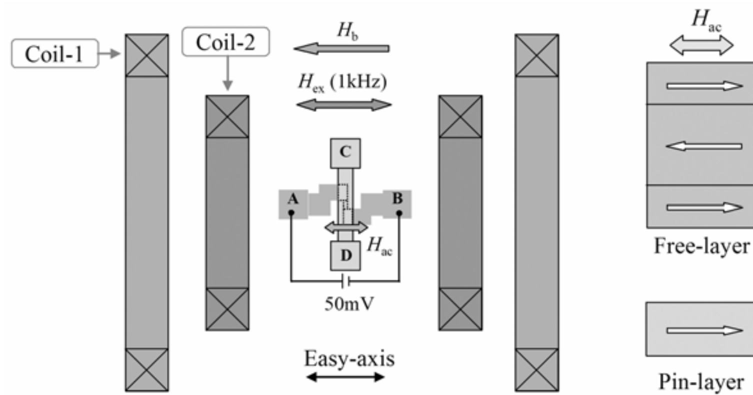

Fig. 3.44. Experimental configuration for DWD type TMR sensor.

Figure 3.45 shows the *M-H* loop and the minor loop for the TMR film stack measured with an AGM. The coercivity of the 10-nm CoFeB free layer is about 12 Oe (estimated from the minor loop shown in Fig. 3.45 (b)).

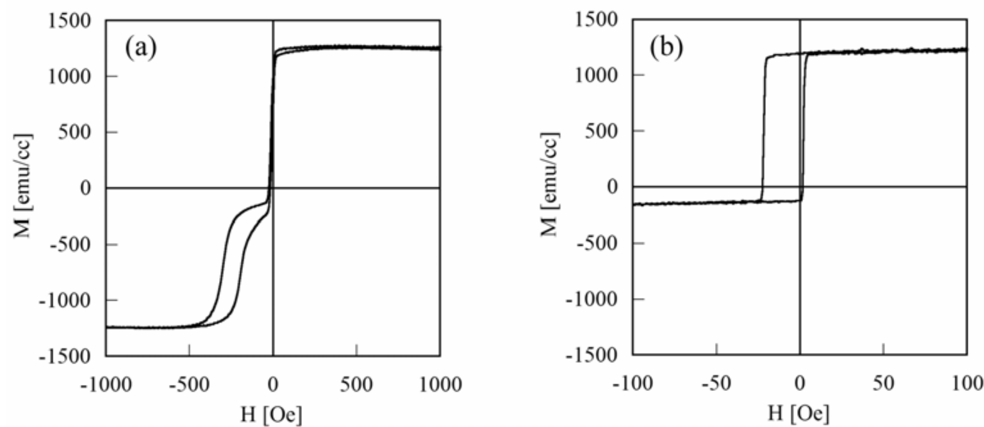

Fig. 3.45. (a) *M-H* loop and (b) minor loop for the TMR film measured with an AGM.

Figure 3.46 shows the MR curves of the MTJ and GMR elements measured under the bias voltage of 10 mV. The TMR ratio and resistance of the MTJ were 12% and 590-Ω, and the GMR element has 5.2% MR ratio and 210-Ω resistance. By comparing minor loops shown in the inset, the free layer of the MTJ has a larger coercivity, which may be attributed to the partial oxidation of the ferromagnetic free layer neighboring the Al-O tunnel barrier, and the horizontal shift of the free layer hysteresis was resulted from the coupling between the pin layer and the free layer. The *I-V* curve of the MTJ was measured by sweeping the bias voltage from a -500 to 500 mV, as shown in Fig. 3.47.

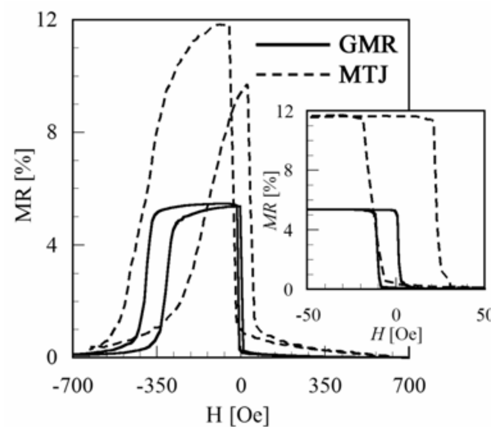

Fig. 3.46. MR curves for the MnIr / CoFeB / Cu / CoFeB GMR element and the MnIr / CoFeB / Al-O / CoFeB MTJ element measured under bias voltage of 10 mV. Inset shows the minor loops of the MTJ and GMR elements.

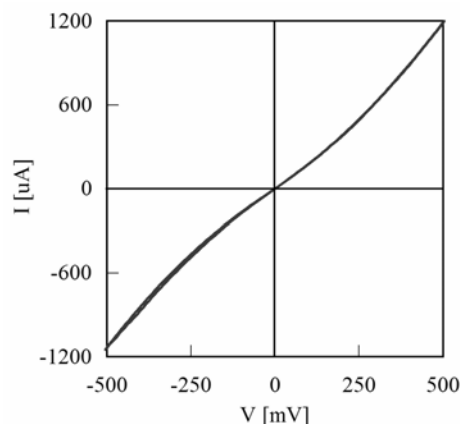

Fig. 3.47. *I-V* curve for the 60×20-μm MTJ.

The GMR and TMR type DWD sensors have different structures and free-layer shapes, thus they exhibit different sensor properties. Figure 3.48 shows the domain structure in the 200×30-μm and 60×20-μm single layer patterns observed with Kerr microscope under different applied fields. In each pattern, there exists only one domain wall and the domain structure was almost rectangle. With increasing the applied field, the domain having the magnetization parallel to the external field was enlarged. For the 200×30-μm pattern (corresponding with the GMR element), the domains were not saturated even under 4.7 Oe applied field, while the domains in the 60×20-μm pattern (corresponding with the MTJ) was almost saturate under the same field.

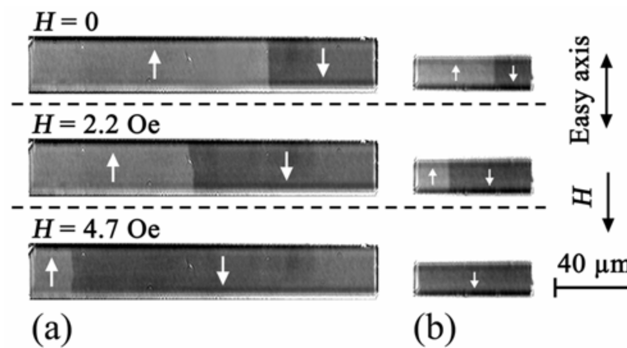

Fig. 3.48. Domain wall structure in the 200×30-μm (a) and 60×20-μm (b) CoFeB single layer patterns observed with Kerr microscope under different applied fields.

The waveforms of instrumentation amplifier (IA) and low-pass filter (LPF) outputs for the DWD GMR sensor were observed with a synchroscope (as shown in figure 3.49), where H_{ac} = 3.1 Oe and H_{ex} = 0.24 Oe. The IA output indicates that the domain wall in the free layer was oscillated by the H_{ac} of 3.1 Oe, and the central position of 140 kHz oscillated domain was shifted by the 1 kHz H_{ex} even it is smaller than the wall coercivity. The RMS value of the 1 kHz LPF output signal, measured by a lock-in amplifier, was defined as V_{out} and the total gain for the 1 kHz signal component was 60 dB.

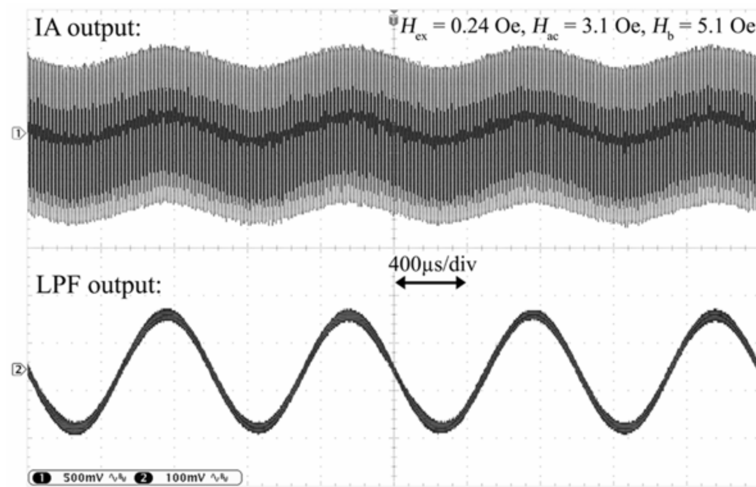

Fig. 3.49. Waveforms of the instrumentation amplifier (IA) output and the low-pass filter (LPF) output for DWD GMR sensor under the conditions of H_{ex} = 0.24 Oe, H_{ac} = 3.1 Oe, H_b = 5.1 Oe. The IA output contains a 140 kHz component and a 1 kHz component, the 1 kHz component is selectively separated by the LPF.

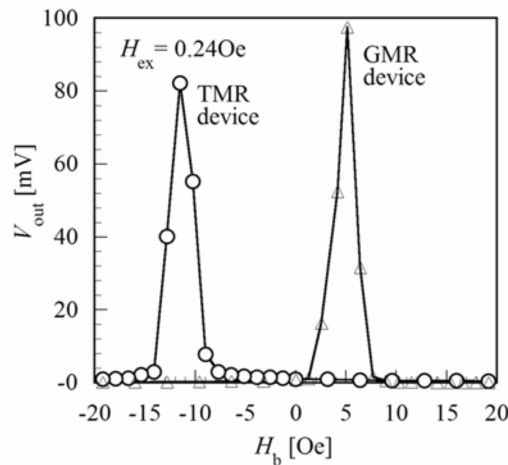

Fig. 3.50. Dependence of the sensor output voltage (V_{out}) on the bias field (H_b) for DWD GMR and TMR sensors.

The dependence of the 1 kHz V_{out} on the bias field (H_b) is illustrated in Fig. 3.50. In the case of the GMR device, magnetization of the pin layer and free layer were initially set antiparallel and H_b swept from negative -20 Oe to positive 20 Oe, while for the TMR device, magnetization of these two layers were initially set parallel and H_b swept from +20 Oe to -20 Oe. Since the GMR and MTJ elements have different free-layer

coercivities and orange-peel coupling fields, the large V_{out} of DWD GMR and TMR sensors appear in different ranges of H_b and take maximum at H_b = 5.1 Oe and H_b = -11.5 Oe, respectively. This result implies that the domain wall can be introduced into the CoFeB free layer within a certain bias field range, and when a proper bias field is applied the shifting of the oscillated domain wall reaches the maximum and the maximum V_{out} can be obtained.

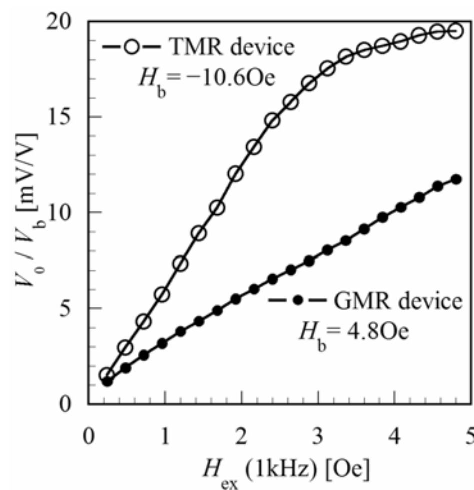

Fig. 3.51. Dependence of the 1 kHz bridge output (V_0) on external field (H_{ex}), the V_0 was normalized by the bias voltage (V_b) applied to the MTJ and GMR elements.

Figure 3.51 shows the dependence of the 1 kHz bridge output (V_0) on external field (H_{ex}). Since the bridge bias voltages for the TMR device and GMR device are different, the V_0 was normalized by the DC bias voltage (V_b) to make the comparison easier. For the DWD TMR sensor, V_0 / V_b becomes saturated when H_{ex} > 2.5 Oe, which indicates that as the H_{ex} increases to 2.5 Oe the shifting of oscillated domain wall in the 20×60-μm free layer reaches the maximum and no longer proportional to the H_{ex}. For the DWD GMR sensor, which has the longer element size (30×200 μm), the V_{out} is linear even H_{ex} increases to 4.8 Oe. This tendency can also be explained by the domain structure in the micro-fabricated CoFeB single layer patterns shown in Fig. 3.48.

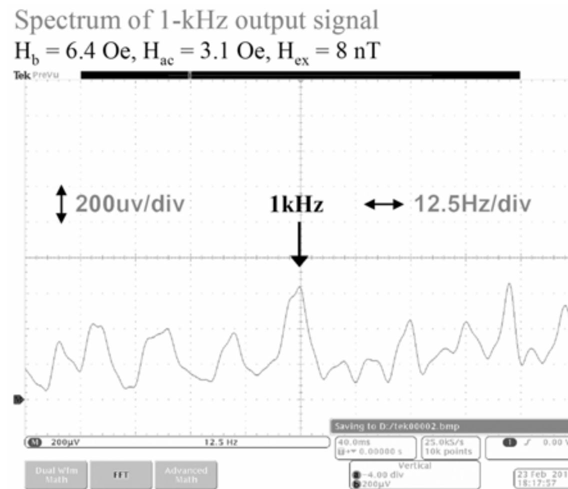

Fig. 3.52. Frequency spectrs (FFT) of the 1 kHz V_{out} under H_{ex} = 8 nT for DWD type GMR sensor.

By calculating the slope of the curves shown in Fig. 3.51, the field sensitivities of the DWD TMR and GMR sensors were 5.81 mV/(V·Oe) and 2.73 mV/(V·Oe), respectively. In comparison with the conventional integrated GMR bridge sensor and the GMR sensor used for magnetic imaging [4, 5], the DWD GMR sensor shows at least 2.7 times higher sensitivity and the minimum 1 kHz signal can be distinguished from the frequency spectra of the LPF output was about 8 nT (as shown in Fig. 3.52).

For the DWD TMR sensor, the sensitivity is limited by the TMR ratio of MTJ, and recently, the MTJ with a TMR ratio of 604% at room temperature was reported [6], which suggests us a way to further improve the sensitivity of DWD TMR sensor. However, since the noise of the DWD TMR sensor is much higher than that for the DWD GMR sensor (as shown in Fig. 3.53), the minimum detectable 1 kHz signal from the background noise for the DWD TMR sensor was 120 nT. The large noise in our MTJ is considered due to the inhomogeneous current flows across the junction [7], and improvement of the junction quality by optimizing the oxidization process [8] may reduce the noise.

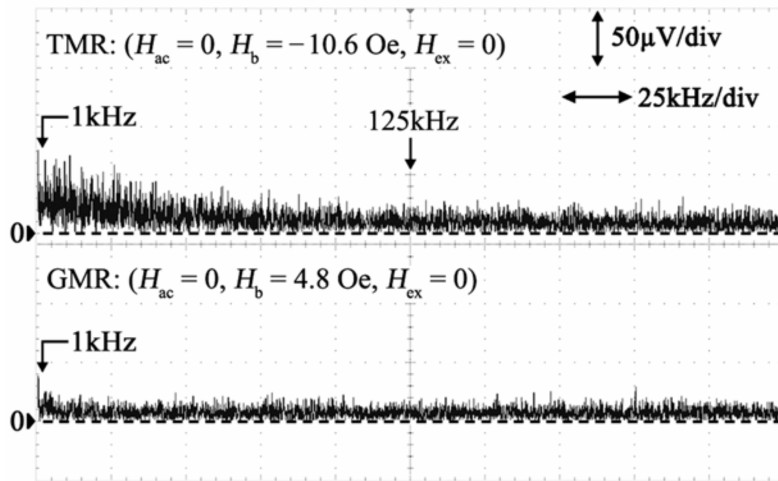

Fig. 3.53. Spectra of the background noise for the DWD TMR and GMR sensors measured under the conditions of H_{ac} = 0 and H_{ex} = 0. The applied bias fields (H_b) for the TMR and GMR sensors were -10.6 Oe and 4.8 Oe, respectively.

3.13 Conclusions

The domain wall displacement in the ferromagnetic free layer was intuitively observed with Kerr microscope under different applied fields. We fabricated the domain wall displacing type sensors using the MTJ and GMR elements, and proved the feasibility of the domain wall displacing method on both TMR and GMR structures. By carrying out the fundamental sensor experiments using the developed sensors, we compared the sensor properties of the TMR and GMR type devices, and a minimum field of 8-nT was detected using the DWD GMR sensor. The field sensitivities of the DWD TMR and GMR sensors were 5.81 mV/(V·Oe) and 2.73 mV/(V·Oe), respectively. The proposed domain wall displacing type sensors exhibited higher sensitivity compared to the conventional magnetization rotation type sensors, and further improvement of the sensitivity is expected.

As the property of the DWD type sensor is determined by the domain structure in the soft magnetic free layer. Domain structures in various soft magnetic single layer

patterns (30 × 200 μm) have been investigated and two typical free-layer materials were selected to fabricate the sensor devices: 10 nm CoFeB, which has a rectangle domain structure, and 10 nm NiFe, which has a closure domain structure. The sensor with a 10 nm NiFe free layer showed a higher field sensitivity (about 4.2 mV/(V·Oe)) but the sensor output became saturated when external field (H_{ex}) > 0.4 Oe. For the sensor, which has a 10 nm $(Co_{90}Fe_{10})_{92}B_8$ free layer, the sensor output was linear even H_{ex} was increased to 2.6 Oe. In addition, the sensors were operated under conventional magnetization rotation mode to compare the sensor outputs with the DWD mode. When the sensors operated under the DWD mode, at least 2 times higher field sensitivity was achieved. Although the field resolution of proposed DWD sensor is still lower than the GMI sensor, as the sensitivity of the DWD type TMR sensor is only limited by the TMR ratio of the MTJ, much higher sensitivity is expected by using the reported MTJ with a TMR ratio of 604% at room temperature. Moreover, the size of proposed DWD type sensor can be made smaller than the GMI sensor and it is easy to be integrated into one chip. Table 3.1 compares the dynamic range, sensitivity, noise and signal to noise ratio (SNR) of the proposed DWD type sensors.

References

[1] Texas Instruments, INA217 Data sheet, (2005).

[2] N. Qureshi and H. Schmidt, Appl. Phys. Lett. 85, 431 (2004).

[3] D. Kim, T. Kim, S. Kim, J. H. Kong, Y. Yu and K. Char, Jpn. J. Appl. Phys. 42, 1242 (2003).

[4] W. Ku, F. Silva, J. Bernardo and P. P. Freitas, J. Appl. Phys. 87, 5353 (2000).

[5] C. H. Smith, R. W. Schneider and A. V. Pohm, J. Appl. Phys. 93, 6864 (2003).

[6] S. Ikeda, J. Hayakawa, Y. Ashizawa, Y. M. Lee, K. Miura, H. Hasegawa, M. Tsunoda, F. Matsukura and H. Ohno, Appl. Phys. Lett. 93, 082508 (2008).

[7] E. R. Nowak, R. D. Merithew, M. B. B. I. Weissman and S. S. P. Parkin, J. Appl. Phys. 84, 6195 (1998).

[8] P. W. T. Pong, M. Schmoueli and J. W. F. Egelhoff, IEEE Trans. Magn. 44, 2911 (2008).

Chapter 4

Magnetization Modulation Type Field Sensor

The typical magneto-resistive (MR) sensors, including the DWD sensor introduced in chapter 3, sense the external field by measuring the magneto-resistance (MR) change of the MR elements, and for this type of sensors, the temperature compensation is necessary to reduce the output drift caused by the change of environmental temperature. To solve this problem, we proposed a field sensor, which senses the external field by detecting the change of frequency component in the modulated GMR output.

4.1 Principle of Magnetization Modulation Method

The magnetization modulation type sensor modulates the free-layer magnetization direction in the GMR device using an alternating magnetic field, a DC bias field H_b was applied to align the magnetization of the free layer along the easy-axis, and an AC field H_{ac} was used to modulate the magnetization direction of the free layer about the pinned direction. The oscillation of free-layer magnetization about the pinned direction causes the increase of GMR resistance under both positive and negative values of H_{ac}. Thus the H_{ac} (f) may generate a $2f$ (harmonic) signal in the GMR output. Figure 4.1 (a) shows the waveforms of the H_{ac} and the voltage on the GMR element under zero H_{ex}. The free-layer magnetization can be tilted by applying an external field H_{ex} in hard-axis direction, and the $2f$ component will be decreased (as shown in Fig. 4.1 (b)).

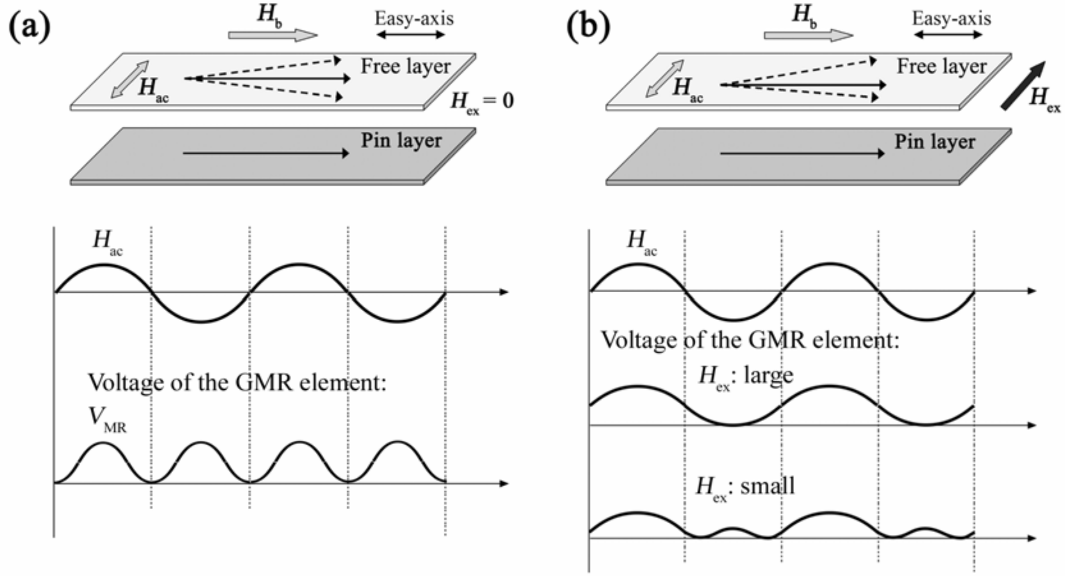

Fig. 4.1. Cartoon of the modulation of the free-layer magnetization in the GMR element by applying an AC field H_{ac}, and the voltages of the GMR element under (a) zero external field (H_{ex}) and (b) $H_{ex} \neq 0$.

Suppose the resistance of the GMR element is R (free layer // pin layer) and $R+\Delta$ (free layer $\perp$ pin layer), when an AC field $H_{ac}\sin(2\pi ft)$ and a DC field H_{ex} are both applied along the hard-axis the resistance of the GMR element can be written

$$R' = R + \Delta R\{1 - \cos(\delta + \theta_0 \sin(2\pi ft))\}$$

$$\approx R + \Delta R\left\{\frac{\delta^2}{2} + \frac{\theta_0^2}{2}\cdot\frac{1-\cos(4\pi ft)}{2} + \delta\theta_0\sin(2\pi ft)\right\} \tag{4.1}$$

where the δ is the angle of magnetization between the free layer and the pin layer due to the H_{ex}, and θ_0($\approx H_{ac}/H_k$) is the amplitude of angle modulation due to the H_{ac}, f is the frequency of H_{ac}. The GMR element was connected to a Wheatstone bridge, and the bridge output voltage is given by

$$V_{bridge} \approx \frac{V_b \cdot MR}{4}\left\{\frac{1}{2}\cdot\left(\frac{H_{ex}}{H_k}\right)^2 + \frac{1}{2}\cdot\left(\frac{H_{ac}}{H_k}\right)^2\cdot\frac{1-\cos(4\pi ft)}{2} + \frac{H_{ex}\cdot H_{ac}}{H_k^2}\cdot\sin(2\pi ft)\right\} \tag{4.2}$$

where V_b is the bridge bias voltage, MR is the magnetoresistance ratio of the GMR ($\Delta R/R$), H_k is the uniaxial anisotropy field (~30 Oe) of the 10-nm CoFeB free layer. When H_{ex} = 0, only the 2nd term remains, and thus the V_{bridge} contains only the $2f$ component (as shown in Fig. 4.1 (a)). When a H_{ex} (DC) is applied along the hard axis, the oscillating center will be tilted from the pinned direction, which causes the increase of f component and the decrease of $2f$ component (as shown in Fig. 4.1 (b)). This is due to the increase of the 3rd term in equation (4.2), when H_{ex} and H_{ac} are applied simultaneously.

4.2 Sensor Device

The modulation type sensor has the similar structure as the DWD sensors, where A 200-nm-thick insulation layer (Al_2O_3) and a 250-nm-thick Al conducting wire were micro-fabricated onto the GMR element, but the easy axis of the free layer is set parallel to Al conducting wire (as shown in Fig. 4.2). The resistance of the micro-fabricated Al conducting wire (100 μm in width, 1200 μm in length) was about 3.8 Ω. By transmitting an alternating current through the Al conducting wire, an AC field (H_{ac}) can be produced on the GMR element, and the H_{ac} can be calculated using equation (3.2).

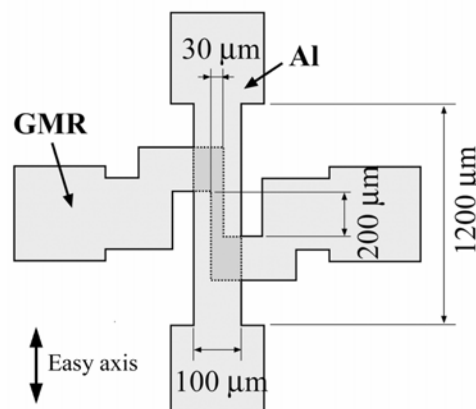

Fig. 4.2. Schematic top view of the magnetization modulation type GMR device.

The sensor device composed of GMR multilayer film, Si wafer / Ta 5 nm / $(Co_{90}Fe_{10})_{92}B_8$ 10 nm / Cu 2.2 nm / $Co_{90}Fe_{10}$ 3 nm / $Mn_{80}Ir_{20}$ 10 nm / Ta 2 nm, was prepared on a thermally oxidized silicon wafer (SiO_2 500 nm) by RF magnetron sputtering at room temperature. The exchange bias field of the CoFe 3 nm / MnIr 10 nm pin layer and the uniaxial anisotropy of the 10-nm CoFeB free layer were induced by applying a 200 Oe magnetic field during the sputtering. The spin-valve GMR element (200 μm in length, 30 μm in width) was micro-fabricated using photolithography and Ar^+ ion etching techniques. The resistance and MR ratio of the micro-fabricated GMR element were 163 Ω and 5.8 %, respectively. Figure 4.3 shows the easy-axis and hard-axis MR curves of the micro-fabricated GMR element. During the measurement, the bias voltages applied to the GMR element was 1 V. The uniaxial field of the free layer is about 30 Oe, and the coercivity of the 10-nm CoFeB free layer is about 2 Oe. In this experiment, only the magnetization rotation of free layer about the easy axis was utilized.

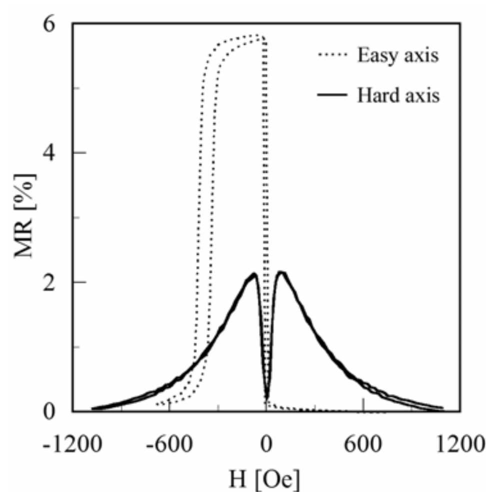

Fig. 4.3. Easy-axis and hard-axis MR loops of the micro-fabricated GMR element.

4.3 Experimental configuration

The GMR element was connected to a Wheatstone bridge, where the applied bridge bias voltage was 2.0 V, as illustrated in Fig. 4.4. Two independent Helmholtz coils (not shown in the figure) were used to apply an external field (H_{ex}) and a bias field (H_b). The H_{ex} applied along the hard axis acts as a magnetic field to be detected. The free-layer magnetization of the GMR element was saturated along the easy axis by the DC bias field H_b (5.9 Oe) applied parallel to the pin-layer magnetization direction. The 5 kHz current (37 mA), transmitted through the Al conducting wire, produced an AC field H_{ac} (about 2.3 Oe) along the hard axis to oscillate the free-layer magnetization

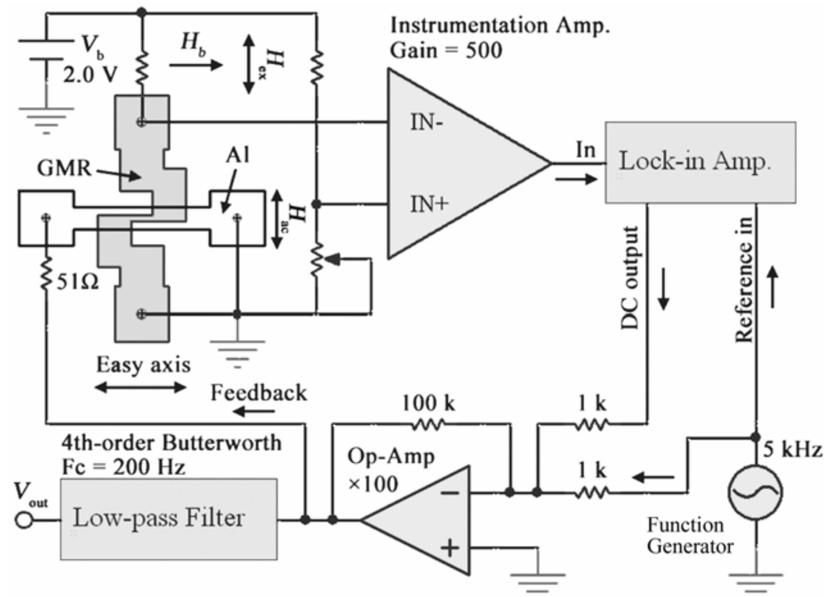

Fig. 4.4. Experimental configuration and signal acquisition circuit. Two independent Helmholtz coils (not shown in the figure) are used to apply the bias field (H_b) and the external field (H_{ex}).

The bridge output was amplified by a low-noise instrumentation amplifier (IA; INA217) with a gain of 54 dB, and the 5 kHz component in the IA output was detected

by a lock-in amplifier (LA). The time constant of the LA was set at 100 msec and the gain for 5 kHz signal was about 40 dB. The LA output (DC) was mixed with a 5 kHz signal and sent to the Al conducting wire. The DC current generated a feedback field H_f on the GMR element. The DC voltage applied to the Al conducting wire and the 51-Ω resistor was separated using a 4th-order active low-pass filter (LPF; f_c = 200 Hz) and was defined as V_{out}. Figure 4.5 shows the schematic of the 4th-order low-pass filter with a cut-off frequency (f_c) of 200 Hz, two 2nd-order sections are used to build this filter.

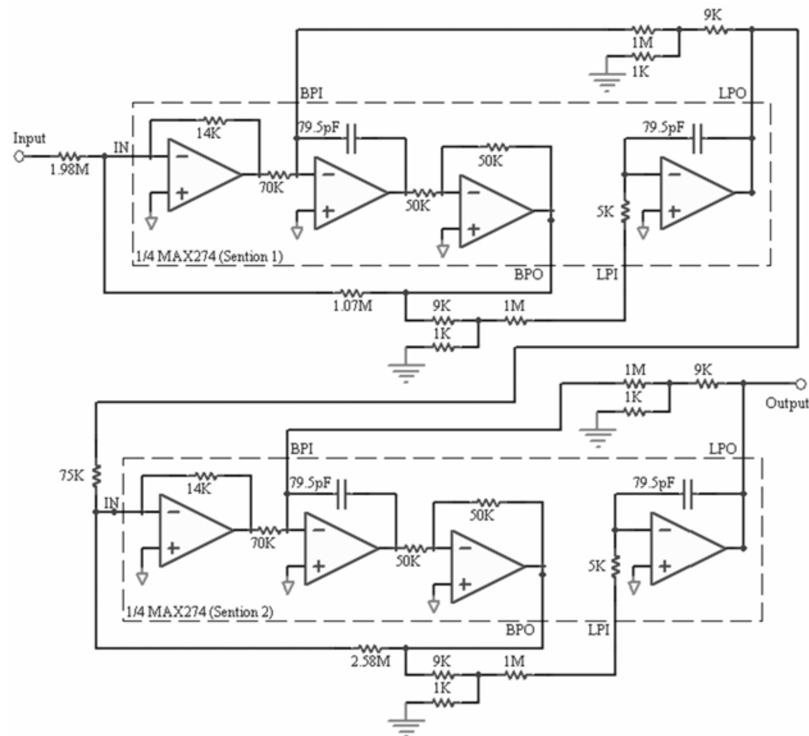

Fig. 4.5. Schematic of the 4th-order low-pass filter with a cut-off frequency (f_c) of 200 Hz.

The frequency response for this low-pass filter is illustrated in Fig. 4.6, where a function generator was used to produce a sine test signal (1-100 kHz, 1V RMS), and the root mean square (RMS) value of the output voltage was measured with an oscilloscope.

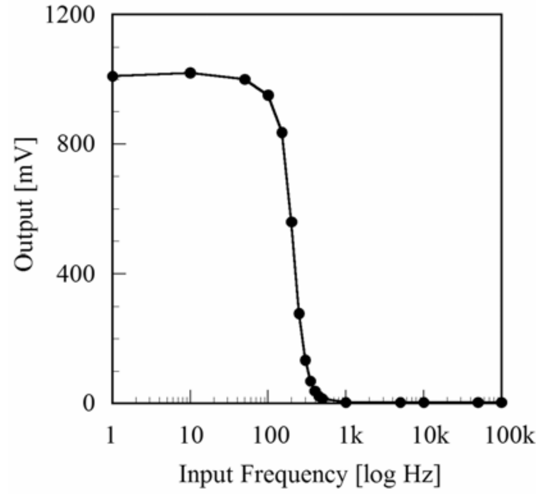

Fig. 4.6. Frequency response of the 4th-order low-pass filter (f_c = 200 Hz).

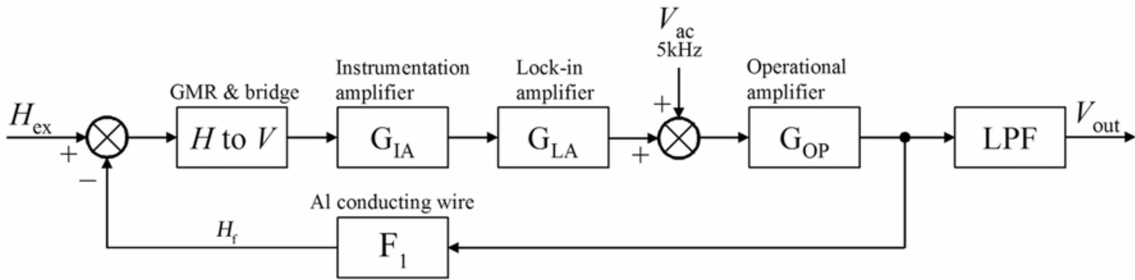

Fig. 4.7. Block diagram of the GMR sensor with negative feedback.

Figure 4.7 shows the block diagram of the GMR sensor with negative feedback. The GMR element and bridge convert the field to voltage, and the Al conducting wire acts as a voltage to field converter. In the closed-loop mode, the LA output (DC) is amplified and transmitted through the Al conducting wire to generate a DC field on the GMR element, which cancels the tilt of the oscillated free-layer magnetization center and acts as a negative feedback to the system. If the gain of feedback current is sufficient, the feedback current will be proportional to the H_{ex}. The close-loop sensor output can be written

$$V_{out} = \frac{H_{ex}}{F_1} \cdot (1 + \frac{4}{MR} \cdot \frac{H_k^2}{F_1 \cdot V_b \cdot H_{ac}} \cdot \frac{1}{G_{LA} \cdot G_{IA} \cdot G_{OP}})^{-1} \tag{4.3}$$

where F_1 (~1.14 Oe/V) is the conversion factor of V to H for the Al conducting wire, MR is the magnetoresistance ratio of the GMR, H_k is the uniaxial anisotropy field of the CoFeB free layer, G_{LA}, G_{IA} and G_{OP} are the gains of lock-in amplifier, instrumentation amplifier and operational amplifier, respectively. Since $G_{LA} \cdot G_{IA} \cdot G_{OP} \approx 5 \times 10^6$, $4/MR \approx 70$, $H_k^2/(F_1 \cdot V_b \cdot H_{ac}) \approx 200$, equation (4.3) can be simplified to

$$V_{out} \approx \frac{H_{ex}}{F_1} \tag{4.4}$$

which indicates that the V_{out} has almost no dependence on V_b, MR and the gains of the amplifiers.

4.4 Experimental Results and Discussion

Figure 4.8 (a) shows the waveforms of the 5 kHz H_{ac} and the IA output under zero H_{ex}. The waveforms shown in Fig. 4.8 were measured in an open-loop mode, where the lock-in amplifier was disconnected. Since the oscillation of free-layer magnetization about the pinned direction causes the increase of GMR resistance under both positive and negative values of H_{ac}, the 5 kHz H_{ac} generates a 10 kHz (harmonic) signal in the GMR output. As shown in Fig. 4.8 (a), when the H_{ac} swept from positive to zero, the IA output voltage was lower than it swept from negative to zero, and this level difference increased with increasing the frequency or intensity of the H_{ac}. This result can be understood by the rotational hysteresis of the pin-layer magnetization and the misalignment of the photomasks during the micro-fabrication process, where the length direction of the GMR element is slightly tilted from the easy axis of the deposited GMR film. However, the effects of asymmetry and hysteresis can be eliminated by adjusting the detecting phase of the LA as described later. When a H_{ex} (DC) is applied along the hard axis, the oscillating

center will be tilted from the pinned direction, which causes the increase of 5 kHz component in the IA output (as shown in Fig. 4.8 (b)). This is due to the increase of the 3rd term in equation (4.2), when H_{ex} and H_{ac} are applied simultaneously.

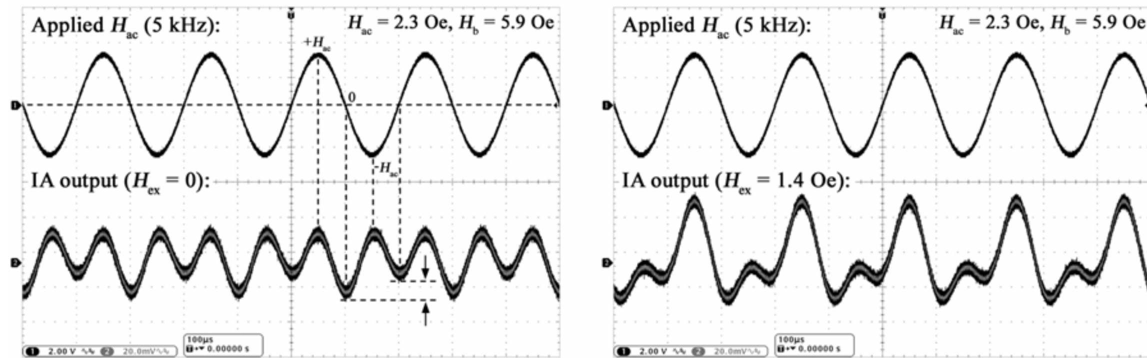

Fig. 4.8. Waveforms of the instrumentation amplifier output under (a) zero external field (H_{ex}) and (b) H_{ex} = 1.4 Oe. The waveforms were measured in an open-loop mode.

The dependence of the LPF output V_{out} on the external applied DC field H_{ex} is illustrated in Fig. 4.9. The V_{out} is proportional to the external applied field in the range from -1.5 Oe to +1.5 Oe and deviates from the proportional relationship when further increase of the H_{ex}. The nonlinear response of V_{out} under large H_{ex} is due to the limitation of the op-amp output. In this experiment, the output voltage swing of the op-amp is ± 3.4 V and the maximum current can be applied to the Al conducting wire is about ± 62 mA, where 37 mA was allocated for generating the H_{ac}, and the rest of 25 mA can be used as the feedback DC current, which generates a 1.6 Oe feedback field on the GMR element. The field detection range can be modified by changing the amplitude of H_{ac} or by replacing the resistor connected in serial with the Al conducting wire. However, special attention should be paid to the maximum current that can be transmitted through the Al conducting wire. The inset of Fig. 4.9 shows the V_{out} versus small external field H_{ex}, the

error bar for each measured point was estimated from the deviation of LPF output during 30-second measurement and the mean values were plotted as dots. As shown in the inset, the offset of the V_{out} at H_{ex} = 0 is quite small, which means that the effect of the unwanted 5 kHz component at H_{ex} = 0 (shown in Fig. 4.8 (a)) can be completely eliminated by adjusting the detecting phase of the LA.

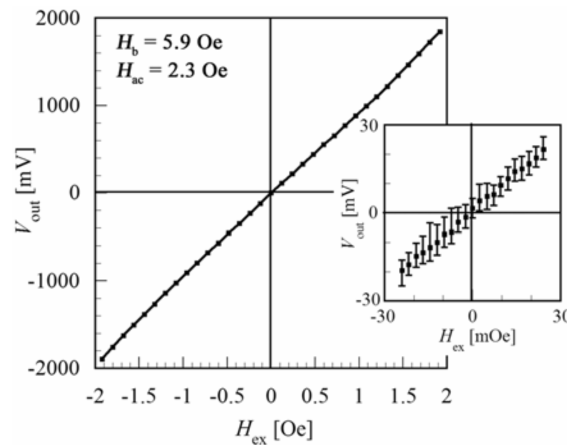

Fig. 4.9. Dependence of the low-pass filter output (V_{out}) on the external field (H_{ex}). Inset shows the V_{out} versus small external field H_{ex}, the error bar for each measured point was estimated from the deviation of the LPF output during 30-second measurement and the mean values were plotted as dots.

The magnetization rotation type GMR sensor device, which has the same structure as the DWD type sensor introduced in chapter 3, was used to compare the field resolution and temperature drift. A 40 Oe bias field H_{b0} was applied to saturate the free-layer magnetization orthogonal to the easy axis and the magnetization of the free layer was rotated by the external field (H_{ex}) applied along the easy axis. The output signal of the IA (Gain = 54 dB) was detected with a synchroscope. Before starting the measurement, the IA output (V_{out}) was adjusted near zero by balancing the Wheatstone bridge. All the measurements were carried out in a simple shield box made of 3-mm-thick iron plates and a tape heater was used to raise the inside temperature.

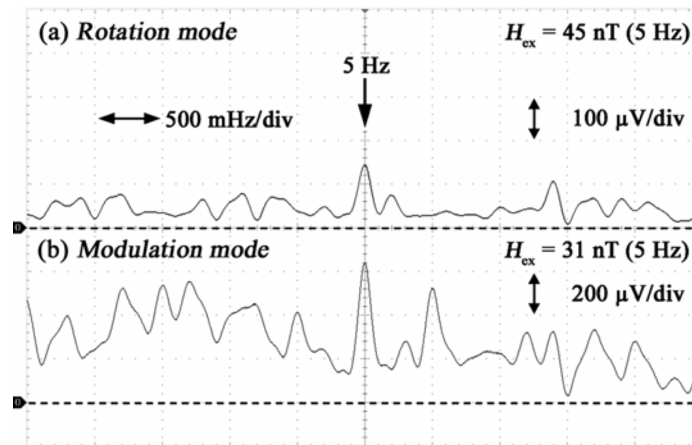

Fig. 4.10. Frequency spectra of the sensor outputs for (a) magnetization rotation mode and (b) magnetization modulation mode. The spectra was obtained by applying the 5 Hz external fields.

Figure 4.10 shows the frequency spectra of the sensor outputs for (a) magnetization rotation mode and (b) magnetization modulation mode, where the 5 Hz external fields were applied to obtain the spectra. The frequency of this signal was set at a lower value (5 Hz) since the time constant of the LA was set at 100 msec. The minimum detectable field for the modulation mode was about 0.3 mOe (30 nT), which is slightly smaller than that for the rotation mode (45 nT). The limitation of resolution for the proposed sensor is considered to be due to the high noise level. As shown in the Fig. 4.10, the average level of the background noise for the modulation mode was about 300 μV (corresponds to 0.3 mOe), which is higher than that for the magnetization rotation mode (about 0.15 mOe in terms of the field intensity). Since the input noise of the IA (INA217) is quite low (1.3 nV/Hz$^{0.5}$ at 1 kHz), the noise of the modulation type sensor is mainly due to the large dimension of the circuit, which may pick up more external noise to the system. The noise level is expected to be further reduced by using an integrated LA module with much smaller size and shorten the connecting cables between the components.

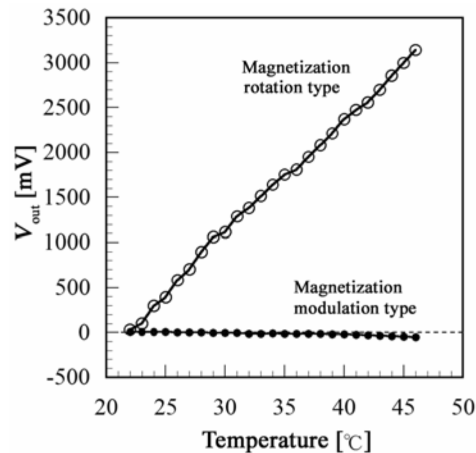

Fig. 4.11. Dependence of the sensor outputs (V_{out}) on environmental temperature for the typical magnetization rotation type sensor and modulation type sensor under zero external fields.

For the typical magnetization rotation type sensor, the change of environmental temperature may cause the resistance drift of the bridge resistors, which will cause a significant drift in the sensor output. On the contrary, the modulation type sensor detects the frequency change of the GMR output, and the output will not be affected by the environmental temperature as described in section 4.3. Figure 4.11 shows the dependence of the sensor outputs (V_{out}) on environmental temperature for the typical magnetization rotation type sensor and modulation type sensor under zero external fields. With increasing the temperature from 22 to 46 °C, the drift of V_{out} for the modulation type sensor was about 60 mV, which is 50 times lower than that for the typical magnetization rotation type sensor. The calculated temperature drift for the bridge output is about 0.26 mV/°C, which is due to the different temperature characteristics for the bridge resistors and the GMR element.

4.5 Conclusions

The fundamental properties of the proposed modulation type GMR field sensor have been investigated. When the sensor worked in a close-loop mode and the free-layer magnetization was modulated by the H_{ac} (2.3 Oe), the sensor output (V_{out}) was proportional to the applied external field (H_{ex}) in the range from -1.5 Oe to +1.5 Oe. The V_{out} is only determined by the feedback current, and has no direct relationship with the MR ratio or the gains of the amplifiers. The modulation type sensor exhibits much lower temperature drift (about 1/50) compared to the typical magnetization rotation type sensor and further reduction of the drift can be achieved by improving the signal acquisition circuit. Therefore, we can conclude that the modulation type GMR sensor proposed here is drift free and can be used for high precision DC field detection without the additional temperature compensation.

Chapter 5

General Conclusions

This study focused on the development of high sensitivity micro-magnetic sensors using magneto-resistance devices. This thesis presented two types of magnetic field sensors: 1) Domain wall displacing (DWD) type sensor, which utilizes the oscillatory domain wall displacement in the ferromagnetic free layer to detect the external field, and 2) Magnetization modulation type sensor, which senses the external field by detecting the change of frequency component in the modulated GMR output.

In chapter 1, the principles and applications of various magnetic field sensors have been shortly introduced. The magneto-resistive effects, including anisotropic magneto-resistive effect, giant magneto-resistance effect and tunnel magneto-resistance effect, have been briefly described. As the main MR elements used in this study, the spin-valve GMR and the magnetic tunnel junction have been discussed in detail.

The preparation of sensor devices and the analytical tools were introduced in chapter 2. The lithographic photomasks were prepared using electron beam lithography (EBL) technique. The multi-layer films were prepared on thermally oxidized silicon wafers (SiO_2 500 nm) by RF magnetron sputtering at room temperature. An alternating gradient-field magnetometer (AGM), which has a sensitivity exceeding (10^{-8} emu), was used to measure the magnetic moments of the magnetic thin films. The sensor devices and the samples prepared for Kerr microscope observation were micro-fabricated using

photolithography and Ar^+ ion etching techniques. The sectional structure of the TMR film was observed using a transmission electron microscope (TEM) and the domain structures in the magnetic films were observed by Kerr microscopy.

In chapter 3, domain structures in various magnetic patterns have been investigated. The operational principle, fabrication and signal acquisition circuit of the proposed domain wall displacing (DWD) type field sensor were described in detail. By carrying out the fundamental sensor experiments using the developed sensors, we compared the sensor properties of the TMR and GMR type devices, and a minimum field of 8-nT was detected using the DWD GMR sensor. The field sensitivities of the DWD TMR and GMR sensors were 5.81 mV/(V·Oe) and 2.73 mV/(V·Oe), respectively. The proposed domain wall displacing type sensors exhibited higher sensitivity compared to the conventional magnetization rotation type sensors, and further improvement of the sensitivity is expected. In addition, the influence of free-layer domain structure on the sensor output has been investigated. The sensor with a 10 nm NiFe free layer exhibited a higher field sensitivity (about 4.2 mV/(V·Oe)) but the sensor output became saturated when external field (H_{ex}) > 0.4 Oe. For the sensor, which has a 10 nm $(Co_{90}Fe_{10})_{92}B_8$ free layer, the sensor output was linear even H_{ex} was increased to 2.6 Oe.

In order to improve the DC drift in the DWD sensor output, which caused by the change of environmental temperature, a magnetization modulation type GMR sensor was proposed. The details of this sensor were illustrated in chapter 4. The proposed field sensor modulates the free-layer magnetization direction in the GMR device using an alternating magnetic field, and a negative feedback mechanism was utilized to obtain the linear sensor output and to eliminate the DC drift caused by the change of environmental temperature. When the sensor worked in a close-loop mode and the free-layer

magnetization was modulated by the H_{ac} (2.3 Oe), the sensor output (V_{out}) was proportional to the applied external field (H_{ex}) in the range from -1.5 Oe to +1.5 Oe. The V_{out} is only determined by the feedback current, and has no direct relationship with the MR ratio or the gains of the amplifiers. The modulation type sensor exhibits much lower temperature drift (about 1/50) compared to the typical magnetization rotation type sensor and further reduction of the drift can be achieved by improving the signal acquisition circuit. Therefore, the modulation type GMR sensor proposed here considered to be drift free and can be used for high precision DC field detection without the additional temperature compensation. The proposed two types of magnetic field sensors in this research are expected to be used in the applications of biological detection, magnetic compass, position sensing, etc.

Acknowledgements

Pursuing a Ph.D. is a both painful and enjoyable experience. It is just like climbing a high peak, step by step, accompanied with bitterness, hardships, frustration, encouragement and with so many people's kind help. When I found myself at the top enjoying the beautiful scenery, I realized that it was, in fact, teamwork that got me there. Though it will not be enough to express my gratitude in words to all those people who helped me, I would still like to give my many thanks to all these people.

First of all, I would like to express my deep and sincere gratitude to my honorific supervisor, Prof. Satoshi Iwata, who accepted me as his first Ph.D. student without any hesitation when I presented him my research proposal. During the 3 years study in his laboratory I learned not only the knowledge but also a kind of responsibility and diligence from him. Without his patiently supervising and help, I could not have finished my dissertation successfully. I would like to extend my sincere appreciation to Prof. Akira Fujimaki and Prof. Hiroyuki Awano for their valuable suggestions and encouragement. Special thanks are also given to Dr. Takeshi Kato (Associate Professor), who offered me so many advices, and always patiently guiding me in the right direction. He helped me to correct mistakes in my all published papers, and suggested possible improvements. It is not sufficient to express my gratitude with only a few words. I would like to express my appreciation to all those persons who have offered me their kind help during my research, including Dr. Suharuyadi Edi, Mr. Susumu Okuda, Mr. Tomohiro Kozawa, Mr. Keiji Masuda, Mr. Daiki Oshima and Mr. Kumazawa Masayuki.

My sincere thanks go to the Chinese Scholarship Committee, which provided me with financial support during the Ph.D. study. Without its support and financial help, it

would not have been possible for me to pursue and to complete this Ph.D. project successfully. I would like to convey my heartfelt thanks to my home university, Northeastern University, and Hohai University for offering me an ideal environment in which I felt free and could concentrate on my research. There are so many friends, both in China and in abroad, who offered me so much kindly help. I give my sincere thanks to all these people.

I am very grateful for my parents. Their understanding and love encouraged me to work hard and to continue pursuing a Ph.D. abroad. Their firm and kind-hearted personality has affected me to be steadfast and never bend to difficulty. They always let me know that they are proud of me, which motivates me to work harder and do my best. Even when they were ill, both of them would not let me know so as to enable me to concentrate on my research. I owe my every achievement to both of them.

Last but not least, I am greatly indebted to my devoted wife Xiaoqiao and my son Zixu. They form the backbone and origin of my happiness. Being both a mother and father while I was away was not an easy thing for my wife. She took every responsibility and suffered all the bitterness to take care of my son and my family. Her love and support without any complaint or regret has enabled me to complete this Ph.D. project.

List of Achievements

I. Papers

Title	Journal	Authors
① High sensitivity GMR magnetic sensor using oscillatory domain wall displacement.	Journal of Applied Physics, vol. 107, pp. 09E709-1-3 (2010).	G. A. Wang S. Nakashima S. Arai T. Kato S. Iwata
② Design and performance of domain wall displacing-type field sensors using a magnetic tunnel junction and a giant magnetoresistive device.	Journal of Physics D: Applied Physics, vol. 43, pp. 455001-1-5 (2010).	G A Wang Y Masuda T Kato S Iwata
③ Influence of the free-layer domain structure on domain-wall displacing type field sensors.	Journal of Applied Physics, vol. 109, pp. 07E523-1-3 (2011).	G. A. Wang Y. Masuda T. Kato S. Iwata
④ Low drift giant magnetoresistive field sensor using modulation of free-layer magnetization direction.	Journal of Physics D: Applied Physics, vol. 44, pp. 235003-1-5 (2011).	G A Wang S Arai T Kato S Iwata

II. International Conferences

Title	Conference	Authors
1. High sensitivity GMR magnetic sensor using oscillatory domain wall displacement.	The 11th Joint MMM-Intermag Conference 2010, AG-05, Washington DC, USA, January 2010.	G. A. Wang S. Nakashima S. Arai T. Kato S. Iwata
2. Nanotesla field detection using domain-wall displacing type GMR sensor.	The 2nd International Symposium on Advanced Magnetic Materials and Applications, RE-13, Sendai, Japan, July 2010.	G. A. Wang S. Nakashima S. Arai T. Kato S. Iwata

3. Study of the Domain Structure in Domain-wall Displacing type Field Sensor.	The 55th Annual Conference on Magnetism and Magnetic Materials, FQ-04, Atlanta, USA, November 2010.	G. A. Wang Y. Masuda T. Kato S. Iwata
4. Low drift DC field sensor using modulation of magnetization direction in GMR device.	IEEE International Magnetics Conference 2011, ET-03, Taipei, Taiwan, April 2011.	G. A. Wang S. Arai T. Kato S. Iwata

III. Domestic Conferences

Title	Conference	Authors
1. Development of a domain-wall displacing type GMR sensor.	第 34 回日本磁気学会学術講演会，5aF-6，つくば国際会議場，茨城，September 2010.	G. A. Wang S. Nakashima S. Arai T. Kato S. Iwata
2. 磁壁移動方式 TMR 磁気センサーにおけるフリー層の磁区構造。	平成 22 年度電気関係学会東海支部連合大会，A5-2，中部大，愛知，August 2010.	増田圭治 王国安 加藤剛志 岩田聡